



المملكة العربية السعودية
مدينة الملك عبدالعزيز للعلوم والتقنية
الادارة العامة لبرامج المنح البحثية

المشروع البحثي التطبيقي أت - 30 - 36

الاشتقاق العكسي لدوال استقبال الموجات الأولية
والقصيرة وتشتيت السرع : تقنية جديدة لتحديد التركيب
التفصيلي للغلاف الصخري في الدرع العربي

التقرير النهائي المنقح

أ. د. عبدالله بن محمد العمري (الباحث الرئيسي)

جامعة الملك سعود

محرم 1435 هـ - نوفمبر 2013 م



**Kingdom of Saudi Arabia
King Abdulaziz City for Science and Technology
General Directorate of Research Grants Programs**

AR - 30 - 36

**Joint Inversion of P- and S-Wave Receiver Functions
and Dispersion Velocities : A New Technique for
Determining Detailed Lithospheric Structure in the
Arabian Shield**

REVISED FINAL REPORT

Prof. Abdullah M. Al-Amri (P - I)

KING SAUD UNIVERSITY

Muharram 1435 H – November 2013 A.D



جميع حقوق الطبع محفوظة لمدينة الملك عبدالعزيز للعلوم والتقنية. غير مسموح بطبع أي جزء من أجزاء هذا التقرير أو خزنه في أي نظام لخزن المعلومات واسترجاعها أو نقله على أي هيئة أو بأي وسيلة سواء كانت إلكترونية أو مغnetic أو ميكانيكية، أو استنساخاً، أو تسجيلاً، أو غيرها إلا بإذن من صاحب الطبع. إن كافة الآراء والنتائج والاستنتاجات والتوصيات المذكورة في هذا التقرير هي خاصة بالباحثين ولا تعكس وجهة نظر المدينة.

All Rights Are Reserved to King Abdulaziz City for Science and Technology. No Part of this publication may be reproduced, stored in a retrieval system or transmitted in any form or by any means-electronic, electrostatic magnetic tape, mechanical, photocopying, recording or otherwise - without the permission of the copyright holders in writing. All views, results, conclusions, and recommendations in this report represent the opinions of the authors and do not reflect opinions of KACST.

ACKNOWLEDGMENTS

This is the final report of the research project **AR-30 - 36**. The author would like to express his thank and gratitude to King Abdulaziz City for Science and Technology for funding this project. This work would not have been possible without the generous assistance of **KACST**.

Drs. Jordi Julia and Eric Matzel, the project consultants, whose expert guidance and continuing advice made this work possible. Their willingness to devote their time greatly facilitated the completion of the project we owe them a deep debt of gratitude and a great deal of thanks. Grateful acknowledgment is also extended to the anonymous referees for their helpful suggestions and criticism of previous progress reports.

Finally and most importantly, we would like to extend our sincerest thanks to Eng. Mostafa Hemeda from **KACST** for processing earthquake data and to Dr. Dr. Michael Pasanos who helped in performing surface wave group velocity measurements and tomography.

الملخص العربي

تتميز المملكة العربية السعودية بأنها منطقة فقيرة زلزالية، نظراً لندرة البيانات الزلزالية المتوفرة. وبالرغم من الجزء الأكبر منها يعتبر غير نشط زلزالي، إلا أنها محاطة بمصادر زلزالية إقليمية في المناطق النشطة تكتونياً من إيران وتركياً إلى الشمال الشرقي، غور البحر الأحمر المجاور لل الدرع العربي بالجنوب الغربي، ونطاق الصدع التحولي بالبحر الميت في الشمال . تعتبر منطقة الدرع العربي والبحر الأحمر من الأماكن القليلة في العالم التي خضعت لشد قاري نشط وتكون قشرة بحرية حديثة .

دراسة الدرع العربي لها أهمية كبيرة للمجتمع الجيولوجي الدولي بسبب (أ) أنه يوفر مثالاً رائعاً عن القارة المتصدعة حديثاً، أحد الأفكار المحورية في الصفائح التكتونية، (ب) الصخور البركانية البازلتية الحديثة (أقل من 12 مليون سنة) في الدرع الشرقي مرتبطة بمرحلة ما بعد التصدع ، وهي أيضاً فكرة محورية في شرح التصدع القاري، (ت) هو واحد من أوضح الأمثلة لتكتونية الصفائح لعصر ما قبل الكمبري المتأخر ونمو القشرة الأرضية، وجميعها موضوعات جدل مكثف في المجالات العلمية.

من أجل الحد من المخاطر الزلزالية، وتحسين موقع الزلازل ومعايير القدر الزلزالي في المملكة العربية السعودية، فـ قد اقتربنا لتحديد تركيب الغلاف الصخري بالدرع العربي الحصول على نماذج سرعة موجات القص عند محطات رصد الزلازل ذات النطاق العريض في المملكة العربية السعودية من خلال تكنية تم تطويرها حديثاً للربط بين مجموعات متعددة من البيانات السيزمية.

قمنا بتطوير نماذج جديدة لسرعة لسماكة الغلاف الصخري وتركيب السرعة للدرع العربي من خلال الاشتقاء العكسي لمجموعات متعددة من البيانات: دوال المستقبل للموجات الأولية، دوال المستقبل لموجات القص ، سرعة تشتت الموجة السطحية، والمضاهاة المتقطعة بين سرعات تشتت الضوضاء السائدة. تتحدث هذه الورقة عن مهام ثلاثة التي تهدف إلى تطوير نماذج لسرعة القص بالغلاف الصخري مع العمق للدرع العربي .

قمنا أولاً بوصف تفصيلي عن العملية التي اتبعناها للحصول على دالة المستقبل للموجات الأولية و دالة المستقبل لموجات القص لمحطات النطاق العريض الدائمة (هيئة المساحة الجيولوجية السعودية، مـ دـيـنـةـ الـمـلـكـ عـبـدـالـعـزـيزـ لـلـعـلـومـ وـالـتـقـنـيـةـ) والشبكات السيزمية المؤقتة في المملكة العربية السعودية، ثانياً قمنا بتحليل

دوال المستقبل للموجات الأولية للحصول على تقديرات لسمك القشرة وال نسبة بين سرعة الموجات الأولية وسرعة موجات القص للقشرة العربية، وأخيراً ترحيل دوال المستقبل لموجات القص إلى مجال العمق لتقدير سماكة الغلاف الصخري.

أظهرت تحليلات دوال المستقبل للموجات الأولية أن قيم سمك القشرة الأرضية تتراوح من 45-25 كم ، مع قشرة رقيقة بجانب البحر الأحمر وخليج العقبة وقشرة أكثر سماكاً تحت الر صيف العربي ، وأن النسبة بين سرعة الموجات الأولية وسرعة موجات القص تتراوح بين 1.7 - 1.8 ، موضحاً مدى التكوينات (فلزية - مافية) لقشرة الدرع . اقترحت ترحيلات دوال المستقبل لموجات القص أن سمك القشرة الأرضية يقع في نطاق 80 - 100 كم لأجزاء من الدرع ملائمة للبحر الأحمر وخليج العقبة وأيضاً بالقرب من الخليج العربي.

وأيضاً قمنا بوصف تفصيلي للاشتقاء العكسي لدوال المستقبل للموجات الأولية ، وموجات القص وسرعات التشتت للموجة السطحية المستخدمة لتطوير نماذج السرعة القصية بالغلاف الصخري مع العمق بالدرع العربي، وبعد ذلك قدمنا نماذج الاشتقاء العكسي للمحطات منهج الاشتقاء العكسي ربط بنجاح بين جميع مجموعات البيانات (دوال المستقبل للموجات الأولية، دوال المستقبل لموجات القص،

سرعات التشتت) وقدم نماذج لتغيير السرعة القصية مع العمق وصولاً إلى 250 كم عمق في الدرع (قدر الإمكان) للرصيف العربي . الجزء القشرى من النماذج يتفق تماماً مع التقديرات الأولية لسمك القشرة الأرضية المذكور أولاً ومع التقديرات المستقلة في الدراسات السابقة، وجاء الغلاف الصخري يتفق أيضاً مع تقديرات سmek الغلاف الصخري، وربما نجح بإثارة كثير من الاهتمام، في تصوير قناة الغلاف الوهن المائي ذات السرعة المنخفضة تحت أجزاء من الدرع والرصيف العربي.

في هذه الدراسة، استخدمنا أيضاً طريقة الضوضاء السائدة لتصوير سرعة القص في القشرة والوشاح العلوي تحت شبه الجزيرة العربية . وحسبنا دوال مصاهاة جرين لجميع أزواج المحطة المتاحة داخل الشبكاتزلزالية السعودية، والتي توفر مئات من المسارات الفريدة من نوعها في المنطقة . قمنا بقياس السرعات الجماعية بالتزامن مع الاشتقاء العكسي لدوال الاستقبال وسرعات التشتت .

بشكل منفصل، تم اقتباس الشكل الموجي لدالة جرين للحصول على أفضل نماذج أحادية البعد على طول كل مسار، وتخليق نموذج ثلاثي الأبعاد بناءاً على تلك النتائج. الدقة العالية أمكن تحديدها من خلال كثافة المحطات ، وكانت الأفضل على طول الجزء الغربي من المملكة على ساحل البحر الأحمر.

سرعات التشتت من الموجات السطحية والمضاهاة المتقاطعة للضوضاء السائدة تحفظت على متوسط السرعة في القشرة الضحلة والعميقة والوشاح الصخري، على التوالي، ولكنهم غير قادرين على اكتشاف الثغرات السيزمية . الاشتباك العكسي لدوال المستقبل وسرعات التشتت اجتاز الفجوات بين قواعد البيانات وأنتج نماذج سرعة لباطن الأرض التي تدمج القدرة عالية الدقة من دوال المستقبل مع الطابع الفريد لسرعات التشتت.

بصفة عامة، فإن هذه التحليلات وفرت تقديرات للتراكيب الفيزيائية للقشرة والوشاح العلوي تحت شبه الجزيرة العربية . سوف تقدم نتائج هذه الدراسة معلومات جديدة عن عمليات التي تحدث خلال مرحلة الانفصال القاري . وعلى وجه الخصوص، تم الحصول على نماذج أفضل للجزء العلوي من الوشاح العلوي لتحديد عمق مصدر النشاط البركاني وعن عمليات رفع الدرع العربي.

SUMMARY

Saudi Arabia is an area which is characterized very poorly seismically and for which little existing data is available. While for the most part aseismic, the area is ringed with regional seismic sources in the tectonically active areas of Iran and Turkey to the northeast, the Red Sea Rift bordering the Shield to the southwest, and the Dead Sea Transform fault zone to the north. The Arabian Shield and Red Sea region is considered one of only a few places in the world undergoing active continental rifting and formation of new oceanic lithosphere.

Studying the Arabian Shield is of great interest to the international geologic community as (i) it provides a superb example of a recently rifted continent, one of the cornerstone ideas of plate tectonics, (ii) young basaltic volcanic rocks (< 12 Ma) in the eastern shield are related to post-rifting plume activity, also a cornerstone idea in explaining continental rifting, and (iii) it is one of the clearest examples of late Precambrian plate tectonics and crustal growth, all intensively debated topics in high-profile international journals such as Science or Nature.

In order to reduce seismic hazard, improve earthquake locations and magnitude calibration in Saudi Arabia, we propose to determine the detailed lithospheric structure of the Arabian Shield by obtaining S-wave velocity models at broadband seismic stations in Saudi Arabia through a newly developed technique that jointly inverts multiple seismic data sets.

We developed new velocity models of lithospheric thickness and velocity structure for the Arabian Shield by jointly inverting multiple data sets : P-wave receiver functions, S-wave receiver functions, surface-wave dispersion velocities, and

ambient-noise cross-correlation dispersion velocities. This document reports on three tasks that aim at developing models of lithospheric S-velocity with depth for the Arabian shield.

We (i) describe in detail the process that we followed to obtain P-wave receiver function (PRF) and S-wave receiver function (SRF) estimates for broadband stations belonging to permanent (Saudi Geological Survey, King Abdulhaziz Center for Science and Technology) and temporary (IRIS-PASSCAL) seismic networks in Saudi Arabia, (ii) analyze the PRFs to obtain estimates of thickness and bulk Vp/Vs ratio for the Arabian crust, and (iii) migrate the SRFs into the depth domain to estimate lithospheric thickness.

The analysis of the PRFs reveals values of 25 - 45 km for crustal thickness, with the thin crust next to the Red Sea and Gulf of Aqaba and the thicker crust under the platform, and Vp/Vs ratios in the 1.70 – 1.80 range, suggesting a range of compositions (felsic to mafic) for the shield's crust. The migrated SRFs suggest lithospheric thicknesses in the 80-100 km range for portions of the shield close to the Red Sea and Gulf of Aqaba and also near the Arabian Gulf.

We also (i) describe in detail the joint inversion of P- and S-wave receiver functions and surface-wave dispersion velocities utilized to develop the models of lithospheric S-velocity with depth for the Arabian shield and (ii) present joint inversion models for the Saudi stations. The joint inversion approach successfully matches all inverted data sets (PRFs, SRFs, and dispersion velocities) and provides models of S-velocity variation with depth down to 250 km depth for the shield and (when possible) platform. The crustal portion of the models agrees well with preliminary estimates of crustal thickness reported in Task 1 and with independent estimates found in the

literature; the lithospheric portion agrees with lithospheric thickness estimates from Task 1 and, perhaps more interestingly, succeeds in imaging the asthenospheric low-velocity channel under portions of the shield and platform.

In this study, we used the ambient noise method to image the shear velocity in the crust and uppermost mantle beneath the Arabian Peninsula. We calculated the ambient noise correlation Green's functions for all available station pairs within the Saudi seismic networks, which provide hundreds of unique paths exclusively sampling the region. We measured group velocities in conjunction with the joint-inversion of receiver functions and dispersion velocities. Separately, we inverted the Green's function waveforms for the best 1D models along each path and created a 3D model based on those results. Greatest resolution is determined by station density and is greatest along the western part of the kingdom along the Red Sea.

Dispersion velocities from ballistic surface-waves and ambient-noise cross-correlations constrain the average velocity structure in the shallow and deep crust and lithospheric mantle, respectively, but are unable of detecting seismic discontinuities. The joint inversion of receiver functions and dispersion velocities bridges resolution gaps among the datasets and produces velocity models of the subsurface that integrate the high-resolution power of the receiver functions with the uniqueness of the dispersion velocities.

Generally speaking, these analyses will provide estimates of the physical structure of the crust and upper mantle beneath the Arabian Peninsula. The results of this study will provide valuable new constraints on the processes at work during continental break-up. In particular we will have better models of upper mantle structure to determine the depth of the source of volcanism and uplift of the Arabian Shield.

TABLE OF CONTENTS

CHAPTER No.	TITLE	Page No.	
	ACKNOWLEDGMENTS	4	
	ABSTRACT (Arabic)	5	
	ABSTRACT (English)	10	
1	INTRODUCTION	16	
	1.1 Objectives & Tasks	18	
	1.2 Literature Review	20	
2	SEISMOTECTONIC SETTING	25	
3	METHODOLOGY	32	
	3.1 Receiver Function	32	
	3.2 Ambient-Noise-Cross-Correlation	35	
	3.3 Surface-Wave Dispersion	37	
	3.4 Joint Inversion	41	
4	RESULTS & DISCUSSION	47	
	4.1 Computation of P-wave Receiver Functions	47	
	4.2 Crustal Thickness and Bulk V_p / V_s Ratios	52	
	4.3 Computation of S-wave Receiver Functions	58	
	4.4 Lithospheric Thickness	60	
	4.5 Incorporating High-Frequency Dispersion from Ambient Noise Cross-Correlations	64	
	4.6 Group Velocity Measurements and S/N	66	
	4.7 1 D Model Inversions	67	
	4.8 Localized 3 D Tomography	68	
	4.9 Developing Joint Inversion Models for the Arabian Shield	75	
		CONCLUSIONS & RECOMMENDATIONS	82
		REFERENCES	85
	RESPONSES TO REVIEWERS' COMMENTS	92	
	APPENDIX A	99	

LIST OF FIGURES

Figure No.	Description	Page No.
1.1	Inversion of synthetic "data"	22
2.1	Seismotectonic map of the Arabian Peninsula and Arabian plate boundaries showing earthquake locations and volcanic centers.	30
2.2	Location map of the Arabian Plate showing major tectonic elements of the Arabian Shield and Platform	31
3.1	Seismic rays associated to a plane P-wavefront impinging at the base of a uniform velocity layer over a half-space	32
3.2	Seismic rays associated to a plane S-wave front impinging at the base of a layered velocity model	34
3.3	The Green's function emerges from the noise as more data are added to the correlation	36
3.4	Surface Wave Dispersion: path map including regional stations (red) and earthquakes (yellow) used for a tomographic inversion of the Rayleigh wave dispersion data	39
3.5	Surface Wave Attenuation: Path map (left) and initial result (right) for a surface wave inversion of the 25 second period Rayleigh wave	40
3.6	Joint inversion of noise-free, synthetic PRF, SRF, and group velocity "observations".	45
4.1	Topographic map of the Arabian Peninsula showing the broadband stations	49
4.2	Sample radial and transverse receiver function waveforms (PRFs) for three stations in the Arabian Peninsula	51
4.3	Map displaying variation in point measurements of crustal thickness (H) and V_p/V_s ratios in the Saudi Arabia	57
4.4	Overlay of S-wave receiver functions obtained at each broadband station considered in this study	62
4.5	Migrated SRF stacks for several stations in Saudi Arabia	63

Figure No.	Description	Page No.
4.6	A station map showing the broadband seismic stations across the Peninsula used in the ambient noise correlation	69
4.7	A profile of ambient noise correlation Green's functions computed using continuous data from the month of January 2010.	70
4.8	SNR for the correlation Green's functions is a strong function of both distance and frequency	71
4.9	Envelopes of the noise correlation Green's functions (blue) compared with synthetics for the best fitting 1D models for each path (red).	72
4.10	The best fitting 1D models for a subset of the paths	73
4.11	Slices through a localized 3D model at 10, 20, 50 and 100 km.	74
4.12	Joint inversion of PRFs, SRFs, and SW dispersion velocities at station AYUS	78
4.13	Summary of joint inversion results for broadband stations in Saudi Arabia.	81

LIST OF TABLES

Table No.	Description	Page No.
1	Stations and waveform statistics for the selected dataset	50
2	Point measurements of crustal thickness (H) and V_p/V_s ratio from hk-stacking	54

1. INTRODUCTION

The Arabian Shield comprises the western one-third of the Arabian Peninsula and is mostly composed of Precambrian metamorphic and plutonic rocks. It is perhaps the clearest example of late Precambrian plate tectonics and crustal growth and a superb example of a recently rifted continent, one of the cornerstone ideas of plate tectonics. Moreover, although the shield is composed of Precambrian terrains, it contains Tertiary and Quaternary volcanic rocks - the *harrats* - which are related to the early stages of the Red Sea formation and possibly to plume-related lithospheric "erosion". Mapping the subsurface structure of the Shield is therefore an important step towards improving our understanding of the continental growth processes and subsequent modifications through rifting and plume-lithosphere interaction.

Seismic imaging of the lithosphere under the Arabian shield and platform is critical to help answer important geologic questions of regional and global interest. The Arabian Shield can be regarded as an amalgamation of several arcs and microplates of Proterozoic age that culminated in the accretion of the Arabian portion of Gondwana during the Pan-African event at ~550 Ma (Stoeser and Camp, 1985; Gettings et al., 1986). The role of important geologic features observed on the surface, such as the lineaments and shear zones separating the Proterozoic terrains in the shield, are not completely understood and might be linked to deeper structures. For instance, interpretation of aeromagnetic maps of the north-south trending Najd Fault system indicates that the Najd belt is broader at depth than the outcropping fault complex and that continuous structures underlie arrays of faults at surface, and the thrusting of the Al-Amar fault, one of the most important

geological-tectonic feature of the eastern shield, with the eastern Ar-Rayn terrane has long been debated.

Also, current models of Precambrian crustal evolution (Durrheim and Mooney, 1991) predict that Proterozoic terranes are underlain by fertile (FeO-rich) cratonic roots that will allow the production of mafic magmas and the under plating of the Proterozoic crust upon heating by a thermal event. The shield contains Tertiary and Quaternary volcanic rocks related to the early stages of the Red Sea formation and possibly plume-related lithospheric “erosion” (Stoeser and Camp, 1985; Camp and Robool, 1992). Interestingly, seismic velocity models of the crust and uppermost mantle of the shield (e.g. Julià et al., 2003) revealed crustal thicknesses under 40 km and lower crustal velocities below 4.0 km/s, suggesting the absence of a layer of mafic under plate under the Arabian terrains.

Nonetheless, the surface volcanism attests towards recent (< 30 Ma) generation of magmas in the continental lithosphere. Therefore, imaging of the continental lithosphere under the Arabian Shield might provide a unique opportunity for imaging the initial stages of mafic crustal under plating postulated by Durrheim and Mooney (1991).

Also, while for the most part aseismic, the Arabian shield is ringed with regional seismic sources in the tectonically active areas of Iran and Turkey to the northeast, the Red Sea Rift bordering the Shield to the southwest, and the Dead Sea Transform fault zone to the north. The Arabian shield is an area that is characterized very poorly seismically and for which little data is available. Mapping subsurface structure is therefore also important to improve earthquake locations and magnitude calibration, and help mitigate seismic hazard in Saudi Arabia.

1.1 OBJECTIVES & TASKS

In this project, we developed new velocity models of lithospheric thickness and velocity structure for the Arabian Shield by jointly inverting multiple data sets : P-wave receiver functions, S-wave receiver functions, surface-wave dispersion velocities, and ambient-noise cross-correlation dispersion velocities. The velocity models will provide robustly constrained images of the velocity structure of the Arabian lithosphere and accurately determine the depth of seismic discontinuities bounding the top and bottom of LVZs associated with the migration of magma within the crust and lithospheric mantle. The velocity models that will be produced through the joint inversion of multiple datasets will be better constrained and have better resolution than other published models for the region. This is because we will be fitting four complimentary seismic datasets in our inversions. The joint inversion will take advantage of P-wave receiver functions to constrain depths to intra-crustal discontinuities and crustal thickness, S-wave receiver functions to constrain depths to lithospheric discontinuities and lithospheric thickness, and the dispersion velocities from ambient noise cross-correlation and surface-waves to constrain velocities and velocity gradients in the shallow crust and continental lithosphere, respectively.

The resolution of the velocity-depth profiles obtained by the joint inversion of receiver functions and dispersion velocities is a combination of the resolving power of the data sets. Our experience suggests that S-wave velocities and layer thicknesses are generally constrained within 0.1 km/s and 2.5 km in the crust and uppermost mantle, and that the resolution degrades with depth (Julià et al., 2008;

Julià et al., 2009). Laterally, the resolution is at best within the size of one surface-wave tomographic cell (typically $1^\circ \times 1^\circ$).

Together these analyses will result in a unified model of the structure and physical state of the lithosphere beneath the Arabian Shield and Red Sea. Finally, this proposal will suggest several tasks to implement all results as follows :

Task 1 – Computing PRFs and SRFs for all the broadband stations within the Saudi seismic networks. We followed the approaches of Langston (1979) and Sodoudi (2005) for the computation of PRFs and SRFs, respectively, along with the iterative deconvolution method of Ligorría and Ammon (1999). The number of receiver function waveforms depend on the recording time window and quality of the broadband station.

Task 2 – Computing ambient noise correlation Green's functions for all available station pairs within the Saudi seismic networks. Together they provided hundreds of additional, unique paths exclusively sampling the region of interest. Following the data processing procedure laid out by Bensen et al. (2007) for correlation and the methodology of Lin et al. (2008) for measurement, we measured both phase and group velocities for all the resulting empirical Green's functions and to be used in the joint inversion.

Task 3 – We jointly inverted the PRFs and SRFs obtained in task 1 with dispersion velocities measured on the Green's functions obtained in task 2 and with fundamental-mode, Rayleigh-wave, group and phase velocities borrowed from the tomographic studies of Pasmanos (2005) and Ekström et al. (1997) to precisely determine 1D crustal velocity structure and upper mantle.

1.2 Literature Review

P-wave receiver functions (PRFs) have become a popular method to examine crustal and upper mantle structure in a variety of tectonic settings around the globe (e.g. Langston, 1977; Owens et al., 1984; Ammon, 1991; Kosarev et al., 1999; Yuan et al., 2000). Teleseismic P-waveforms recorded at three-component seismic stations contain much information on the earthquake source, the structure near both the source and the receiver, and the mantle path in between. PRFs are obtained by removing the effects of the source and the path to isolate near-receiver structure (Langston, 1979). At relatively sharp velocity discontinuities, several percent of an incoming P-wave's energy is converted to a S-wave; the amplitudes of the resulting P-to-S conversions carry important information on the velocity contrast across the discontinuity and the S-P travel-times of the conversions depend on the depth of the discontinuity as well as the velocity of the structure above it. Examining both the radial and tangential receiver functions can provide additional constraints on dipping interfaces and anisotropy (e.g. Langston, 1977; Cassidy, 1992; Levin and Park, 1997).

The joint inversion of P-wave receiver functions (PRFs) and surface-wave dispersion velocities has proven an effective tool for determining the 1D velocity structure of the continental crust and its underlying uppermost mantle (e.g. Julià et al., 2003; 2005; 2008; 2009; Dugda et al., 2007; Keranen et al., 2009; Kgaswane et al., 2009). Both PRFs and surface-wave dispersion are mostly sensitive to S-wave velocity, but the constraints conveyed by each data set are different. PRFs are mostly sensitive to subsurface seismic discontinuities, constraining S-P travel-times between the discontinuities and the free surface and the S-wave velocity contrasts across them.

These constraints are relative in character, so PRFs alone cannot uniquely resolve velocity structure and independent *a priori* information is generally needed in order to choose among many competing models (Ammon et al., 1990). Surface-wave dispersion velocities, on the other hand, constrain absolute velocity with depth within frequency-dependent averages (e.g. Takeuchi and Saito, 1972), but the longer wavelengths at which surface-waves sample the subsurface prevents rapid variations in seismic velocity from being accurately resolved. Fortunately, the combination of these data sets into a joint inversion scheme bridges the resolution gaps among the datasets and yields velocity models that display little non-uniqueness while integrating the complementary constraints in each of them (Julià et al., 2000).

Although the joint inversion of PRFs and surface-wave dispersion velocities is successful in resolving fine velocity variations with depth within the crust and uppermost mantle, the resolution of similarly fine velocity variations at lithospheric and sub-lithospheric depths is generally difficult. Figure 1.1 displays an inversion of synthetic PRFs and fundamental-mode group velocities computed for a simple velocity model consisting of a 2-layer crust, an upper mantle lid, and a sub-lithospheric low-velocity zone, with the joint inversion scheme of Julià et al. (2000; 2003). The inverted model successfully recovers the sharpness of the intra-crustal discontinuity and the crust-mantle boundary, as expected from the perfect match between “observations” and predictions, but it fails to recover the sharpness of the deeper lithosphere-asthenosphere boundary (LAB). This degradation of the resolving power at the deeper levels is mostly due to the suppression of P-to-S reverberations between the free-surface and the deep discontinuities in the PRF waveforms.

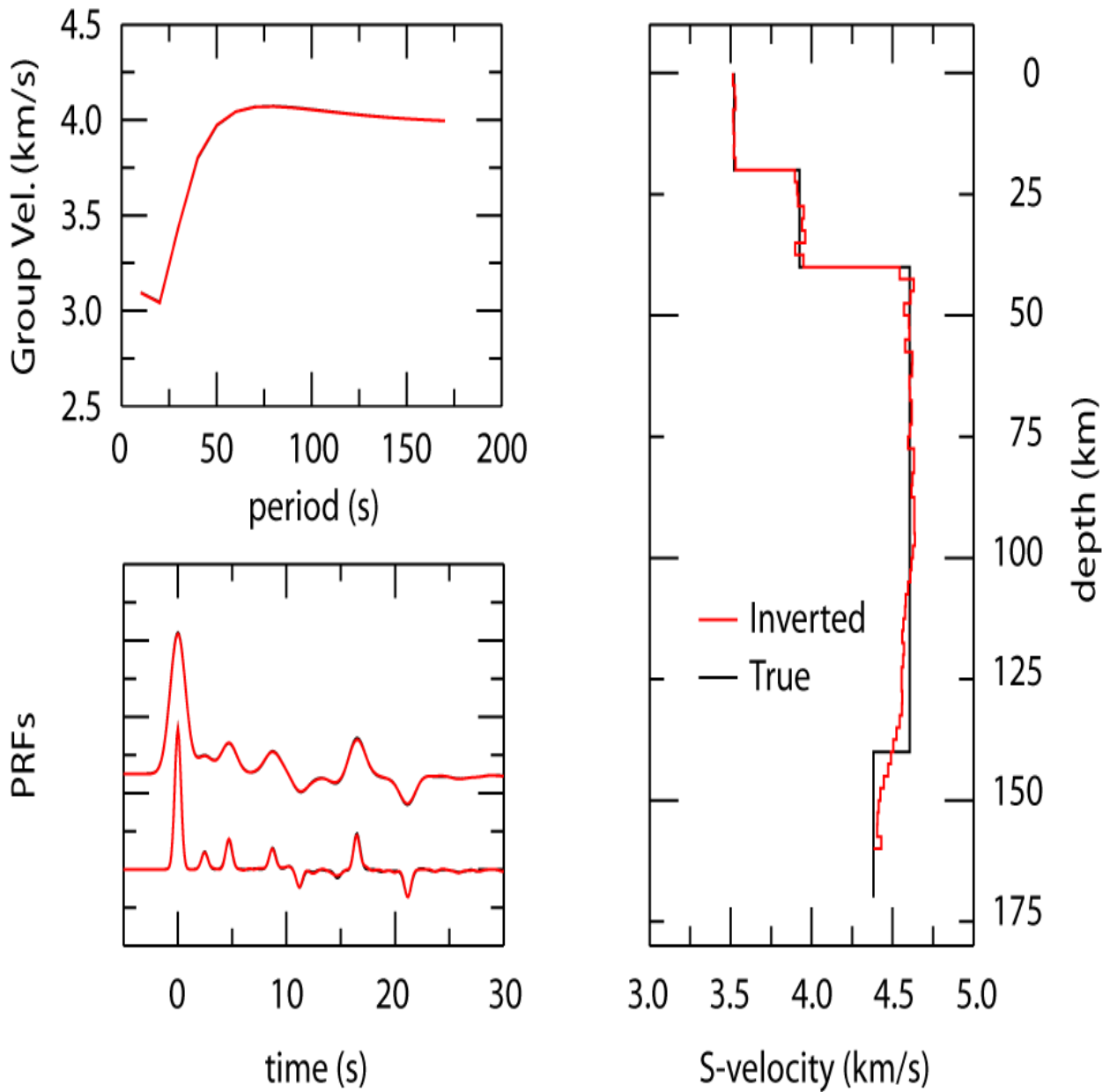


Figure 1.1 – Inversion of synthetic “data” generated from the “true” model in the right panel. The panels on the left display “observations” (black lines) and predictions (red lines) from the inverted model shown to the right. The match between observations and predictions is perfect, as expected from inversion of noise-free synthetic “data”. However, the inverted model is incapable of recovering the lithosphere - asthenosphere boundary at 140 km depth.

In the past few years, S-wave receiver functions (SRFs) have become an increasingly popular tool for investigating the structure of the lithospheric mantle, especially the depth of the LAB (e.g. Kumar et al., 2007; Wittlinger and Farra, 2007; Geissler et al., 2010). Although some authors have reported the signature of the LAB in PRF waveforms (Rychert et al., 2005; 2007, Rychert and Shearer, 2009), SRFs are generally preferred because, theoretically, the signature of the LAB in PRFs is likely to be masked under seismic energy reverberating between the Moho and the free-surface (Kumar et al., 2005). Moreover, for similar frequency contents, SRFs sample the lithospheric and sub-lithospheric mantle with shorter wavelengths than PRFs and have therefore better potential for constraining fine velocity variations at those depths. Combining the seismic constraints provided by PRFs, SRFs, and surface-wave dispersion velocities should then lead to improved estimates of lithospheric structure.

The correlation of ambient seismic noise is a new and rapidly developing field of seismology. One of the techniques included in the field of seismic interferometry, it is based on the observation that the Earth's background noise (generated in part by ocean waves, distant earthquakes and multiply scattered coda) includes coherent energy, which can be recovered by observing over long time periods and allowing the incoherent energy to cancel out (Hennino et a., 2001; Weaver and Lobkis, 2001). The cross correlation of ambient noise between a pair of stations results in a waveform that is identical to the seismogram that would result if an impulsive source located at one of the stations was recorded at the other (Campillo and Paul, 2003; Malcolm et al., 2004; Snieder and Safak, 2006; Wapenaar 2004). This means that

many of the techniques developed in earthquake seismology can be applied directly to the correlations.

A major advantage of the noise-correlation technique is that it strips away dependence on earthquakes or artificial sources for a solution. Problems of source location and velocity heterogeneities outside the region of interest are no longer present, as only the structure between the station pair contributes to the signal. In particular, it allows high resolution imagery beneath dense seismic networks even in areas of low seismicity. The energy in the correlated waveforms is also quite high in frequency bands which are particularly sensitive to the Earth's crust. Ambient noise correlation does require long, preferably continuous data records as the Green's function emerges from the incoherent noise. At local and regional distances, the Green's function is typically lost in the incoherent noise if correlations are shorter than a week. Robust estimates of the Green's function typically require months of data or more.

To date, most ambient seismic noise research has focused on group velocity measurements of the resulting surface waves (Moschetti et al., 2007; Shapiro et al, 2005) although more recently, work has begun on measuring the phase velocities (Lin et al, 2008) and amplitudes (Prieto and Beroza 2008 ; Snieder and Safak, 2006; Matzel, 2008) and the new discoveries and methodologies are constantly being developed.

2. SEISMOTECTONIC SETTING

The Arabian Peninsula forms a single tectonic plate, the Arabian Plate. It is surrounded on all sides by active plate boundaries as evidenced by earthquake locations. Figure 2.1 shows a map of the Arabian Peninsula along with major tectonic features and earthquake locations. Active tectonics of the region is dominated by the collision of the Arabian Plate with the Eurasian Plate along the Zagros and Bitlis Thrust systems, rifting and seafloor spreading in the Red Sea and Gulf of Aden. Strike-slip faulting occurs along the Gulf of Aqabah and Dead Sea Transform fault systems. The great number of earthquakes in the Gulf of Aqabah pose a significant seismic hazard to Saudi Arabia. Large earthquakes in the Zagros Mountains of southern Iran may lead to long-period ground motion in eastern Saudi Arabia.

The accretionary evolution of the Arabian plate is thought to have originated and formed by amalgamation of five Precambrian terranes. These are the Asir; Hijaz, and Midyan terranes from the western part of the Arabian shield, and from the eastern side of the shield are the Afif terrane and the Amar arc of the Ar Rayn micro-plate. The western fusion is along the Bir Umq and Yanbu sutures (Loosveld et al 1996). The eastern accretion may have started by about 680-640 million years ago (Ma) when the Afif terrane collided with the western shield along the Nabitah suture. At about 670 Ma, a subduction complex formed west of Amar arc. Along this subduction zone, the Afif terrane and Ar Rayn microplate collided that lasted from about 640-620 Ma. (Al-Husseini 2000). The north trending Rayn anticlines and conjugate northwest and northeast fractures and faults may have formed at this

time (Figure 2.2).

The Arabian Shield is an ancient land mass with a trapezoidal shape and area of about 770,000 sq. km. Its slightly-arched surface is a peneplain sloping very gently toward the north, northeast, and east. The framework of the shield is composed of Precambrian rocks and metamorphosed sedimentary and intruded by granites. The fold-fault pattern of the shield, together with some stratigraphic relationships suggests that the shield have undergone two orogenic cycles.

To the first order, the Arabian shield is composed of two layers, each about 20km thick, with average velocities of about 6.3 km/s and 7 km/s respectively (Mooney et al 1985). The crust thins rapidly to less than 20 km total thickness at the western shield margin, beyond which the sediments of the Red Sea shelf and coastal plain are underlain by oceanic crust.

The platform consists of the Paleozoic and Mesozoic sedimentary rocks that unconformably overlays the shield and dip very gently and uniformly to the E-NE towards the Arabian Gulf (Powers et al., 1966). The accumulated sediments in the Arabian platform represent the southeastern part of the vast Middle east basin that extend eastward into Iran, westward into the eastern Mediterranean and northward into Jordan, Iraq and Syria.

The Arabian shield isolated the Arabian platform from the north African Tethys and played an active paleogeographic role through gentle subsidence of its northern and eastern sectors during the Phanerozoic, allowing almost 5000 m of continental and marine sediments deposited over the platform. This accumulation of sediments represents several cycles from the Cambrian onward, now forms a homocline dipping very gently away from the Arabian shield.

Several structural provinces can be identified within the Arabian platform : 1) An interior homocline in the form of a belt, about 400 km wide, in which the sedimentary rocks dip very gently away from the shield outcrops. 2) An interior platform, up to 400 km wide, within which the sedimentary rocks continue to dip regionally away from the shield at low angles. 3) Intra-shelf depressions, found mainly around the interior homocline and interior platform.

The Saudi Arabian Broadband Deployment (Vernon and Berger, 1997; Al-Amri , 1999) provided the first broadband recordings for the Arabian Shield and Platform. This deployment consisted of 9 broadband, three-component seismic stations along a similar transect to a seismic refraction study (Mooney et al., 1985; Gettings et al., 1986). Data from this deployment resulted in several reports of crustal and upper mantle structure (Sandvol et al., 1998; Mellors et al., 1999; Rodgers et al., 1999; Benoit et al., 2003). The crustal model of the western Arabian Platform shows a slightly higher P-velocity for the upper crust in the Arabian Shield than in the Platform. Also the crust of the Platform appears to be 3-5 km thicker than in the Shield. The Moho Discontinuity beneath the western Arabian Platform occurs at a depth of 40-45 km, and the velocity of the upper mantle is about 8.2 km/sec (Al-Amri 1998; 1999; Rodgers et al., 1999; Tkalcic et al., 2006).

Generally, the crustal thickness in the Arabian Shield varies from about 15 km in the Red Sea, to 20 km along the Red Sea coast to about 35-40 km in the central Arabian Shield (Sandvol et al., 1998; Al-Damegh et al., 2005; Tkalcic et al., 2006). Reports of large-scale seismic tomography (e.g. Debayle et al., 2001) suggest that a low-velocity anomaly in the upper mantle extends laterally beneath the Arabian Shield from the Red Sea in the west to the Shield-Platform boundary in the east.

Additionally, Debayle et al. (2001) observed a narrow region of low-velocity beneath the Red Sea and the western edge of the Arabian Shield, extending to 650 km depth. Recent tomographic imaging using SANDSN data found low velocities extending to 400 km in the upper mantle beneath the southern Red Sea and Arabian Shield, but more normal velocities beneath the northern Red Sea, suggesting different geodynamic connections between rifting of the Red Sea and mantle upwelling in the southern and northern Red Sea.

High-frequency regional S-wave phases are quite different for paths sampling the Arabian Shield than those sampling the Arabian Platform (Mellors et al., 1999; Al-Damegh et al., 2005). In particular the mantle Sn phase is nearly absent for paths crossing parts of the Arabian Shield, while the crustal Lg phase has abnormally large amplitude. This may result from an elastic propagation effect or extremely high mantle attenuation and low crustal attenuation occurring simultaneously, or a combination of both. High-frequency Lg does not propagate as efficiently across the Arabian Platform compared to the Shield but Sn does propagate efficiently. This suggests that crustal attenuation is low in the higher velocity crust of the Arabian Shield, or sedimentary structure in the Arabian Platform attenuates and disrupts the crustal waveguide for Lg. These observations imply high-frequency ground motions will propagate with lower attenuation in the Arabian Shield compared to the Arabian Platform.

It is known that high-frequency regional phase behavior in the Arabian Plate is quite variable as demonstrated by Al-Damegh et al. (2005). They investigated the attenuation of Pn phase (Q_{Pn}) for 1–2 Hz along the Red Sea, the Dead Sea fault system, within the Arabian Shield and in the Arabian Platform. Consistent with the

Sn attenuation, they observed low Q_{Pn} values of 22 and 15 along the western coast of the Arabian Plate and along the Dead Sea fault system, respectively, for a frequency of 1.5 Hz. Higher Q_{Pn} values of the order of 400 were observed within the Arabian Shield and Platform for the same frequency. Their results based on *Sn* and *Pn* observations along the western and northern portions of the Arabian Plate imply the presence of a major anomalously hot and thinned lithosphere in these regions that may be caused by the extensive upper mantle anomaly that appears to span most of East Africa and western Arabia.

More recently, Pasquenos et al. (2009b) applied a technique to simultaneously invert amplitudes measurements of Pn, Pg, Sn and Lg to produce P-wave and S-wave attenuation models of the crust and upper mantle. The attenuation is modeled as P-wave and S-wave attenuation surfaces for the crust, and similar set for the upper mantle. They used all of the phase amplitudes together by using the appropriate (source, geometrical-spreading, site, and attenuation) terms for each phase. Because this is a model-based inversion, the velocity structure of the region can be included to more accurately model the predicted ray paths (Fig. 2.2).

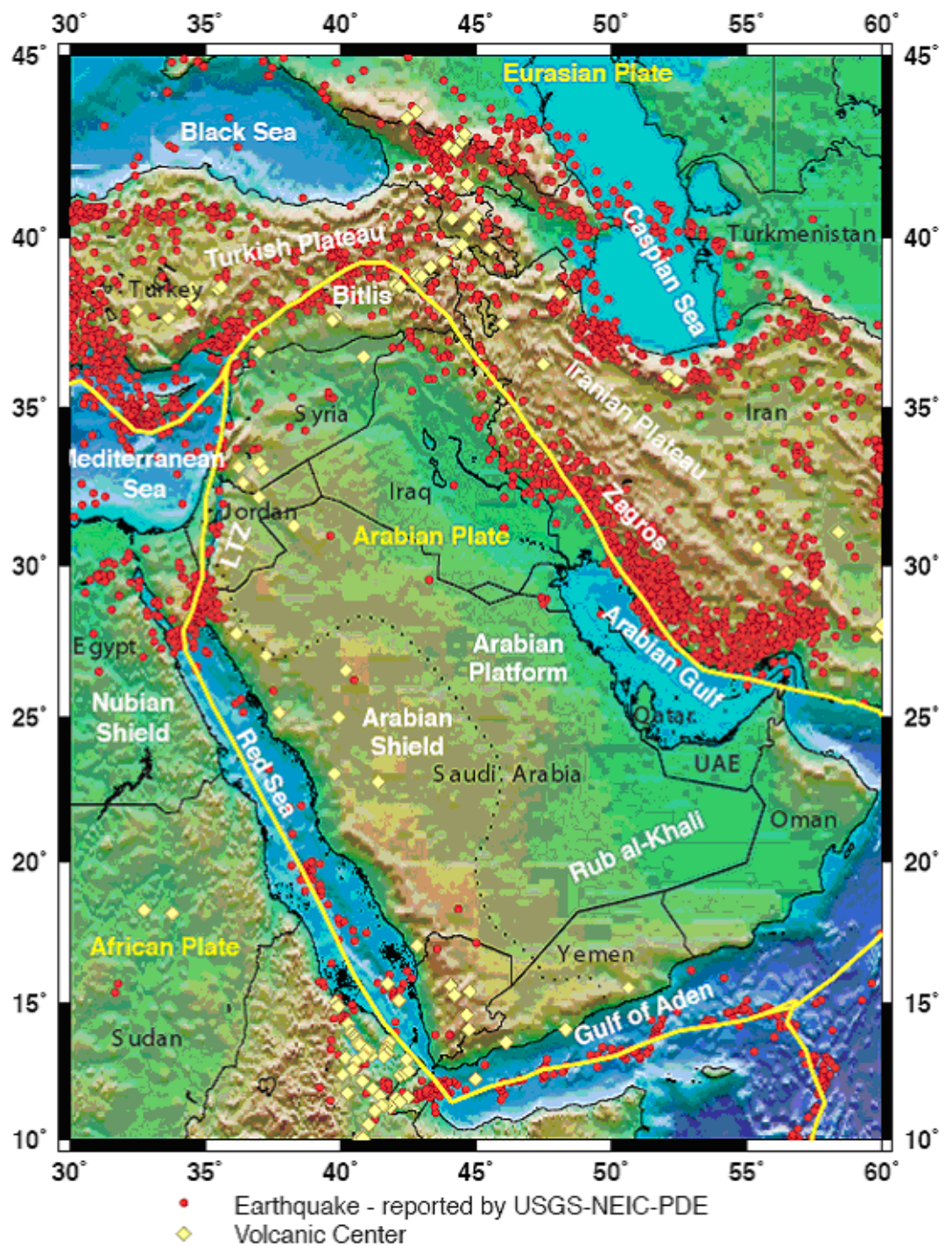
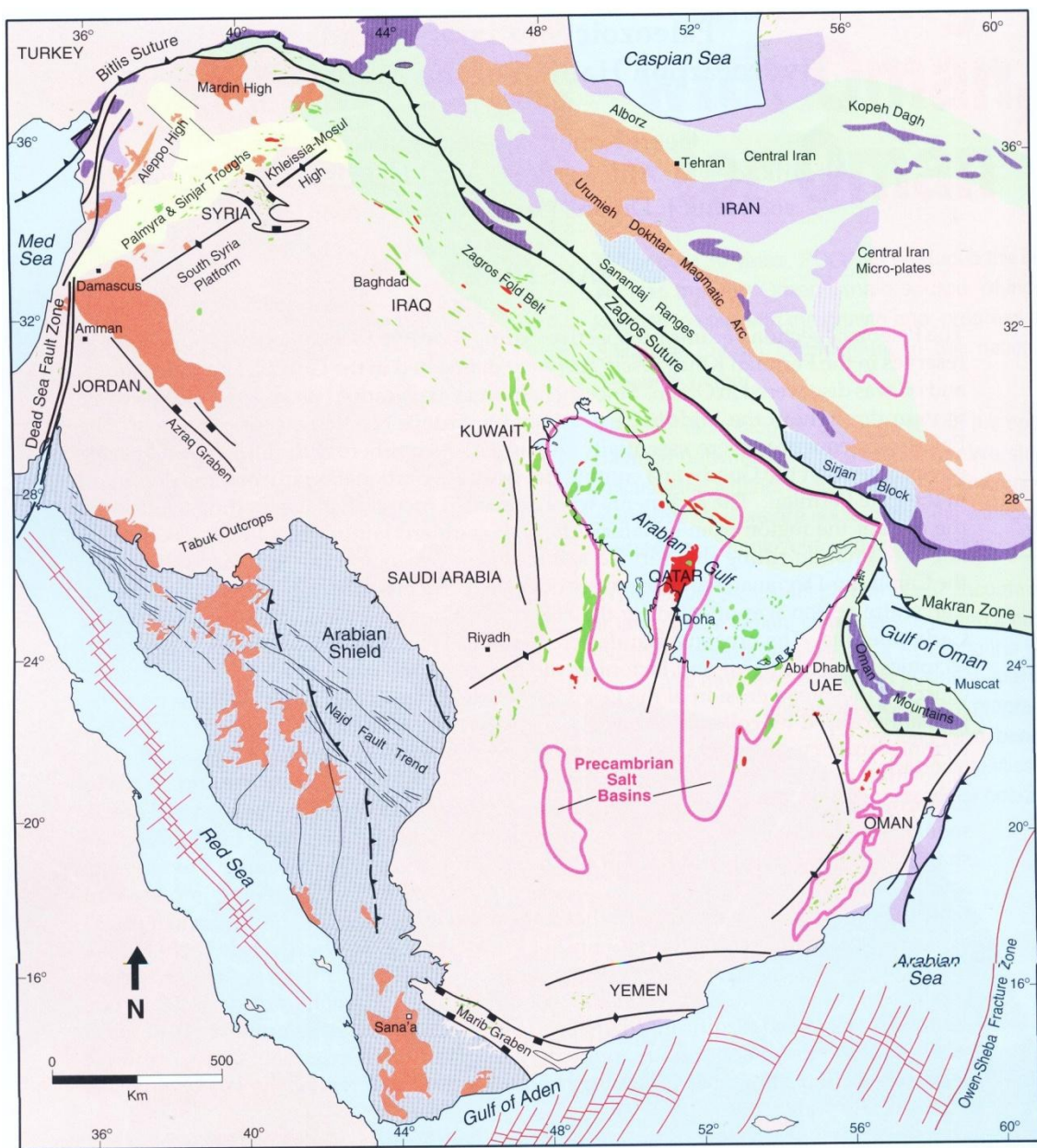


Figure 2.1 Seismotectonic map of the Arabian Peninsula and Arabian plate boundaries showing earthquake locations and volcanic centers.



LEGEND

Fold/thrust belts	Ophiolites
Intraplate inversion zone	Calcarenite alkaline volcanics
Tertiary basins	Alkaline basalts
Hercynian mobile zone	Crystalline basement

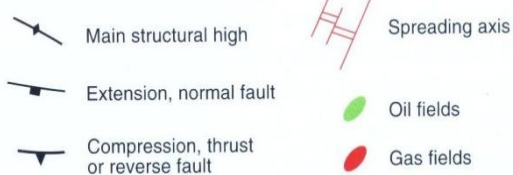


Figure 2.2 Location map of the Arabian Plate showing major tectonic elements of the Arabian Shield and Platform (Al-Husseini,2000).

3. METHODOLOGY

3.1 Receiver Function Method

In general, the receiver function method utilizes coordinate rotation and deconvolution to identify converted phases from seismic discontinuities. To compute a PRF, teleseismic P-waveforms are first rotated from the N-E-Z to the R-T-Z coordinate system using the event's back-azimuth. Then, to remove source and path effects, the data are equalized by deconvolving the Z component from the R and T components, which creates both radial and tangential PRFs (Langston, 1979; Ammon, 1991). PRFs are mainly composed of P-to-S converted energy, containing both refracted phases (Ps) as well as reverberations (PpPs and PpSs+PsPs) generated by reflections between the free surface and discontinuities at depth (Figure 3.1). Positive amplitudes indicate velocity increases with depth while negative amplitudes indicate velocity decreases with depth.

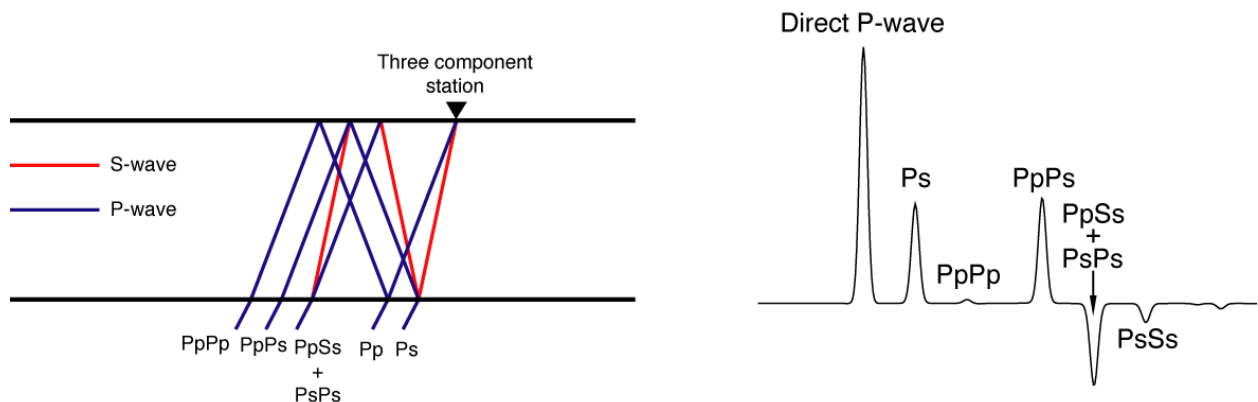


Figure 3.1 – (left) Seismic rays associated to a plane P-wavefront impinging at the base of a uniform velocity layer over a half-space. (right) Receiver function waveform (PRF) for the layer-over-half space model to the left. Note how each peak and trough in the PRF is related to a specific ray-path in the model.

While PRFs have become a routine technique to detect crustal and uppermost mantle discontinuities, S-wave receiver functions (SRFs) are now becoming widely used to detect lithospheric and sub-lithospheric mantle discontinuities. Similar to PRFs, several percent of an incoming S-wave's energy is converted into P-wave energy when a velocity discontinuity is encountered. SRFs, however, tend to be noisier than PRFs since the conversions of interest arrive after the P-wave. SRFs also have longer periods so they do not resolve the fine structure within the crust and mantle lithosphere. However, unlike PRFs, where multiples can mask the conversions of interest, S-to-P conversions upon refraction (Sp) on SRFs can be more clearly identified because they arrive earlier than the direct S phase while all multiples arrive later (Figure 3.2). This is particularly useful when trying to image the lithosphere-asthenosphere boundary (LAB). On PRFs, crustal multiples generally arrive at the same time as the LAB conversion, making the LAB signal almost impossible to detect. On SRFs, the separation of the multiples from the direct converted phases allows the LAB to be more easily imaged (e.g. Farra and Vinnik, 2000; Li et al., 2004; Kumar et al., 2005; 2007; Hansen et al., 2007).

Compared to PRF analysis, a few additional processing steps are necessary to generate a SRF. As before, waveforms are first rotated from the N-E-Z to the R-T-Z coordinate system using the event's back-azimuth. Then, to detect Sp conversions, the data must be rotated around the incidence angle into the SH-SV-P coordinate system (Li et al., 2004). This second rotation is critical because if an incorrect incidence angle is used, noise can be significantly enhanced and converted phases may become undetectable. To make the SRFs directly comparable to PRFs, both the time axes and the amplitudes of the SRFs are reversed (Farra and Vinnik, 2000; Li et

al., 2004; Kumar et al., 2005; 2007).

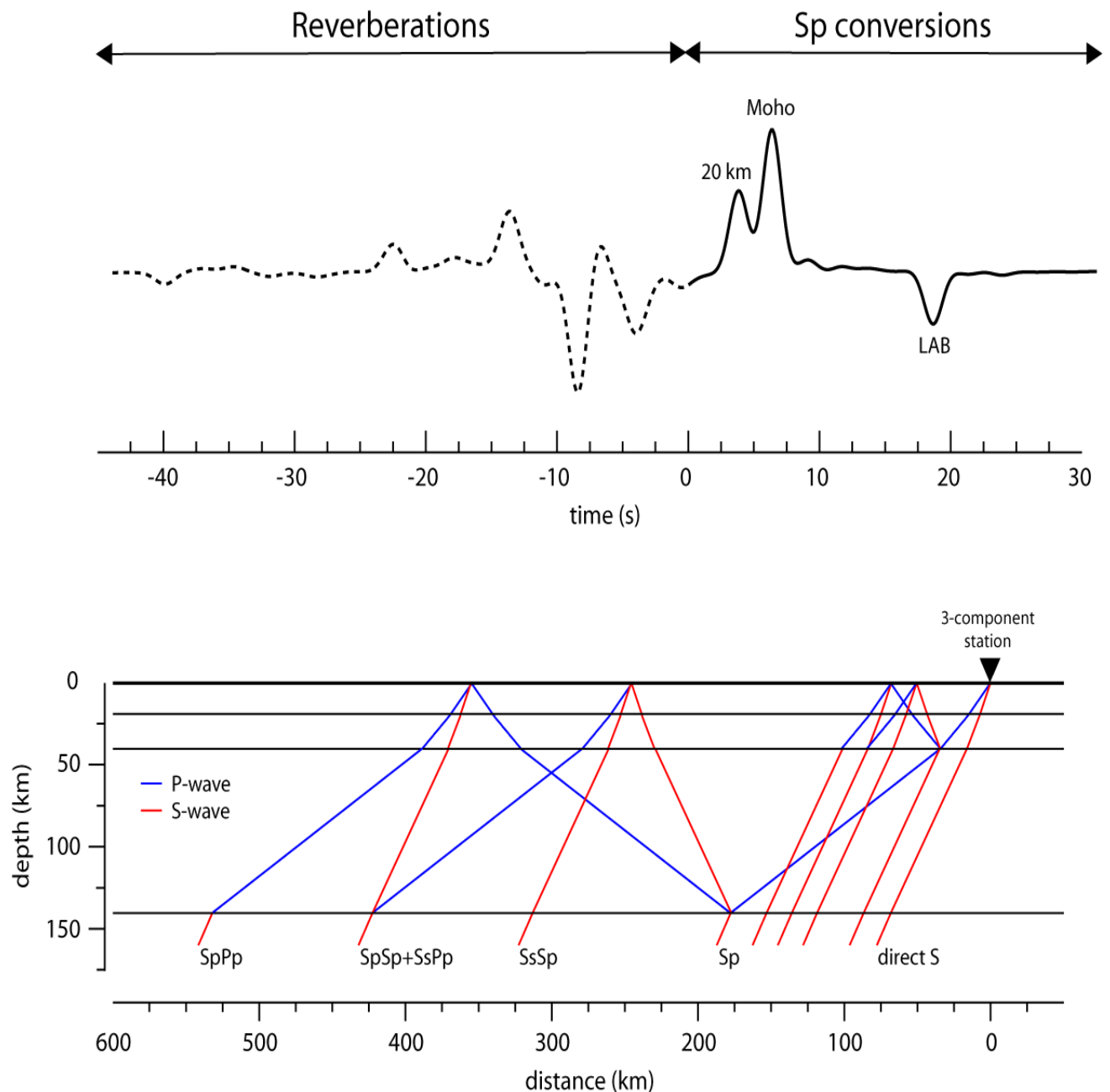


Figure 3.2 – (bottom) Seismic rays associated to a plane S-wave front impinging at the base of a layered velocity model consisting of a 2-layer crust and a lithospheric mantle lid overlying a lower-velocity asthenosphere. (top) S-wave receiver function waveform (SRF) for the model above (plotted in reversed time). Note how the conversions upon refraction at each discontinuity (Sp phases) never interfere with the corresponding multiply reverberated phases.

3.2. Ambient-noise Cross-correlation Method

The correlation of ambient seismic noise is a new and rapidly developing field of seismology. Also referred to as seismic interferometry, it is based on the observation that the Earth's background noise (generated in part by ocean waves, distant earthquakes and multiply scattered coda) includes coherent energy, which can be recovered by observing over long time periods and allowing the incoherent energy to cancel out (Hennino et al., 2001; Weaver and Lobkis, 2001).

The cross correlation of ambient noise between a pair of stations results in a waveform that is identical to the seismogram that would result if an impulsive source located at one of the stations was recorded at the other (Campillo and Paul, 2003; Malcolm et al., 2004; Wapenaar 2004). This means that many of the techniques developed in earthquake seismology can be applied to the correlations themselves. Because the noise correlation function is equivalent to the waveform that would be obtained from an impulsive source located at one of the stations and recorded at the other, many of the techniques developed in earthquake seismology can be applied to the correlations themselves.

A major advantage of the noise-correlation technique is that it strips away dependence on earthquakes or artificial sources for a solution. Problems of source location and velocity heterogeneities outside the region of interest are no longer present, as only the structure between the station pair contributes to the signal. In particular, it allows high-resolution imagery beneath dense seismic networks even in areas of low seismicity. The energy in the correlated waveforms is also quite high in frequency bands which are particularly sensitive to the Earth's crust. Ambient noise correlation does require long, preferably continuous data records as the Green's

function emerges from the incoherent noise. The Green's function is typically lost in the incoherent noise if correlations are shorter than a week (Figure 3.3). Robust estimates of the Green's function require months of data or more.

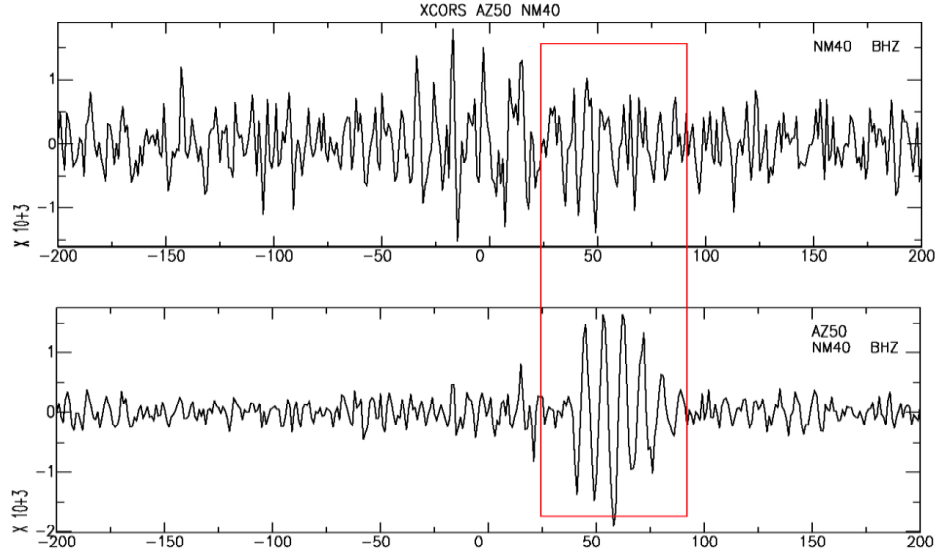


Figure 3.3. The Green's function emerges from the noise as more data are added to the correlation. The (top) trace is the result of correlating the one day's worth of data between a pair of stations separated by 172 km. The (bottom) trace is the result of correlating 7 days' worth of data for the same pair of stations. Notice that the surface wave emerges as more data are added to the stack the stack.

To date, most ambient seismic noise research has focused on group velocity measurements of the resulting surface waves (Moschetti et al., 2007; Shapiro et al, 2005) although more recently, work has begun on measuring the phase velocities (Lin et al, 2008) and amplitudes (Prieto and Beroza 2008 ; Snieder and Safak, 2006; Matzel, 2008) and the new discoveries and methodologies are constantly being developed.

As an example of the resolution power of ambient noise seismology, we show the results of a recent study using the data from a PASSCAL seismic deployment. The

region of interest in that case was the Rio Grande Rift and its relationship to the Colorado Plateau to the west and the Great Plains to the East (Matzel, 2008). In that study, a year's worth of continuous data were correlated resulting in over 1400 new Green's functions. Those waveforms were used as the input in a waveform modeling scheme (Nolet, 1990). 1D models were calculated for each station-pair and the resulting models were then combined to create a tomogram of the crust and uppermost mantle beneath the array. We calculated sensitivity kernels to determine the level of detail obtainable. Vertically, the ambient noise data are particularly sensitive to the upper crust immediately beneath each station and the lower crust along the path between each pair, however, there is also significant sensitivity within the mantle to depths over 100 km. Resolution laterally was on the order of the station spacing. Because the ambient noise data are not dependent on sources from outside the region of interest, the level of detail imaged is far higher than that of traditional methods. We easily identify the upwelling mantle beneath the ridge axis, sharp contrasts in velocity separating the Great Plains and Colorado Plateau as well as mid crustal low velocity zones (presumably hot, partially molten material) underlying the Ruidoso and Zuni uplifts. The resulting image allows us to discriminate between different models of the tectonics of continental rifting.

3.3 Surface wave Dispersion Method

Surface wave dispersion measurements are used to create updated Rayleigh and Love wave group velocity maps which have high-resolution over a wide period band. The amplitude measurements can be used in a tomography for surface wave attenuation. In general, surface wave amplitude measurements are more difficult to

make than group velocity dispersion measurements because information about the source amplitude is needed, requiring a moment tensor solution. Having a focal mechanism is also needed to avoid making measurements at radiation nodes, where amplitudes can be contaminated by multi-pathing.

We are incorporating the amplitudes into a four-phase attenuation tomography of amplitudes. Surface waveform data have already been included in the current tomography (Figures 3.4 and 3.5). Velocity profiles from the source parameter estimation will be used in the inversion. Amplitudes were used to solve for attenuation surfaces (Q_p and Q_s in the crust; Q_p and Q_s in the upper mantle), event source terms, and station site terms. In the process, we modeled the 1D average amplitude attenuation of the region. The attenuation maps were compared and contrasted with our dispersion maps and analyzed for information about the attenuation properties of the sediments, crystalline crust, and upper mantle of the Arabian Peninsula.

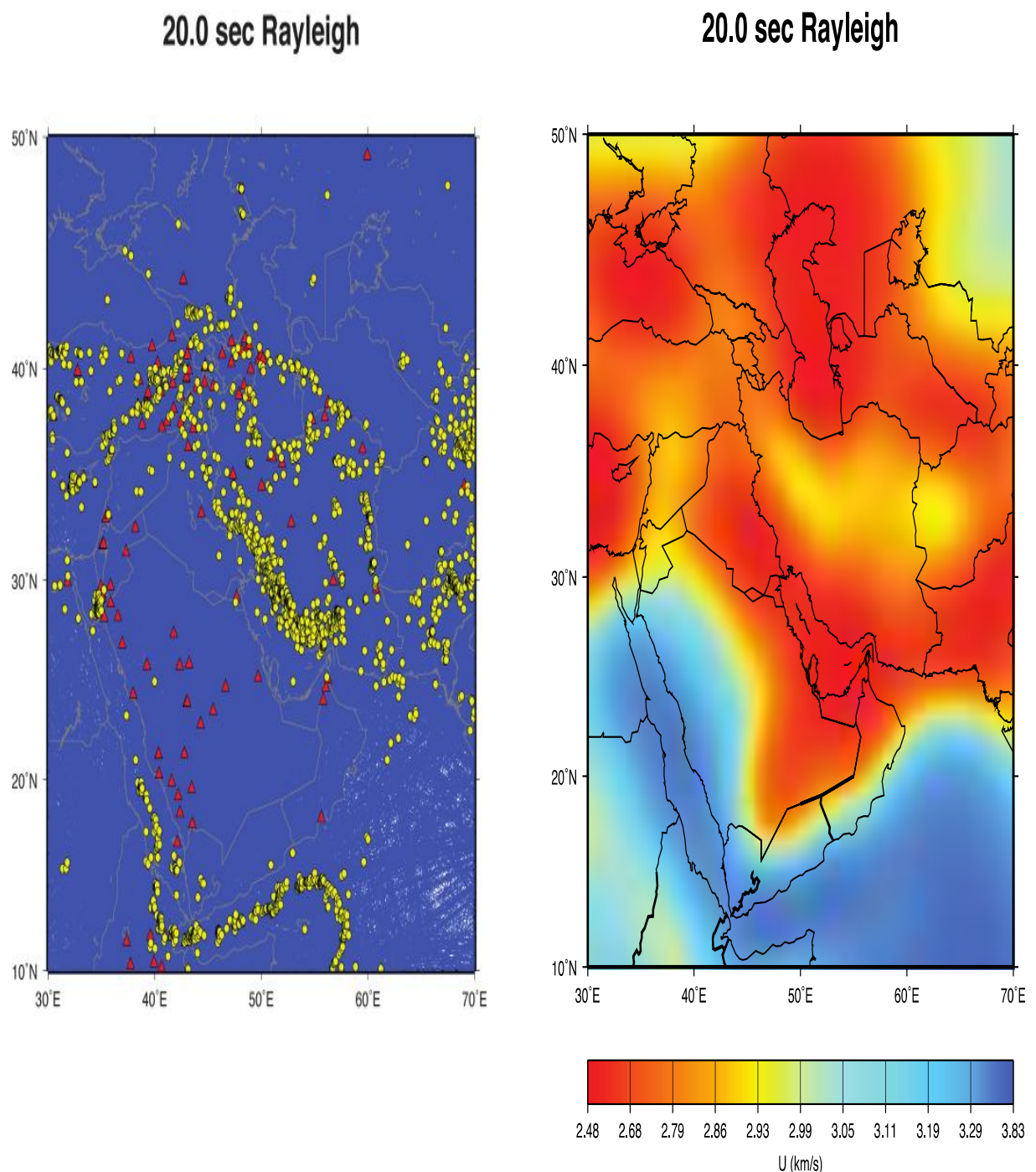


Figure 3.4 Surface Wave Dispersion: (left) path map including regional stations (red) and earthquakes (yellow) used for a tomographic inversion (right) of the Rayleigh wave dispersion data at 20 seconds period. These data have sensitivity to increasingly deeper structure with longer periods (i.e. 15 sec maps with sediments, 50 sec maps with crustal thickness, etc.).

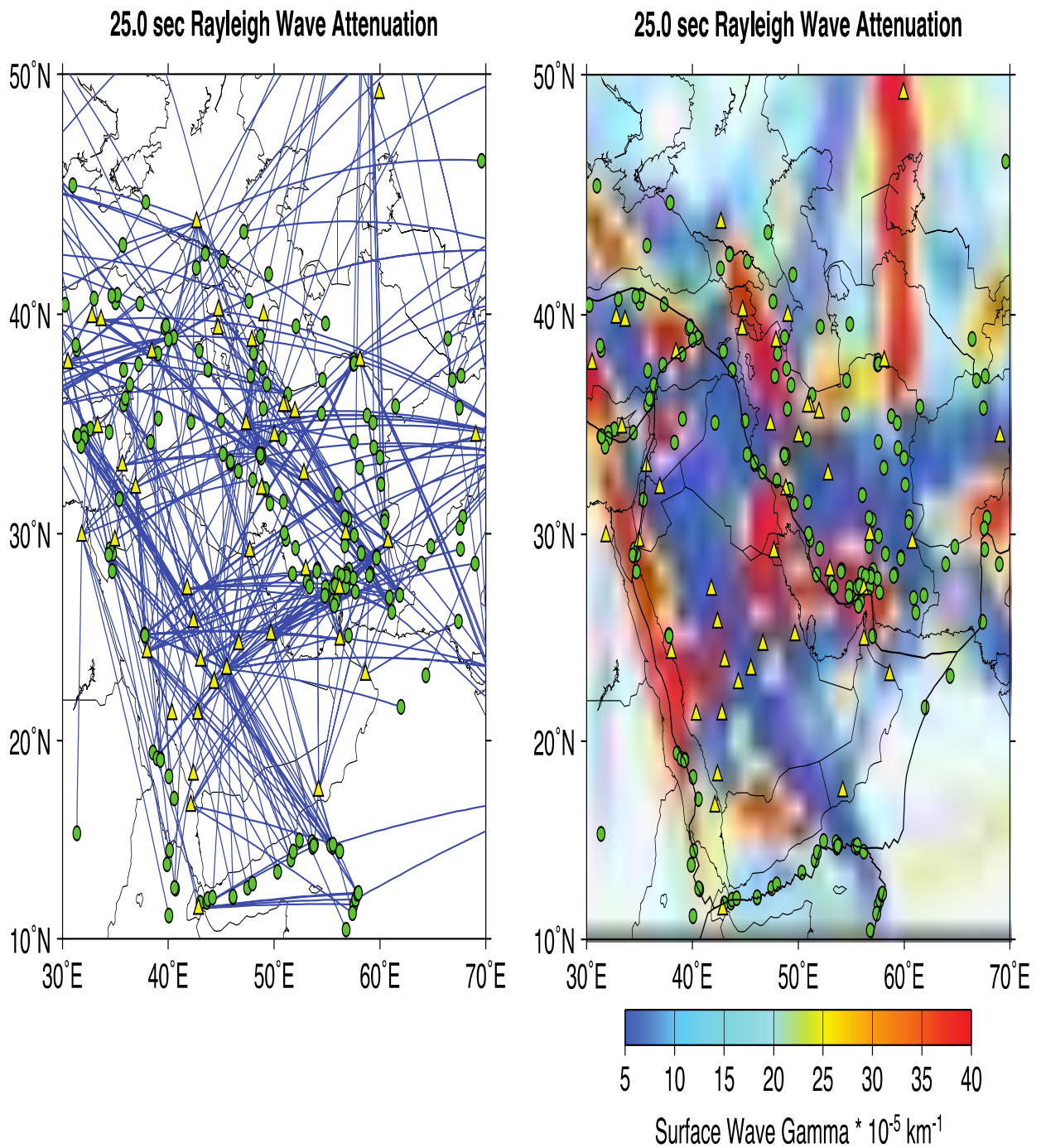


Figure 3.5 Surface Wave Attenuation: Path map (left) and initial result (right) for a surface wave inversion of the 25 second period Rayleigh wave. In these preliminary inversions, we show the attenuation parameter gamma where $g=p/UTQ$.

3.4 Joint Inversion Method

The inversion scheme utilized to jointly invert PRFs, SRFs, and dispersion velocities is exactly the same that Julià et al. (2003) used for the joint inversion of PRFs and dispersion velocities. The only difference is that the computer code has been modified to calculate PRFs or SRFs depending on the receiver function type, in a similar way that group or phase velocities are computed depending on the dispersion velocity type (e.g. Julià et al., 2005). The general equations for the joint inversion, nonetheless, remain the same.

The general equations for the joint inversion of receiver functions and surface-wave dispersion velocities are expressed in matrix form as

$$\begin{bmatrix} sD_s \\ bD_b \\ \sigma\Delta \\ W \end{bmatrix} \mathbf{m} = \begin{bmatrix} s\mathbf{r}_s \\ b\mathbf{r}_b \\ 0 \\ 0 \end{bmatrix} + \begin{bmatrix} sD_s \\ bD_b \\ 0 \\ 0 \end{bmatrix} \mathbf{m}_0 + \begin{bmatrix} 0 \\ 0 \\ 0 \\ W \end{bmatrix} \mathbf{m}_a. \quad (3)$$

The top two rows account for the modeling of the datasets and result from linearizing the forward problems for the dispersion velocities and receiver functions, respectively. The matrices D_s and D_b contain the partial derivatives with respect to \mathbf{m} , the vector of unknowns that defines the velocity profile, and \mathbf{r}_s and \mathbf{r}_b are vectors of residuals that contain the differences between observations and predictions. The subscript s refers to dispersion velocity and the subscript b refers to receiver functions. The linearization of the forward problem turns the inversion scheme into an iterative process that requires a starting model \mathbf{m}_0 . Details on the linearization of the forward problem are given in Ammon et al. (1990) and Julià et al. (2000).

The scalars s and b that multiply the first two rows in eq. (3) are responsible for equalizing the relative importance of the datasets and are defined as

$$s = [p/w_s^2]^{1/2} \quad (4a)$$

$$b = [(1-p)/w_b^2]^{1/2} \quad (4b)$$

where w_s^2 and w_b^2 are weights that equalize the datasets and p is an influence factor that controls the relative contribution to the misfit from each dataset. Julià et al. (2000) suggested using $N\sigma^2$, where N is the number of data points and σ^2 is the variance, to calculate the weights. The influence factor p is typically chosen by trial and error, so that it provides a good balance between matching the dispersion velocities and the receiver functions. Details on the equalization procedure can be found in Julià et al. (2000).

The third row in eq. (3) implements smoothness constraints on the inverted velocity profile \mathbf{m} . The procedure assumes that the earth model is parameterized as a stack of thin layers of constant thickness, and \mathbf{m} is constructed from the S-wave velocity values for each layer. The matrix \square is defined as

$$\Delta = \begin{bmatrix} 1 & -2 & 1 & 0 & \dots \\ 0 & 1 & -2 & -1 & \dots \\ 0 & 0 & 1 & -2 & \dots \\ 0 & 0 & 0 & 1 & \dots \\ \vdots & \ddots & \ddots & \ddots & \dots \end{bmatrix} \quad (5)$$

and constructs the second difference between adjacent model layers. In general, the inversion of noisy data will require stronger smoothness constraints to prevent noise from mapping into the velocity-depth profiles. The parameter σ controls the

importance of the smoothness constraints in the resulting velocity profile and is chosen to provide a good balance between matching the observations and smoothing the velocity profiles (Ammon et al., 1990).

Finally, the last row in eq. (3) incorporates *a priori* constraints on the velocity profile \mathbf{m} . This row fixes the S-wave velocity value of select model layers to values prescribed in vector \mathbf{m}_a . This is achieved through the diagonal weight matrix W , by giving non-zero values to the corresponding weights in the matrix.

The performance of the joint inversion scheme described above was tested through an inversion of synthetic “data”, where synthetic PRF, SRF, and fundamental-mode, Rayleigh-wave group velocity data were computed for the simple earth model displayed in Figure 3.1. The receiver function waveforms are calculated from the deconvolution of synthetic seismograms obtained after propagating a plane wave through the earth model with a matrix-propagation algorithm (e.g. Kennett, 1983). P-wave synthetics assumed a ray parameter of 0.05 s/km while S-wave synthetics assumed a ray parameter of 0.10 s/km. The PRF was windowed between -5 and 30 s before and after the direct P-wave arrival and low-pass filtered with a Gaussian filter of width 2.5 ($f_c \leq 1.2$ Hz); the SRF was windowed between 0 and 30 s after the direct S-wave (after time-reversing the synthetic seismograms) and low-pass filtered with a Gaussian filter of width 1.0 ($f_c \leq 0.5$ Hz). The group velocities were obtained after a grid-search solution of the dispersion equation, as implemented in the DISPER80 package of Takeuchi and Saito (1972), for periods between 10 and 170 s. note that the parameters for the synthetic “observations” were chosen to lay within the range of values commonly found in real observations.

The synthetic observations are then inverted using the joint inversion scheme in eq. (3). The starting model consisted of a stack of 2.5 km-thick layers of fixed thickness defining a half-space of 4.0 km/s in S-wave velocity. V_p/V_s ratios in the starting model were set to those of the true model within the corresponding depth-ranges and densities were computed with the same empirical relationship implemented in the joint inversion code (Berteussen, 1977). The influence factor was set to $p=0.5$ and the smoothness parameter was set to $\sigma=0.2$. A non-zero smoothness value is required to stabilize the inversions below 80 km depth, even though the “data” are noise-free. Both Ps conversions and multiples generated at discontinuities above ~80 km are recorded within the 30 s PRF time window, but only Ps conversions will be present for deeper discontinuities. This is important as the reverberations sample the discontinuities through topside reflections and, at finite frequencies, have higher resolution than Ps conversions (Richards, 1972; Bostock, 1999). Thus, the 2.5 km-thick layers cannot be resolved below 80 km depth and need to be additionally constrained.

Figure 3.6 shows the inverted models and the corresponding predictions as the iterations progress. After the first iteration the match between “observed” and predicted dispersion velocities improve dramatically, and this resulted in an inverted model with average velocities close to those of the true model. The predicted receiver functions, however, do not match the peaks and troughs correctly, which translates into seismic discontinuities being shifted in the inverted models with respect to the true model.

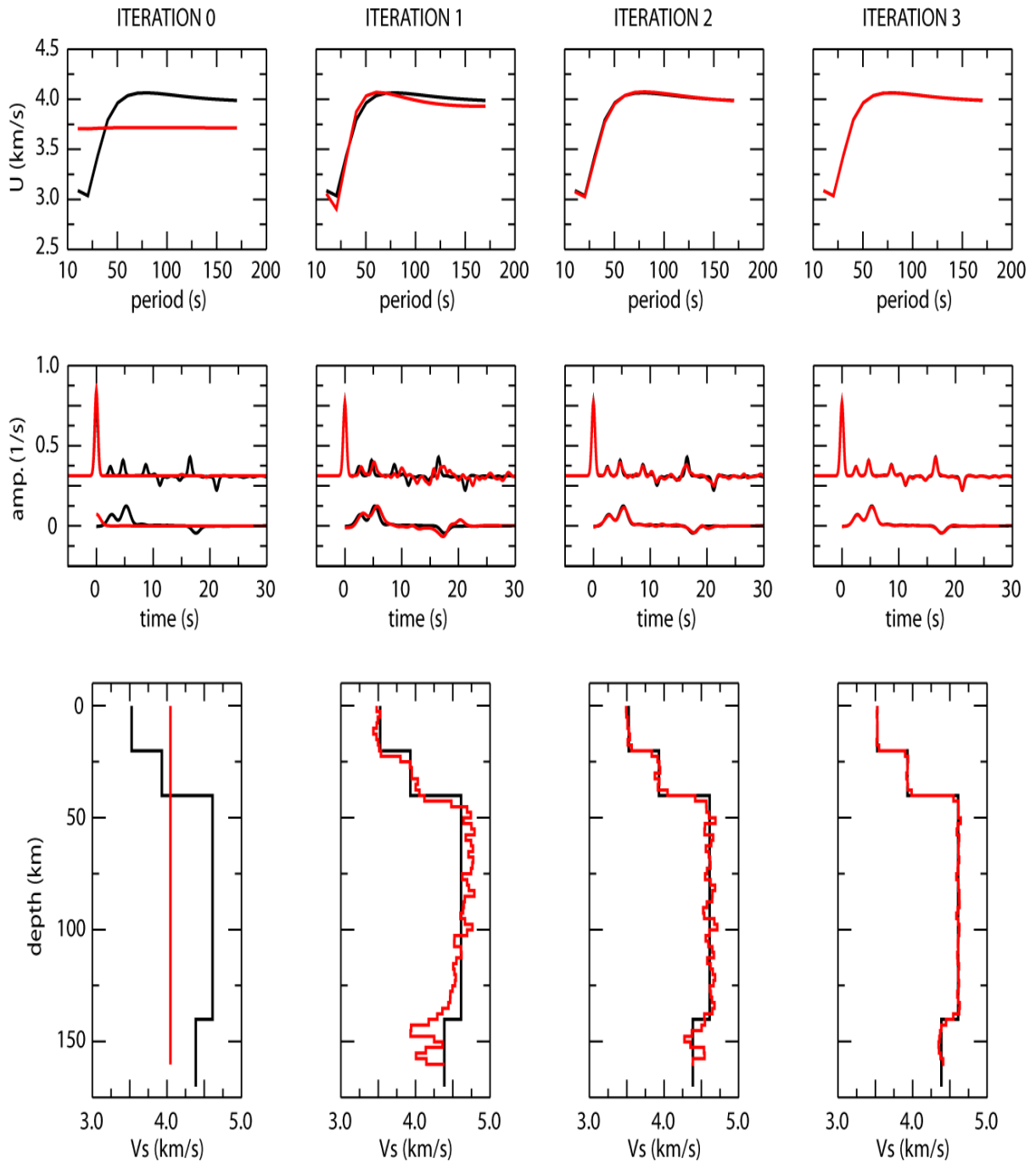


Figure 3.6 - Joint inversion of noise-free, synthetic PRF, SRF, and group velocity “observations”. The top panels display group velocities, the middle panels display PRF and SRF waveforms, and the bottom panels display S-wave velocity models. The black lines represent the synthetic “observations” and the “true” velocity models while the red lines display the inverted velocity model and the corresponding prediction after each iteration (indicated on top). Note how the final model (iteration 3) resolves the sharpness of the discontinuities at 20 and 40 km depth but not the sharpness of the discontinuity at 140 km depth.

After the second iteration the match between “observed” and predicted receiver functions improves, and the depths of the discontinuities are placed at the expected depths. Subsequent iterations fine-tune the inverted models. The final model displays an almost perfect match to the “true” model, except for the sharpness of the LAB. The sharpness of a discontinuity is best constrained by the reverberations between the free-surface and the discontinuity Julià (2007), and for the 140 km deep LAB in the “true” model they lie outside the 30 s time window considered for the PRF.

4. RESULTS & DISCUSSION

4.1 Computation of P-wave receiver functions

We computed PRFs and SRFs for all the broadband stations within the Saudi seismic networks. We followed the approaches of Langston (1979) and Sodoudi (2005) for the computation of PRFs and SRFs, respectively, along with the iterative deconvolution method of Ligorría and Ammon (1999). The number of receiver function waveforms depended on the recording time window and quality of the broadband station.

The data set for the computation of PRFs consisted of teleseismic P-waveforms for seismic sources located between 30° and 90° epicentral distance and with $5.5 m_b$ or larger recorded at broadband seismic stations in Saudi Arabia (Figure 4.1). A summary of the data gathered is given in Table 1, which lists the location, recording time period, and number of selected waveforms for each station. The number of downloaded waveforms is quite variable and ranges from 33 at station SGS21 to 3,870 at station RAYN. This variation in the number of waveforms reflects mostly variations in the amount of data made available by KACST and SGS, but also results from gaps in the continuous data archive from these two institutions.

The selected waveforms were processed to obtain P-wave receiver function estimates for all the stations (Langston, 1979). First, the waveforms were windowed 10 s before and 110 s after the teleseismic P-wave arrival, detrended, and tapered with a cosine taper function of 5% width. The waveforms were then high-pass filtered with a 3-pole Butterworth filter at 20 s to remove long-period noise, and

decimated to 10 samples per second after low-pass filtering below 8 Hz to avoid aliasing. The filtered waveforms were rotated into the ZRT coordinate system and the vertical component (Z) was then deconvolved from the radial (R) and transverse (T) components to produce radial and transverse receiver functions, respectively, for each event. The deconvolution was implemented through the iterative time-domain procedure of Ligorría and Ammon (1999) with 500 iterations, at two overlapping Gaussian widths of 2.5 ($f_c \leq 1.25$ Hz) and 1.0 ($f_c \leq 0.5$ Hz) to remove high-frequency noise. The computation of PRFs at two overlapping frequency bands helps constrain gradational boundaries versus sharp discontinuities during the modeling of receiver function amplitudes, as explained in our report of Task 3.

A quality control was applied to the deconvolved waveforms to select high-quality receiver functions for our analysis. First, the performance of the deconvolution process was assessed by computing the root-mean-square (RMS) misfit between the original radial waveform and the recovered radial waveform obtained after convolving the receiver function back with the vertical component. Receiver functions with percent recoveries under 85% were rejected. Second, transverse receiver functions were examined and the corresponding radial receiver functions were rejected if significant signal was observed. This step ensured that radial receiver functions were not significantly disrupted by small-scale lateral heterogeneities under the recording station. Finally, the remaining radial receiver functions were overlapped to visually identify outliers, which were removed from the data set. The final number of selected PRFs for each station and frequency band is reported in Table 1.

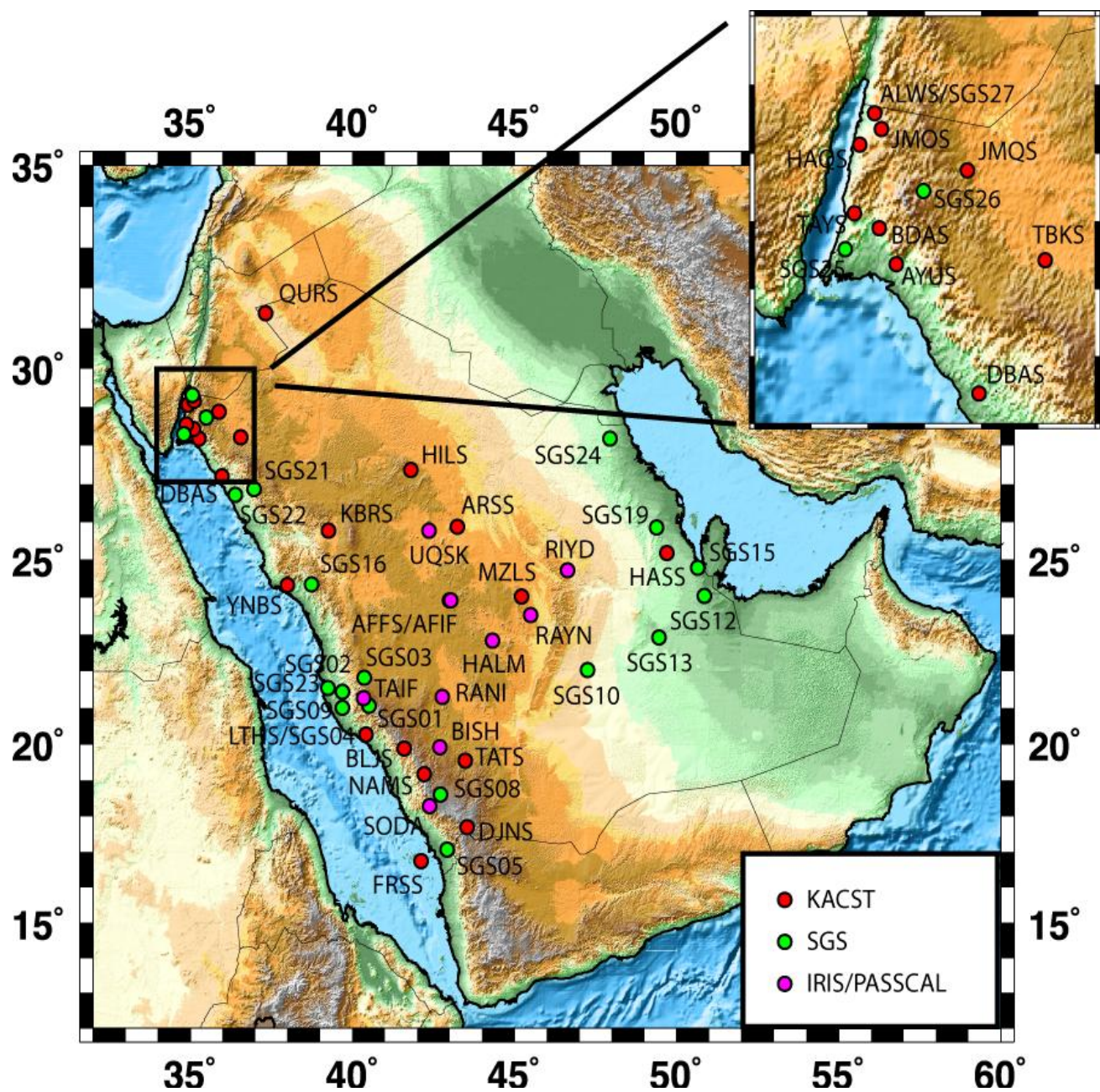


Figure 4.1 – Topographic map of the Arabian Peninsula showing the broadband stations. The stations belong to three different networks: King Saud Center for Science and Technology (KACST), Saudi Geological Survey (SGS), and the Incorporated Research Institutes for Seismology (IRIS).

Table 1 – Stations and waveform statistics for the selected dataset.

Station name	Latitude (deg)	Longitude (deg)	Start Time (year.jday)	End Time (year.jday)	P-wave	PRFs (a=2.5)	PRFs (a=1.0)	S-wave	SRFs (a=1.0)
KACST Network									
affs	23.927	43.001	2000.125	2006.300	1350	88	62	177	9
alws	29.310	35.065	1999.312	2006.029	1533	84	94	188	9
arss	25.881	43.237	2001.145	2005.360	186	22	18	19	3
ayus	28.189	35.269	2000.133	2006.296	1170	68	56	159	6
bdas	28.432	35.101	1999.312	2006.296	1407	67	61	179	6
bljs	19.881	41.599	2000.241	2006.300	1689	104	90	153	6
djns	17.707	43.543	2001.021	2006.300	1449	86	89	157	5
frss	16.739	42.114	2002.062	2006.300	828	34	49	85	1
haqs	29.055	34.930	1999.312	2006.296	1470	83	71	181	7
hass	25.190	49.694	2000.088	2006.300	1440	93	78	305	20
hils	27.384	41.792	2000.088	2006.300	1638	139	116	234	14
jmos	29.169	35.109	2000.156	2006.296	1437	71	75	178	4
jmqz	28.886	35.878	2002.064	2006.296	762	41	35	102	2
kbrs	25.789	39.262	2000.202	2005.175	177	25	23	7	1
lths	20.275	40.411	2000.241	2006.120	807	34	35	49	5
mzls	24.028	45.207	2004.007	2006.300	1305	87	63	208	4
nams	19.171	42.208	1999.312	2006.300	735	62	54	86	4
qurs	31.386	37.324	2000.125	2006.292	1182	58	55	179	5
tats	19.541	43.478	2000.156	2006.300	1245	79	73	148	6
tays	28.551	34.872	2000.125	2006.296	651	37	35	85	3
tbks	28.225	36.549	1999.312	2006.296	1641	93	81	181	5
ynbs	24.340	37.992	1999.312	2006.296	1146	64	55	116	5
IRIS-PASSCAL Network									
afif	23.931	43.040	1995.328	1997.052	363	53	34	48	6
halm	22.845	44.317	1995.328	1997.052	543	74	64	25	5
rani	21.312	42.776	1995.344	1997.057	333	30	20	20	10
rayn	23.522	45.501	1995.337	2008.354	3870	456	335	164	37
riyd	24.722	46.643	1996.076	1997.059	438	33	28	36	8
soda	18.292	42.377	1995.344	1997.057	516	55	42	11	0
taif	21.281	40.349	1996.158	1996.240	90	11	10	4	1
uqsk	25.789	42.360	1996.163	1997.052	387	31	22	16	1
SGS Network									
sgs01	21.058	40.518	2006.259	2007.216	168	30	28	17	1
sgs02	21.449	39.691	2006.259	2007.216	183	31	28	16	1
sgs03	21.834	40.359	2006.321	2007.216	153	27	25	16	1
sgs04	20.276	40.411	2006.359	2007.216	144	25	22	15	1
sgs05	17.068	42.917	2006.359	2007.216	123	22	24	13	2
sgs08	18.606	42.719	2007.125	2007.216	69	12	9	39	0
sgs09	21.005	39.683	2006.109	2007.076	138	26	21	14	4
sgs10	22.039	47.245	2006.109	2007.216	117	22	17	15	3
sgs12	24.046	50.846	2006.109	2007.216	246	46	44	41	8
sgs13	22.927	49.462	2006.109	2007.216	234	43	36	39	9
sgs15	24.798	50.644	2006.109	2007.216	240	40	36	40	7
sgs16	24.358	38.743	2006.109	2007.216	231	43	43	23	2
sgs19	25.869	49.376	2006.109	2007.216	246	42	38	42	9
sgs21	26.867	36.958	2007.197	2007.216	33	7	5	2	0
sgs22	26.732	36.393	2006.109	2007.216	225	43	36	23	3
sgs23	21.557	39.236	2006.109	2007.216	246	50	42	39	7
sgs24	28.187	47.942	2006.109	2007.216	255	59	48	43	9
sgs25	28.300	34.797	2006.109	2007.216	222	29	26	28	1
sgs26	28.735	35.492	2006.109	2007.216	243	50	41	31	4
sgs27	29.300	35.062	2006.109	2007.216	246	48	45	31	3

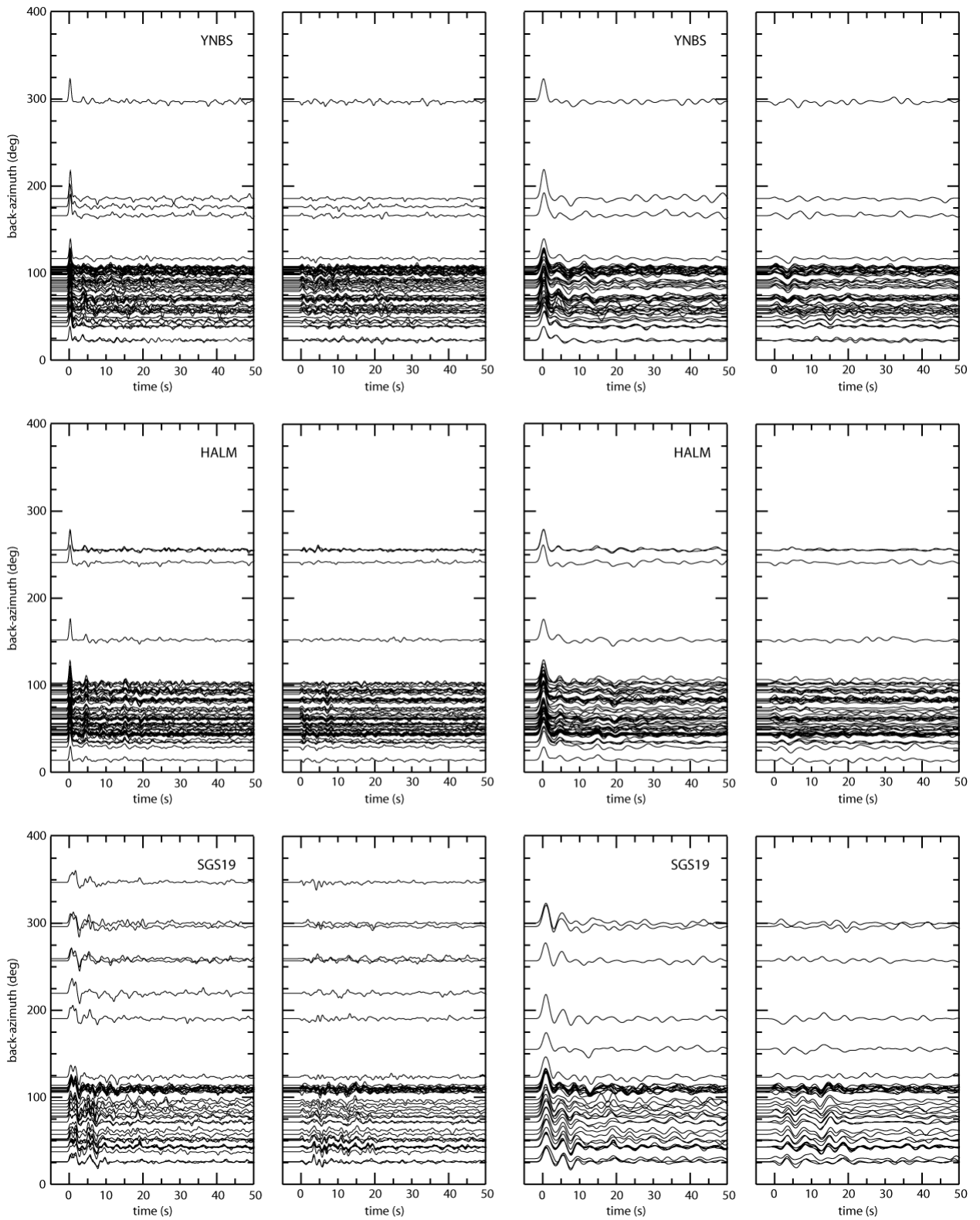


Figure 4.2 – Sample radial and transverse receiver function waveforms (PRFs) for three stations in the Arabian Peninsula. Left panels correspond to a Gaussian width of 0.5 ($f_c \leq 1.25$ Hz) and right panels correspond to a Gaussian width of 1.0 ($f_c \leq 0.5$ Hz).

Examples of PRF waveforms are displayed in Figure 4.2 for select stations in the shield and platform. Note the small amplitudes in the transverse receiver function components compared to the corresponding amplitude in the radial components. Small transverse amplitudes are diagnostic for a laterally homogeneous medium under the recording station, which is an important assumption during the development of lithospheric velocity models for the Arabian peninsula of Task 3. Also note the clear Ps, PpPs and PpSs arrivals in the PRF waveforms. These arrivals are generated after the interaction of the teleseismic P-waveform with the crust-mantle boundary and are critical to tightly constrain the thickness and bulk Vp/Vs ratio of the crust in the lithospheric velocity models.

The full set of computed receiver functions for all the stations utilized in this project can be found in Appendix A.

4.2 Crustal thickness and bulk Vp/Vs ratios

Following the suggestions given by reviewer #2 on the 2nd progress report of this project, we have developed Vp/Vs ratio estimates for the Arabian crust (previously, it was assumed a uniform value of 1.75) to help constrain velocity structure in the joint inversion models developed in Task 3. The PRFs contain a wealth of information about the structure beneath the receiver. In particular, the Ps arrival time of the converted phase at the Moho can be used to determine the crustal thickness assuming an average crustal P-wave velocity (e.g. Zandt et al., 1995) and, when clear multiples are present, both the Moho depth and Vp/Vs ratio can be determined (Zhu and Kanamori, 2000).

We have applied the hk-stacking technique of Zhu and Kanamori (2000) to the high-

frequency ($f_c \leq 1.25$ Hz) PRFs to obtain thickness and bulk Vp/Vs ratios for the crust under each recording station in Saudi Arabia. The technique consists of a transformation from a time-domain representation of the PRFs into a new domain, which is a function of the depth to the interface (H) and Vp/Vs (k) ratio. The transformation is described as

$$s(H, k) = \sum [w_1 r f_i(t_1) + w_2 r f_i(t_2) - w_3 r f_i(t_3)], \quad (1)$$

where $r f_i(t_j)$ are the receiver function amplitudes at $t=t_j$, w_i are *a priori* weights such that $\sum w_i = 1$, and the summation extends to all the PRFs for a given station.

The times t_j are given by

$$t_1 = t_{Ps} - t_p = H (\Lambda_\beta - \Lambda_a) \quad (2a)$$

$$t_2 = t_{PpSs} - t_p = H (\Lambda_\beta + \Lambda_a) \quad (2b)$$

$$t_3 = t_{PsPs} - t_p = 2H \Lambda_\beta, \quad (2c)$$

where Λ is the vertical slowness (obtained through a trial k value and an *a priori* value for crustal P-wave velocity) and H is a trial depth. During the transformation, the amplitudes of P-to-S conversions at the computed times t_j will interfere constructively only when the trial H and Vp/Vs ratios coincide with the depth to and Vp/Vs ratio above an actual discontinuity. The results on crustal thickness and Vp/Vs ratio for the broadband stations in Saudi Arabia are displayed in Figure 4.3 and listed in Table 2, along with 2σ confidence bounds obtained after bootstrapping the original dataset with 200 replications (Efron and Tibshirani, 1991) and other relevant information. The detailed hk-stacking analysis for each station, which include the hk-stacking surface and P-to-S phase moveout diagrams, can be found in Appendix A.

Table 2- Point measurements of crustal thickness (H) and V_p/V_s ratio from hk- stacking for broadband stations in Saudi Arabia.

Station	PRFs	VP(km/s)	W1	W2	W3	H(km)	V_p/V_s	Cor(%)
KACST NETWORK								
affs	88	6.5	0.4	0.3	0.3	36.2 ± 0.4	1.73 ± 0.01	-84.4
arss	22	6.5	0.4	0.3	0.3	38.8 ± 0.4	1.75 ± 0.01	-86.2
ayus	68	6.5	0.4	0.3	0.3	29.3 ± 0.5	1.71 ± 0.02	-86.7
bdas	67	6.5	0.5	0.0	0.5	27.7 ± 0.8	1.75 ± 0.03	-94.3
bljs	104	6.5	0.4	0.3	0.3	38.6 ± 0.3	1.71 ± 0.01	-85.1
djns	86	6.5	0.5	0.5	0.0	42.7 ± 1.1	1.76 ± 0.04	-76.3
haqs	83	6.5	0.5	0.5	0.0	28.2 ± 0.5	1.80 ± 0.04	-82.1
hass	93	6.5	0.5	0.5	0.0	43.7 ± 0.2	1.77 ± 0.01	-85.7
hils	139	6.5	0.4	0.3	0.3	37.1 ± 0.2	1.78 ± 0.01	-76.2
joms	71	6.5	0.5	0.5	0.0	32.0 ± 1.9	1.77 ± 0.05	-98.5
jmqs	41	6.5	0.5	0.5	0.0	38.9 ± 0.9	1.76 ± 0.03	-80.4

kbrs	25	6.5	0.4	0.3	0.3	35.1 ± 0.5	1.74 ± 0.02	-89.4
mzls	87	6.5	0.4	0.3	0.3	41.7 ± 0.8	1.78 ± 0.02	-90.5
nams	62	6.5	0.4	0.3	0.3	41.6 ± 0.4	1.70 ± 0.01	-78.6
qurs	58	6.5	0.4	0.3	0.3	34.2 ± 0.3	1.71 ± 0.01	-68.5
tats	79	6.5	0.4	0.3	0.3	39.7 ± 0.3	1.80 ± 0.01	-89.4
tays	37	6.5	0.4	0.3	0.3	28.7 ± 0.5	1.71 ± 0.02	-90.6
tbks	93	6.5	0.4	0.3	0.3	35.7 ± 0.4	1.76 ± 0.01	-70.4
ynbs	64	6.5	0.4	0.3	0.3	24.8 ± 0.7	1.93 ± 0.05	-88.8
IRIS NETWORK								
afif	53	6.5	0.4	0.3	0.3	36.1 ± 0.3	1.73 ± 0.01	-80.8
halm	74	6.5	0.4	0.3	0.3	36.1 ± 0.3	1.76 ± 0.01	-96.7
rani	30	6.5	0.4	0.3	0.3	37.1 ± 0.8	1.75 ± 0.03	-91.6
rayn	456	6.5	0.4	0.3	0.3	40.2 ± 0.1	1.76 ± 0.00	-86.0
soda	55	6.5	0.4	0.3	0.3	38.2 ± 0.3	1.73 ± 0.01	-88.0
taif	11	6.5	0.4	0.3	0.3	37.2 ± 0.6	1.75 ± 0.03	-91.5
uqsk	31	6.5	0.4	0.3	0.3	36.3 ± 0.4	1.76 ± 0.02	-80.5

SGS								
NETWORK								
sgs01	30	6.5	0.4	0.3	0.3	39.3 ± 0.7	1.73 ± 0.03	-93.4
sgs02	31	6.5	0.4	0.3	0.3	28.0 ± 0.6	1.73 ± 0.03	-95.6
sgs03	27	6.5	0.4	0.3	0.3	37.1 ± 0.5	1.68 ± 0.02	-95.3
sgs08	12	6.5	0.5	0.5	0.0	39.3 ± 1.6	1.77 ± 0.03	-57.5
sgs09	26	6.5	0.5	0.5	0.0	25.3 ± 0.7	1.81 ± 0.03	-87.0
sgs12	46	6.5	0.5	0.5	0.0	44.9 ± 0.4	1.71 ± 0.01	-84.1
sgs13	43	6.5	0.4	0.3	0.3	45.6 ± 0.7	1.79 ± 0.01	-93.2
sgs16	43	6.5	0.4	0.3	0.3	30.5 ± 0.4	1.79 ± 0.02	-90.4
sgs19	43	6.5	0.4	0.3	0.3	47.7 ± 0.3	1.65 ± 0.01	-55.6
sgs21	7	6.5	0.4	0.3	0.3	35.6 ± 1.7	1.71 ± 0.06	-92.8
sgs22	43	6.5	0.4	0.3	0.3	29.6 ± 0.5	1.69 ± 0.02	-87.50
sgs23	50	6.5	0.4	0.3	0.3	46.2 ± 0.5	1.77 ± 0.01	-84.4
sgs24	59	6.5	0.5	0.5	0.0	47.4 ± 1.3	1.81 ± 0.08	-98.8
sgs25	29	6.5	0.4	0.3	0.3	39.5 ± 1.6	1.75 ± 0.05	-89.4
sgs27	48	6.5	0.4	0.3	0.3	33.1 ± 1.0	1.63 ± 0.04	-86.1

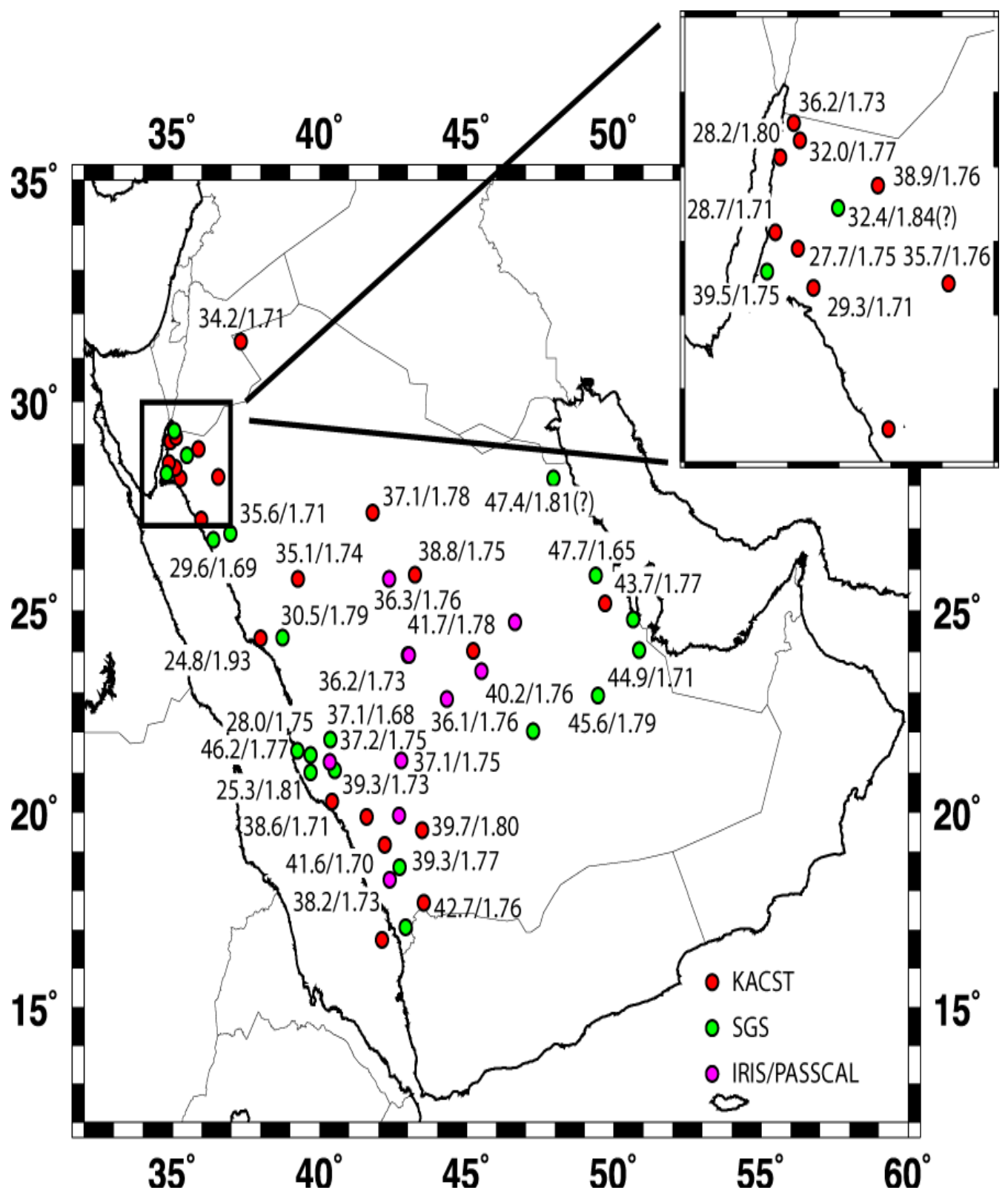


Figure 4.3 – Map displaying variation in point measurements of crustal thickness (H) and Vp/Vs ratios in the Saudi Arabia. Each measurement is shown next to the station location as hh.h/v.vv, where hh.h is crustal thickness and v.vv is Vp/Vs ratio. Confidence bounds for the measurements can be found in Table 2. Note the stations are color-coded according to seismic network.

4.3 Computation of S-wave receiver functions

The data set for the computation of SRFs consisted of teleseismic S-waveforms for seismic sources located between 60° and 82° epicentral distance and with 6.0 m_b or larger recorded at broadband seismic stations in Saudi Arabia. At a given station, the converted Sp phase arrives earlier than the direct S phase, and S-to-P conversions upon refraction (Sp) across shallow discontinuities are best observed within the distance range mentioned above (e.g. Wilson et al., 2006). A summary of the data gathered is given in Table 1, along with PRF information. The number of downloaded waveforms is quite variable and ranges from 7 at station LTHS to 305 at station HASS. As with PRFs, this variation reflects mostly variations in the amount of data made available by KACST and SGS, but also results from gaps in the continuous data archive from these two institutions.

To compute the SRFs, the teleseismic S-waveforms were windowed 110 s before and 10 s after the teleseismic S-wave arrival, detrended, and tapered with a cosine taper function of 5% width. The waveforms were then high-pass filtered with a 3-pole Butterworth filter at 20 s to remove long-period noise, and decimated to 10 samples per second after low-pass filtering below 8 Hz to avoid aliasing. Following standard practice in SRF studies (e.g. Hansen et al., 2007), the filtered waveforms were rotated into the local ray-coordinate system (LQT system). First, a rotation from the ZNE system into the great-circle path (ZRT system) was performed using the event's back-azimuth. Second, a rotation was performed from the ZRT system into the LQT system, using the method of Sodoudi (2005). In this method, R-Z seismograms for a given event are rotated through a series of incidence angles to create sets of quasi-SV and quasi-P data. Each quasi-SV component is then

deconvolved from the corresponding quasi-P component using Ligorría and Ammon's (1999) iterative time domain method, with 500 iterations. The optimal incidence angle for rotation into the SH- SV-P coordinate system is the angle that minimizes the direct S-wave energy on the P- component. On the time-reversed receiver functions, the direct S arrival is at 0 s. Therefore, the receiver function of interest is the one whose mean amplitude is closest to zero at zero time. The deconvolution was implemented at Gaussian widths of 1.0 ($f_c \leq 0.5$ Hz) to remove high-frequency noise.

Once receiver functions are generated for all events at a given station, it is also important to high-grade the dataset using a number of quality control criteria. Since SRFs tend to be noisier than PRFs, the SRFs are compared to PRFs at the same station to identify the Moho conversion. Only SRFs that display a clear Moho conversion at the appropriate time are used for further analysis. Also, the amplitude of the Moho conversion can be examined. Using assumed, average velocities for the crust and upper mantle, forward modeling can be used to predict the expected Moho amplitude. If the amplitude of the Moho conversion on the SRF is too large or too small, indicating an unrealistic velocity contrast across the crust-mantle boundary, the SRF is discarded. Generally, the percentage of useable, high-quality data obtained in SRFs analysis is comparable to that obtained in PRF analysis. However, fewer events overall are available for SRFs given the more restricted distance range used, so a fairly large initial dataset is required. As explained in our report of Task 3, some stations did not include enough data to compute stable SRF averages to be used in the joint inversion.

Figure 4.4 displays SRF waveforms for those stations in Saudi Arabia for which a stable waveform pattern emerged out of the superposition of the computed SRFs.

4.4 Lithospheric thickness

Although not contemplated in the work plan for Task 1, we have stacked and migrated SRFs into the depth domain in order to investigate possible occurrences of negative-polarity Sp conversions that may be suggestive of an S-to-P conversion at the base of the lithosphere. The lithosphere-asthenosphere boundary (LAB) is likely to have a thermal origin and therefore be characterized by a gradational transition rather than a sharp discontinuity (e.g. Karato, 2003). This may reduce the amplitude of the Sp conversion in the SRFs and make it not identifiable in individual SRF waveforms.

First, phase-moveout curves were computed for each event-station pair for a range of Sp conversion depths ranging between 0 and 300 km at 2 km depth intervals. The phase-moveout curves were obtained after ray-tracing through the ak135 global earth model (Kennett et al., 1994) using the TauP utility [Crotwell et al., 1999]. Second, the amplitudes for all the receiver functions were averaged for common Sp conversion depths along the computed phase-moveout curves. Finally, the migrated SRFs were produced by plotting the averaged amplitudes against conversion depth. Confidence bounds were also computed after bootstrapping across the receiver function data set with 200 replications (Efron and Tibshirani, 1991).

Figure 4.5 displays the SRF stacks for those stations that had individual SRFs with a coherent crustal pattern (as explained in the previous section). Some stations do display small-amplitude Sp conversions at depths that vary between 60 km and 200

km. In general, the stations that are located in the interior of the shield display a negative amplitude Sp conversion under 150 km depth (MZLS, RAYN) or no identifiable Sp conversion at all (AFFS, HILS, QURS), while those stations located along the Red Sea and Gulf of Aqaba (AYUS, BDAS, BLJS, HAQS), and also those near Arabian Gulf (HASS, SGS12, SGS15, SGS19) display negative Sp conversions at shallower depths around 60-80 km.

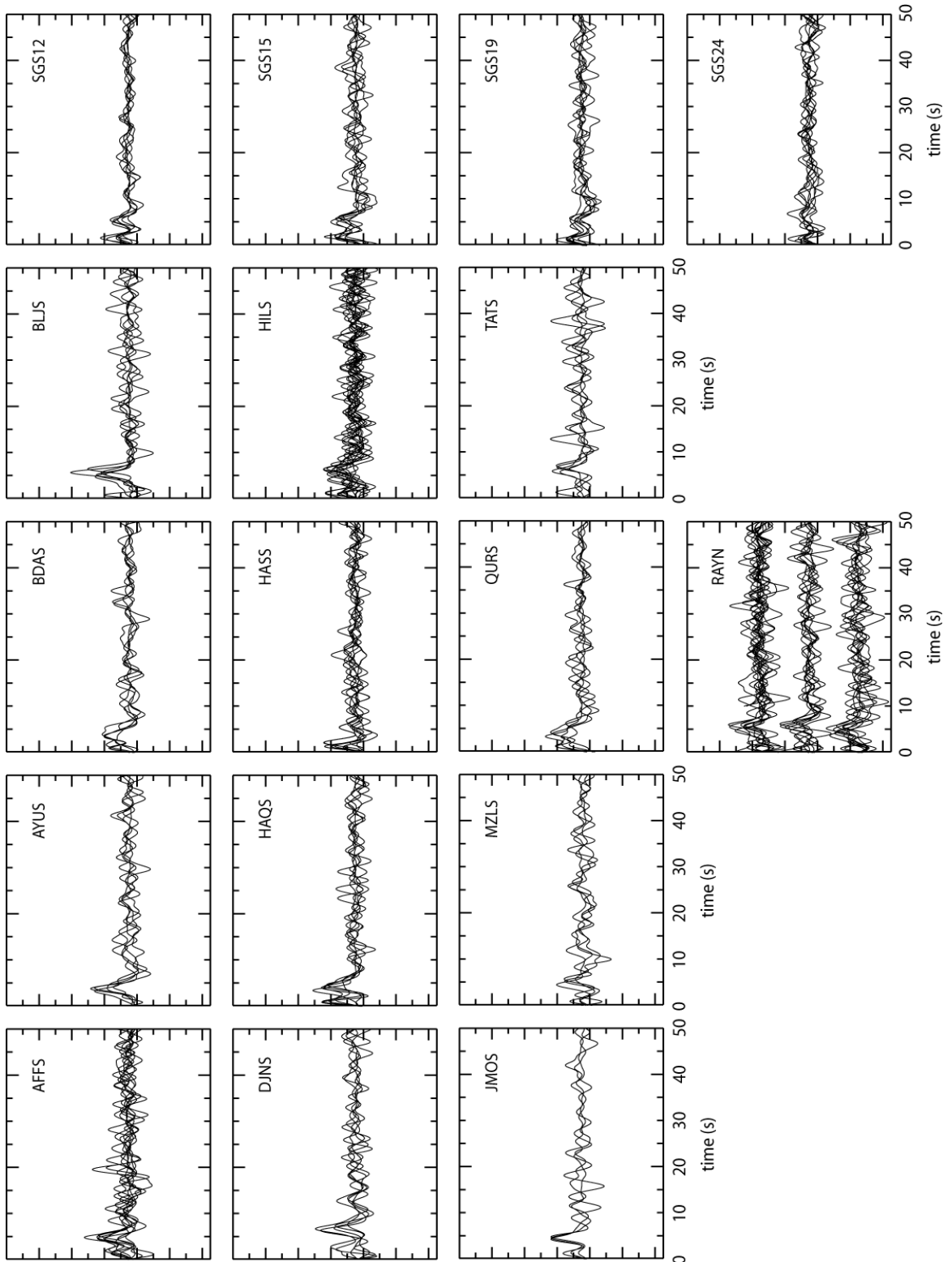


Figure 4.4 . Overlay of S---wave receiver functions obtained at each broadband station considered in this study. The overlay shows a clear consistent peak at $\sim 5\text{--}6$ seconds that we interpret as the Sp conversion at the Moho. Some stations located in sediments also display an earlier peak. No clear Sp conversion at the LAB can be identified in the overlay plots.

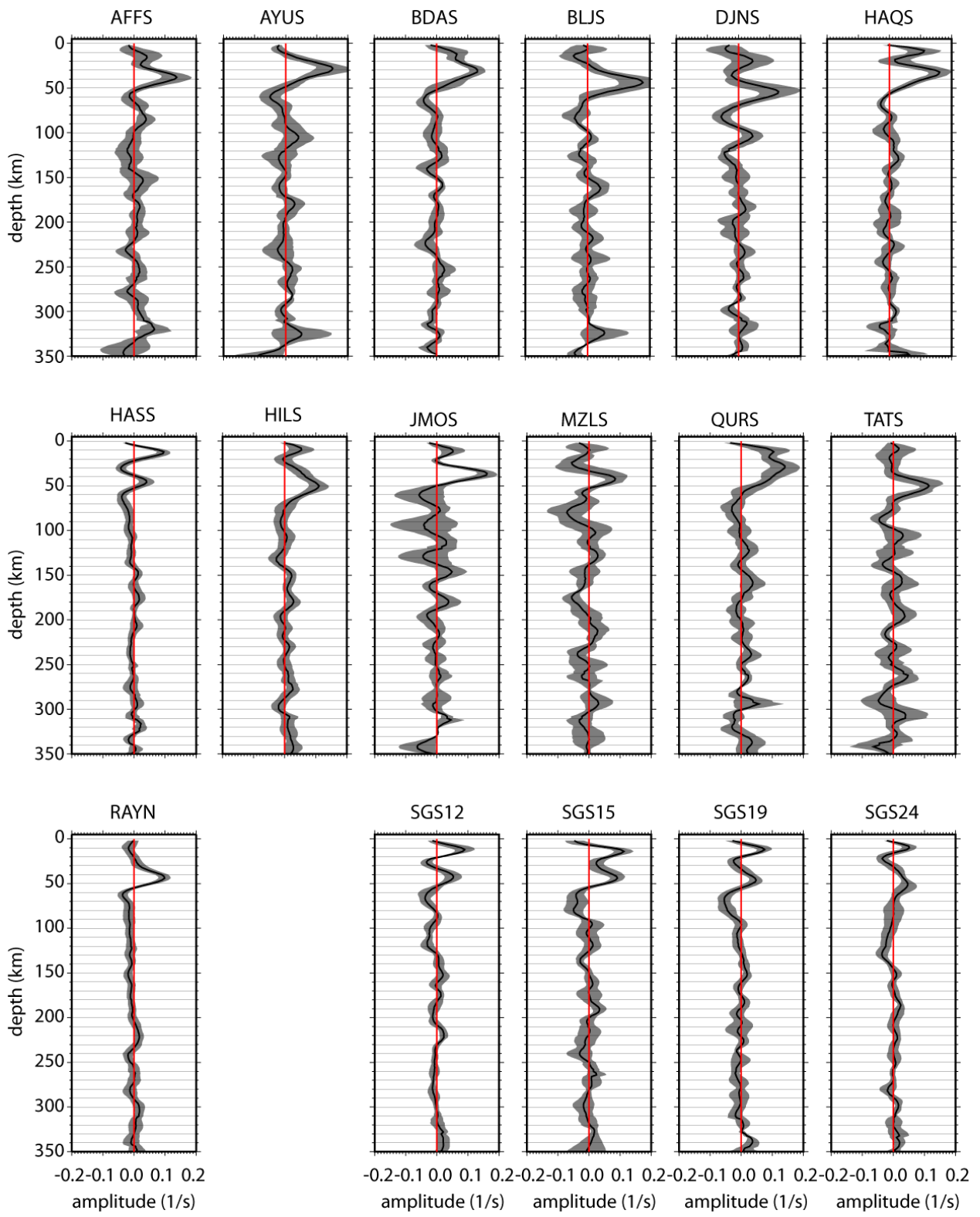


Figure 4.5 – Migrated SRF stacks for several stations in Saudi Arabia. The grey bands are bootstrapped 1s-confidence bounds. Note the clear Sp conversions at the Moho and the more subtle negative Sp amplitudes at lithospheric depths.

4.5 Incorporating high-frequency dispersion from ambient-noise cross-correlations

In this study, we used the ambient noise method to image the shear velocity in the crust and uppermost mantle beneath the Arabian Peninsula. We calculated the ambient noise correlation Green's functions for all available station pairs within the Saudi seismic networks, which provide hundreds of unique paths exclusively sampling the region. We measured group velocities in conjunction with the joint-inversion of receiver functions and dispersion velocities. Separately, we inverted the Green's function waveforms for the best 1D models along each path and created a 3D model based on those results. Greatest resolution is determined by station density and is greatest along the western part of the kingdom along the Red Sea. The raw data for this study consisted of continuous waveform data for the month of January 2010 from 33 stations in the Saudi national network and an additional 6 stations from stations outside the network, which were included to extend coverage (Figure 4.6). The Saudi network data were obtained from the Saudi Geological Survey (SGS) and King Abdulaziz Center for Science and Technology (KACST). External network data were obtained from the publicly available archive at the Incorporated Research Institutes for Seismology (IRIS/PASSCAL). The station names and location data are listed in the Appendix A.

Following the procedure outlined in Bensen et al. (2007) we cut the data into synchronous hour-long segments, instrument corrected the traces to displacement, removed the mean and the trend and applied a 1% taper. The data were then whitened to equalize the frequency content, and finally converted to single-bit waveforms to minimize the weight of large earthquakes on the correlations (Larose

et al., 2004). For each hour, every station was correlated with all the others creating an initial Green's function estimate. This results in a separate correlation waveform for each hour of each day for every pair of stations. By stacking all the hourly correlations, we recover the Green's function with the best signal to noise ratio (SNR). A complete 30 day record would provide us with 720 hours of data, however incomplete traces reduce this, somewhat. Most of the ambient noise Green's functions in this study contain more than 660 hours of continuous data with the maximum being 712 hours and the minimum including only 270 hours.

If the source of the coherent noise were uniformly distributed throughout the Earth, the Green's functions would be symmetric around zero time. Energy traveling from station A to station B would appear at positive time and is often referred to as "causal" energy. Energy traveling from station B to station A would appear at negative time and referred to as "a causal". Ambient noise is known to be inhomogeneously distributed and furthermore, seasonal in its occurrence, so the correlations will typically be dominant on either the causal or acausal side. Additionally the source of the ambient noise varies with frequency, so that the waveform will appear to be dominated by causal energy in some bands and by acausal energy in others. In this study, we take every correlation trace, reverse it around zero time and stack it with the unreversed original. This combines the "causal" ($t > 0$) and "acausal" ($t < 0$) portions of the empirical Green's function. This step results in Green's functions that look symmetric around zero and allows us to perform all of our measurements on the causal trace.

Excluding autocorrelations, we obtained Green's function estimates for 528 paths between stations within the Saudi network and 741 paths total. Separation between

stations ranged between 23 km and 3917 km. An example of the quality of the correlations is given in figure 4.7. We see very good quality signals at less than 700 km, but SNR decreases rapidly with both distance and frequency.

4.6 Group velocity measurements and Signal-to-Noise spectra

In conjunction with the joint inversion of P- and S- receiver functions and dispersion velocities, group velocity measurements were made for all (741) station-pairs and are contained in the Appendix A. 23 bands were selected such that the center frequencies were evenly sampled in log10 space and ranged from 0.02 to 4.10 Hz. These bands were defined such that

$$\text{low pass} = 10 (\log_{10}(\text{center freq}) - 0.1)$$

$$\text{high pass} = 10 (\log_{10}(\text{center freq}) + 0.1)$$

Group velocities were measured within a time window defined by

$$\text{start cut} = \text{distance} / 4.8$$

$$\text{end cut} = \text{distance} / 2.0$$

These were all measured on the vertical component correlations and should be regarded as Rayleigh wave group velocities.

The signal to noise ratio (SNR) for each trace was measured by calculating the time-domain RMS amplitude over a signal window and a noise window. The signal window was defined by the start and end cut above, with the exception that the duration of the time window was enforced to be at least 2/low pass. The noise window was defined to begin 60 seconds after the signal window and be 60 seconds long, likewise with the exception that its duration was forced to be at least 2/low pass.

As illustrated in the spectrogram (figure 4.8), SNR is a strong function of both distance and frequency. At less than 100 km, the month of data provides high quality signal in a broad band ranging from 0.03 - 1 Hz. The signal degrades rapidly with distance, such that by 500 km the high quality signal band falls between 0.03 - 0.25 Hz. Past 1200 km the usable band is below 0.1 Hz and often too noisy even for that. Adding more continuous data to the correlation stacks would significantly improve the quality of the Green's function estimates and the raw Green's functions are being delivered along with this report to allow other researchers to expand on the work, should additional data become available.

4.7 1D Model Inversions

We used the correlation Green's functions as data to invert for shear velocity using a partitioned waveform inversion scheme (Nolet, 1990). The task is to obtain the best 1D model along each path and then merge the paths together to create a 3D image. The optimization was defined to maximize the fit of a synthetic seismogram to the envelope of the Green's function (Figure 4.9). We used a very-fast simulated annealing technique (Sen and Stoffa, 1995) to search efficiently through model space. Synthetics were created using the reflectivity method (Fuchs and Muller, 1971; Randall, 1994) which allows rapid calculation of seismograms for 1D earth models. This allowed us to conduct several thousand iterations, obtaining a separate best fitting model for each of the 741 paths.

Because SNR is such a strong function of distance and frequency, we ran two separate inversion runs: One for data filtered over frequency band between 0.05-0.25 Hz to optimize the strong signal from the short-range data and the other for a

frequency band between 0.03-0.09 Hz to avoid the high noise content of the long-range correlations. All models for distances less than 500 km are the result of the 0.05-0.25 Hz run. All models for distances greater than 1100 km are the result of the 0.03-0.09 Hz run. Models for distances between 500-1100 km are the result of the better of the two runs and tie directly to the SNR measurements listed in the appendix A.

An example of the 1D model results is shown in figure 4.10. We observe large variability in the models crossing different paths sampling different tectonic regimes. All the best fitting 1D models are provided in a separate spreadsheet

[Saudi_ANC_1D_bestfit_model_results_ALL_DATA.xlsx](#).

which is described in the appendix A.

4.8 Localized 3D tomography

The best fitting 1D models were merged into a 3D model of the subsurface using a partitioned waveform inversion technique (Nolet, 1990). Given the SNR quality of the long range data, together with the differences in resolution due to station distribution, we focused on the most well resolved region, surrounding the densely instrumented western Kingdom. A grid restricted between 15° - 30° latitude and 34° - 44° with a node spacing of 0.2° . We also only used the paths for stations separated by less than 1150 km. Based on the data quality issues mentioned above, the result (figure 4.11) should be considered preliminary, and will be enhanced by the joint inversion model. However, it illustrates the large degree of lateral heterogeneity that can be resolved using seismic interferometry in a densely instrumented region.

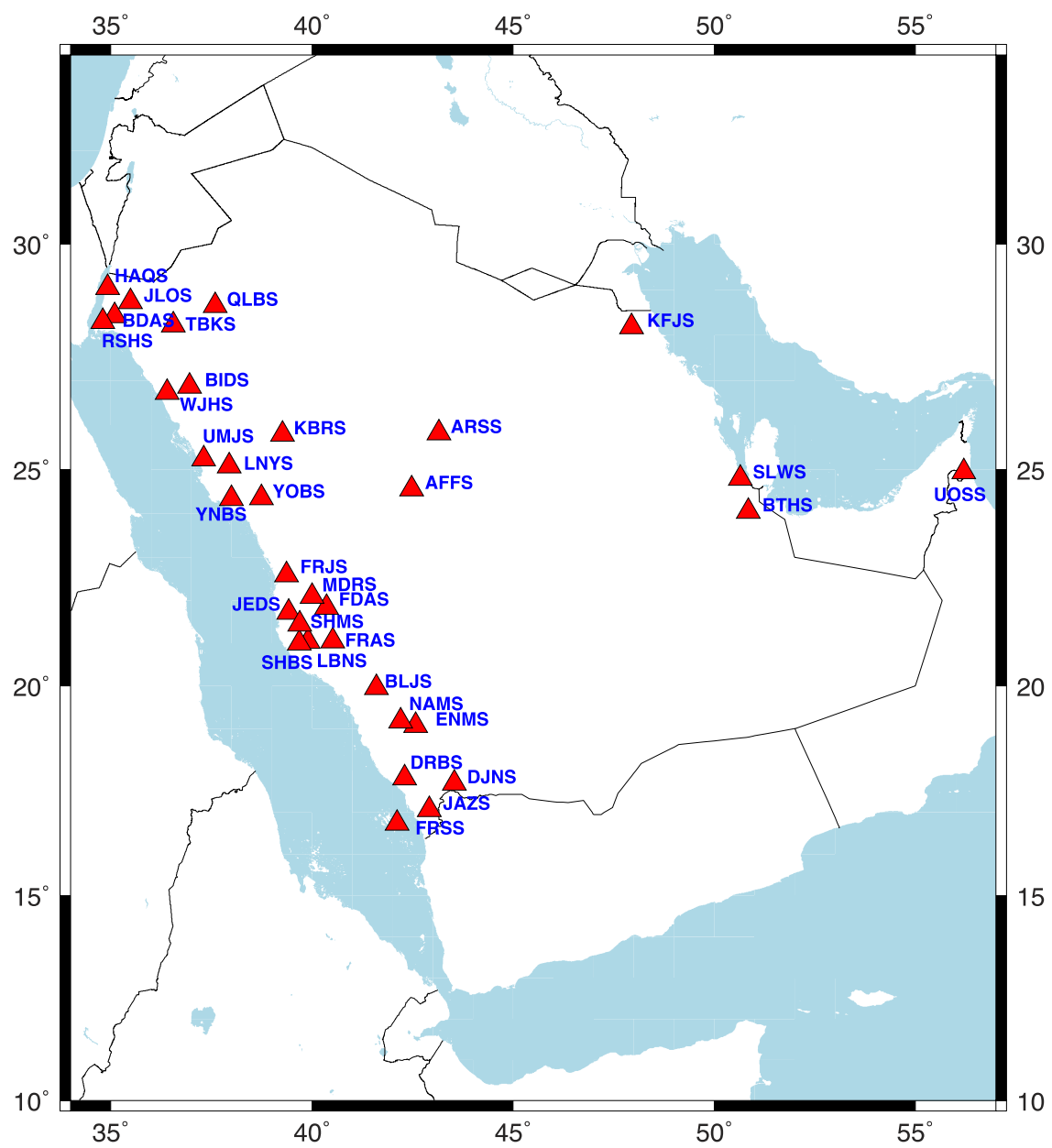


Figure 4.6. A station map showing the broadband seismic stations across the Peninsula used in the ambient noise correlation. Note: additional stations included to expand coverage, but off this map are FURI, ANTO, ABKT, GNI and KIV. (Data courtesy Saudi Geological Survey (SGS), King Abdulaziz Center for Science and Technology (KACST) and Incorporated Research Institutes for Seismology (IRIS/PASSCAL))

Ambient Noise Correlation Green's functions (0.05-0.25 Hz)

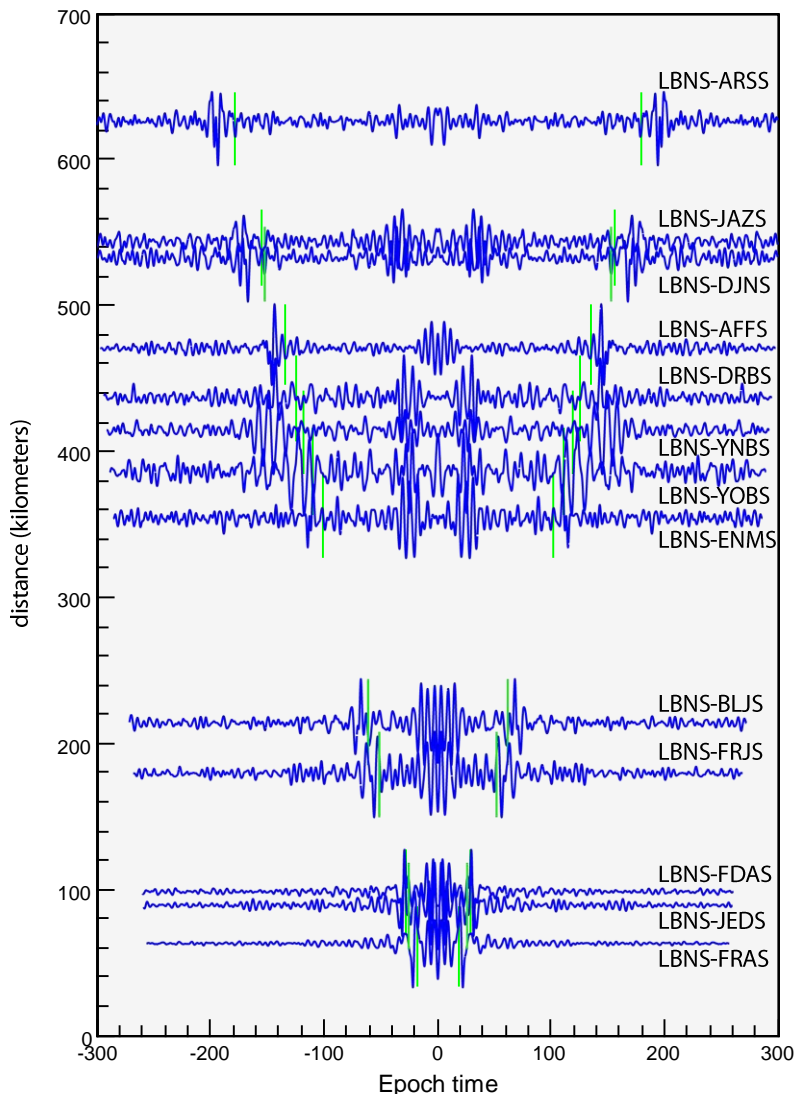


Figure 4.7. A profile of ambient noise correlation Green's functions computed using continuous data from the month of January 2010. The causal and a causal components of the waveforms have been stacked and filtered between 0.05 and 0.25 Hz. The 3.5 km/s group velocity is marked on each trace (green line). The pair of stations correlated in each case is labeled at right.

signal to noise spectrogram

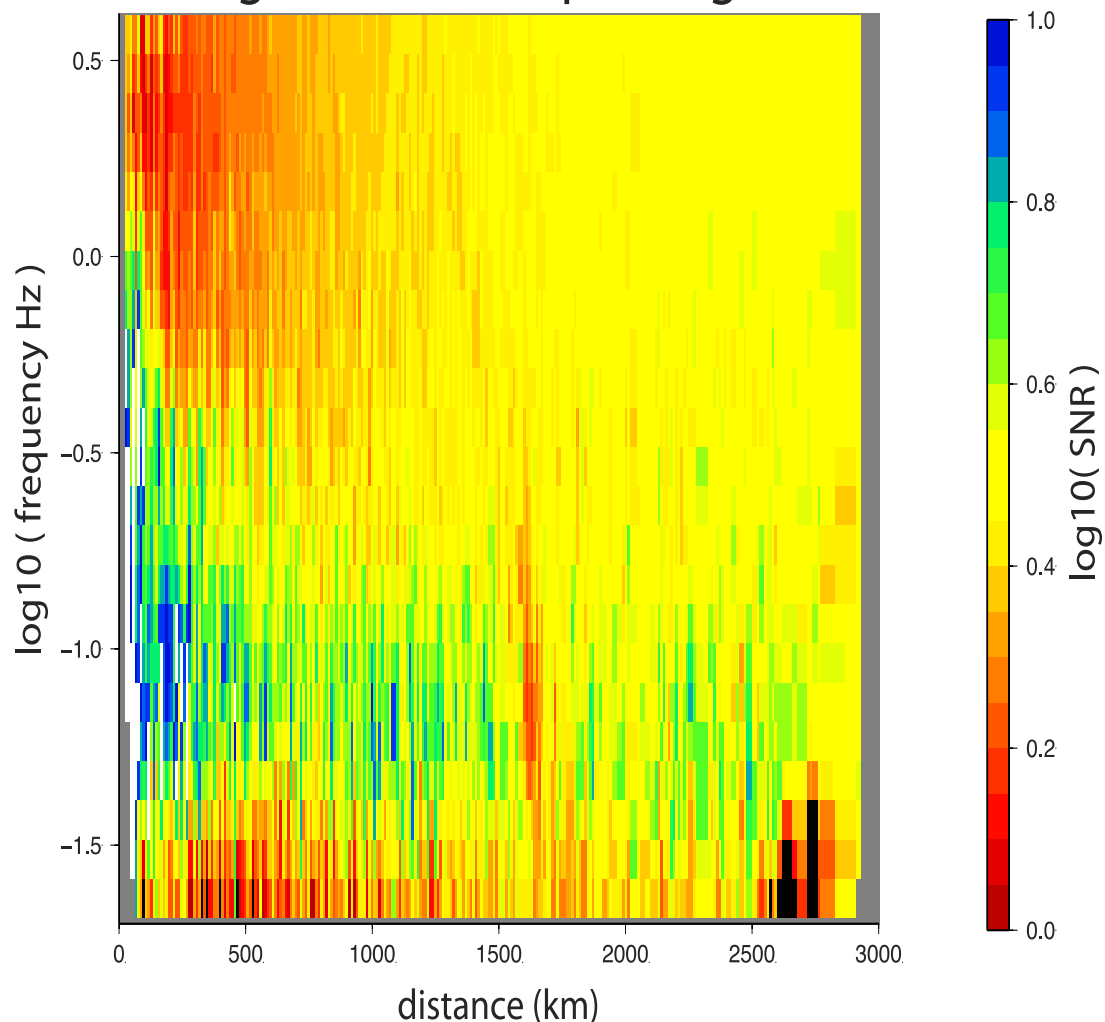


Figure 4.8. SNR for the correlation Green's functions is a strong function of both distance and frequency. At less than 100 km, the month of data acquired provided high quality signal in a broad band ranging from 0.03 - 1 Hz. The signal degrades rapidly with distance, such that by 500 km the high quality signal band falls between 0.03 - 0.25 Hz. Past 1200 km the usable band is below 0.1 Hz and often too noisy for valid measurements.

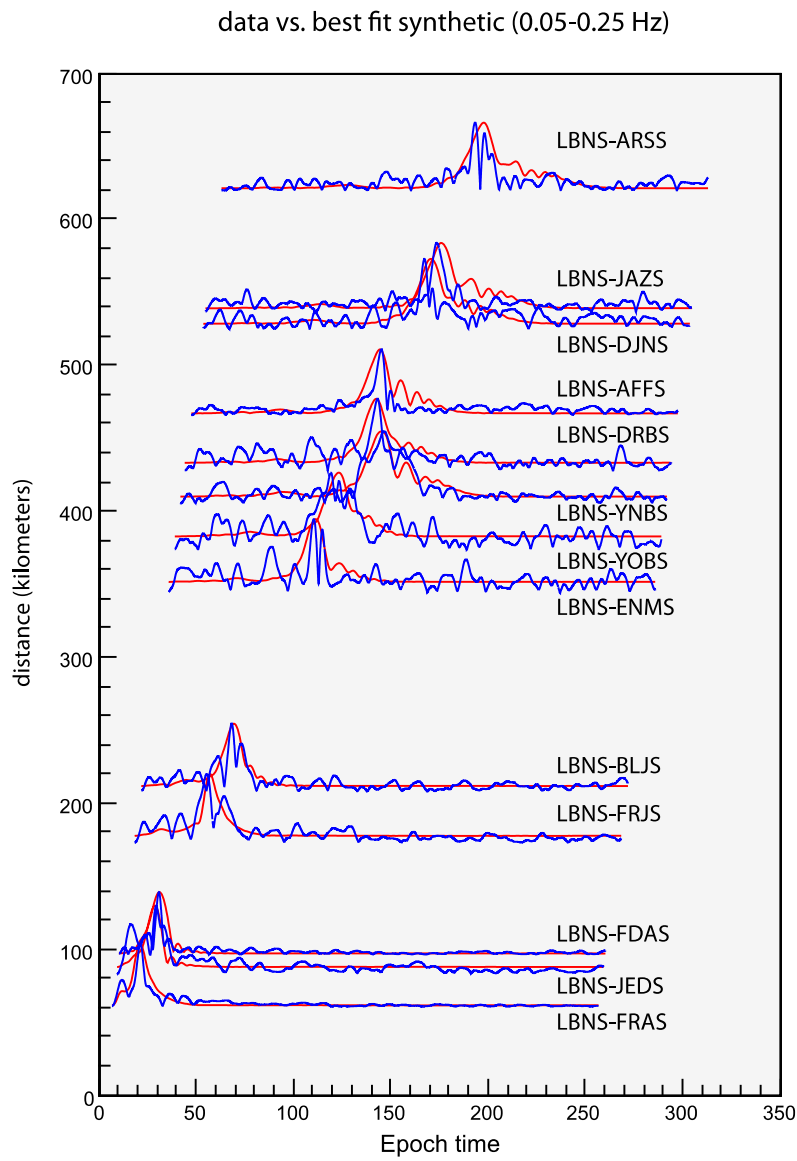


Figure 4.9. Envelopes of the noise correlation Green's functions (blue) compared with synthetics for the best fitting 1D models for each path (red).

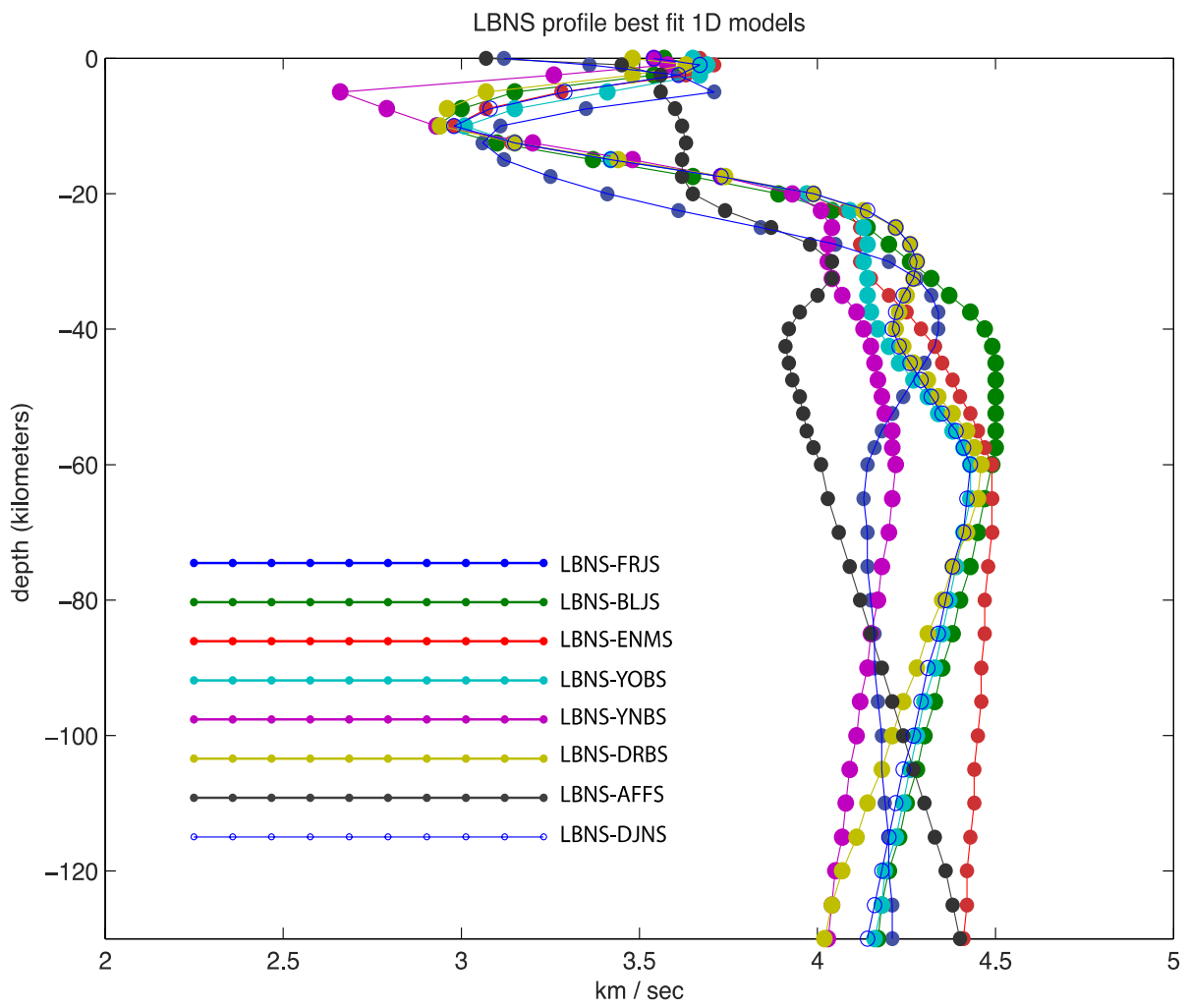


Figure 4.10. The best fitting 1D models for a subset of the paths shown in figure 3.5.

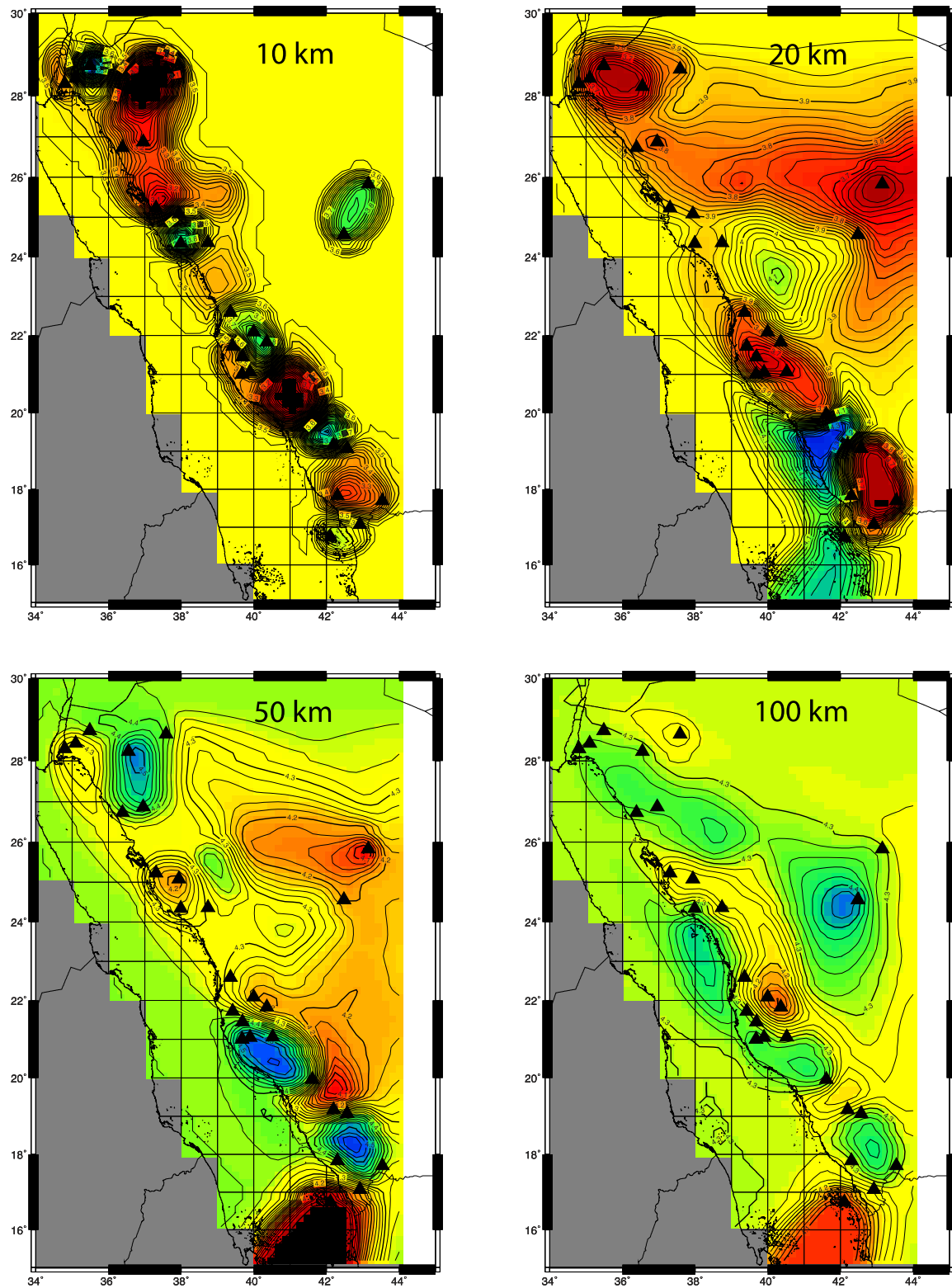


Figure 4.11 Slices through a localized 3D model at 10, 20, 50 and 100 km.

4.9 Developing Joint Inversion Models for the Arabian Shield.

We jointly inverted the PRFs and SRFs obtained in task 1 with dispersion velocities measured on the Green's functions obtained in task 2 and with fundamental-mode, Rayleigh-wave, group and phase velocities borrowed from the tomographic studies of Pasmanos (2005) and Ekström et al. (1997). Using the receiver functions and dispersion measurements, we produced joint inversion models for the broadband stations in Saudi Arabia.

Velocity models from the joint inversion of PRFs, SRFs, and dispersion velocities have been produced for 17 stations in Saudi Arabia, corresponding to stations for which stable SRF estimates could be obtained (Figure 4.12). As explained in our report of Task 1, stable SRF averages are harder to obtain than stable PRF averages due to the reduced epicentral distance range for teleseismic S-wave sources and also due to the fact that Sp conversions occur within the coda of the teleseismic P-wave. Previous to the inversion, PRFs and SRFs waveforms for each station were sorted by ray parameter and binned within ranges of 0.10 s/km and the receiver functions within each bin were averaged, provided that the bin included a minimum of 3 waveforms, to improve the signal-to-noise ratio. Binning around ray parameter values (or, equivalently, incidence angle) before averaging the PRFs and SRFs is critical to prevent incoherent overlap of P-to-S and S-to-P conversions, respectively, due to different phase move-outs.

Surface-wave dispersion velocities for the joint inversion were obtained from the independent surface-wave tomography study of Pasmanos (2005). The study measured quality fundamental-mode group velocities along 30,000 Rayleigh wave and 20,000 Love wave paths for periods between 7 and 100 s, and reported lateral

variation in group-velocity across Eurasia and North Africa. Although the results of the tomographic study were reported in $1^{\circ} \times 1^{\circ}$ cells, the checkerboard tests showed that the average resolution of the study is around $4^{\circ} \times 4^{\circ}$ (for 50 s period Rayleigh-waves). We identified the tomographic cell containing the selected stations in the Arabian Peninsula and extracted the corresponding dispersion curve, which was then regarded as the local dispersion estimate for that station. As the resolution of the Love waves is poorer than that of the Raleigh waves (due to fewer measurements and poorer signal-to-noise ratios), we only utilized the Rayleigh-wave dispersion curve.

For the inversions, we considered a starting model consisting of a 40 km-thick crust with a gradational increase between 6.0 and 7.0 km/s in P-wave velocity and a uniform crustal Vp/Vs ratio of 1.75, overlying a flattened PREM (Dziewonski and Anderson, 1980). We found a uniform Vp/Vs ratio justified for the Arabian crust, as values obtained from the hk-stacking analysis do not deviate significantly from this average, in general (see Table 2); for the lithospheric and sub-lithospheric mantle a PREM-like, depth-dependent Vp/Vs value was assumed. The model was parameterized down to \sim 500 km depth as a stack of thin layers with thicknesses of 1.0 km between 0 and 5 km depth, 2.5 km between 5 and 60 km depth, 5 km between 60 and 200 km depth, and 10 km below. We inverted for S-wave velocity structure down to \sim 250 km depth and constrained the structure below that depth to be PREM-like in order to realistically account for the partial sensitivity of the long-period surface-waves to deep upper mantle structure (Julià et al., 2003). Joint inversion models were obtained after 6 iterations, using an influence factor $p=0.5$ and a smoothing of $\sigma=0.2$. To equalize the datasets, values for the weights w_b and

w_s (eq. 4) were obtained by multiplying the number of data points with average data variances of $\sigma_b^2 = 5 \cdot 10^{-4} \text{ s}^{-2}$ and $\sigma_s^2 = 10^{-4} \text{ km}^2/\text{s}^2$ for the dispersion velocities and receiver functions, respectively.

A detailed joint inversion of PRFs, SRFs, and dispersion velocities is shown in Figure 4.12 for station AYUS, located near the Gulf of Aqaba. The velocity model consists of a ~ 28 km thick crust with crustal S-velocities well under 4.0 km/s that increase with depth (the low velocity zone in the uppermost crust is probably not well resolved due to the lack of short-period measurements in the dispersion velocity curve). The crust overlies a pretty thin (~ 15 km) and slow (~ 4.3 km/s) upper mantle lid which, in turn, overlies the top of a low-velocity zone with a minimum velocity around 4.0 km/s at ~ 60 km depth. The bottom of the low-velocity zone returns to PREM-like velocities at around 180 km depth. The predictions from this model display an excellent agreement with observed PRFs, SRFs and fundamental-mode, Rayleigh-wave, group-velocities.

A summary of all velocity models obtained at the seismic stations in Saudi Arabia is given in Figure 4.13. The figure displays the joint inversion models down to 350 km depth (note the bottom 100 km is constrained to be PREM-like) along with stacked PRF and SRF waveforms migrated to depth. In general, the Moho is consistently seen in both PRF and SRF waveforms and, not surprisingly, accurately located in the joint inversion models. The lithosphere-asthenosphere boundary (LAB) and the bottom of the low-velocity channel, on the other hand, correspond to smaller velocity contrasts in the velocity models and are therefore hard to see in PRFs. For these discontinuities, the information from the SRFs is critical and has helped

constrained lithospheric and sub-lithospheric structure accurately. Detailed fits to observed PRF waveforms, SRF waveforms and dispersion velocities, as predicted by the joint inversion models, can be found in Appendix A.

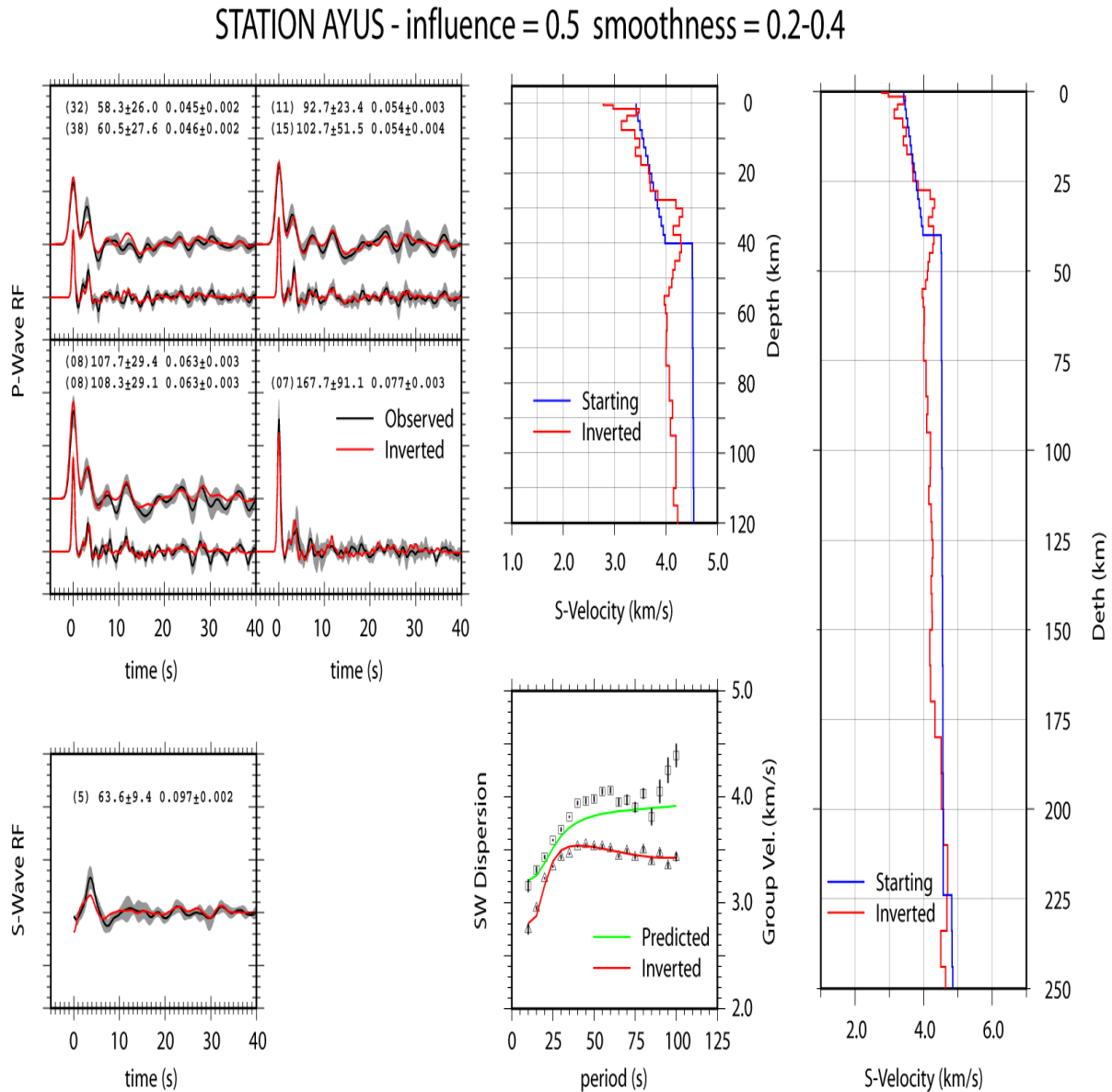
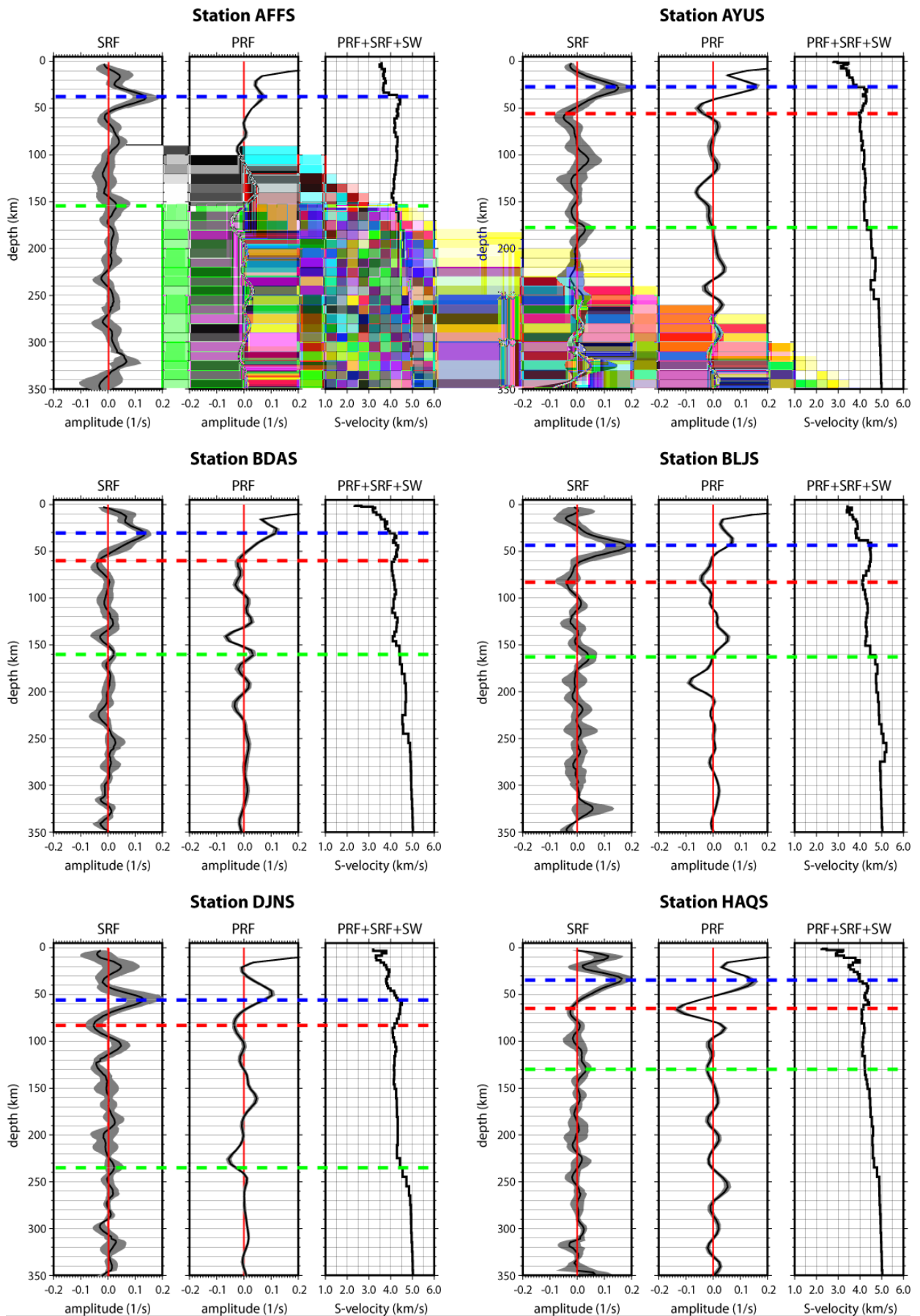
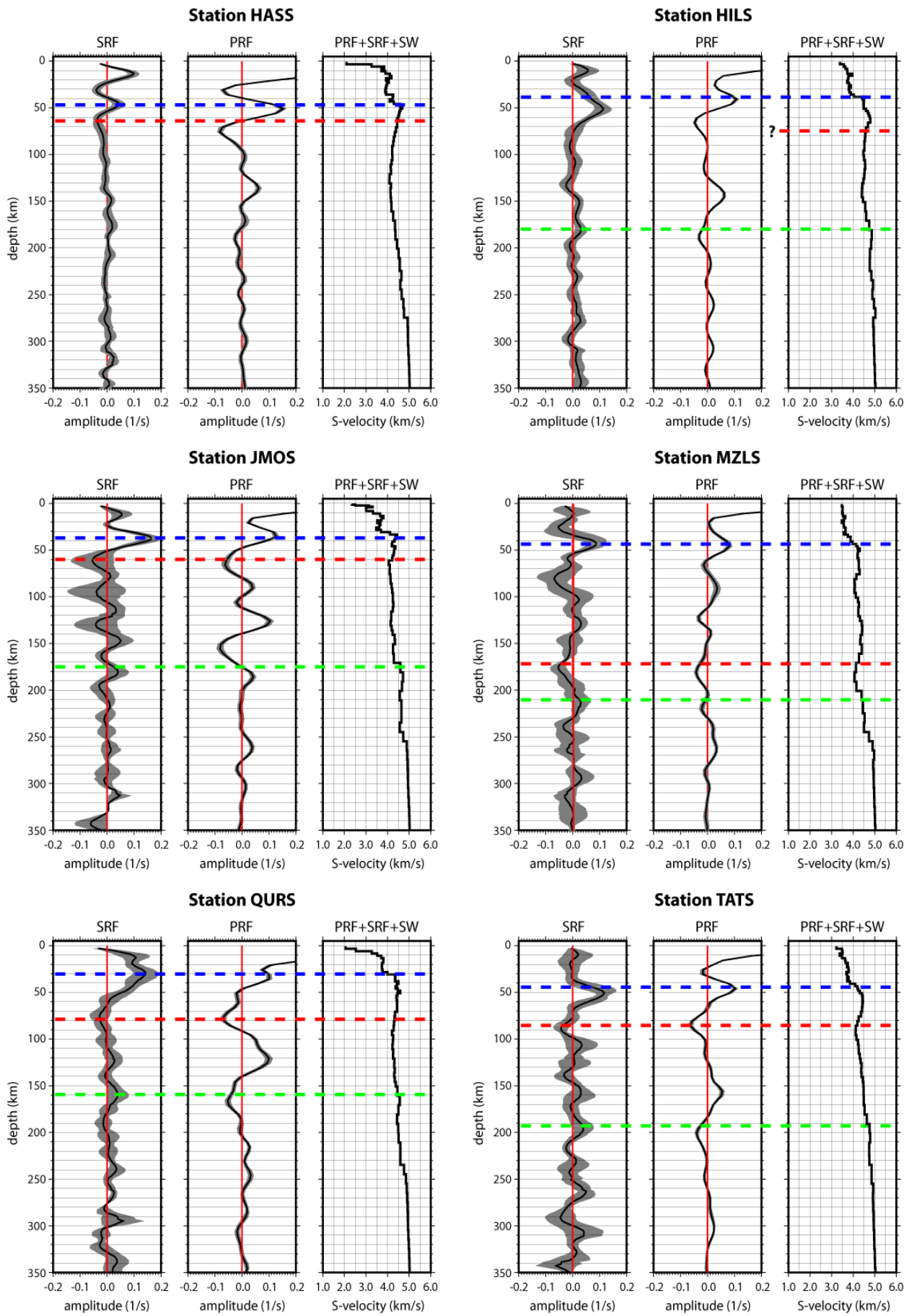


Figure 4.12 Joint inversion of PRFs, SRFs, and SW dispersion velocities at station AYUS. The left panels display observed (black) and predicted (red) receiver functions and the middle panel at the bottom displays observed (symbols) and predicted (lines) group velocities. Only fundamental-mode, Rayleigh waves were used during the inversion (red) but a prediction for the fundamental-mode, Love-wave, group velocity is shown (green). The inverted S-velocity model is shown to the right, with the crustal portion enlarged in the middle (top) panel.





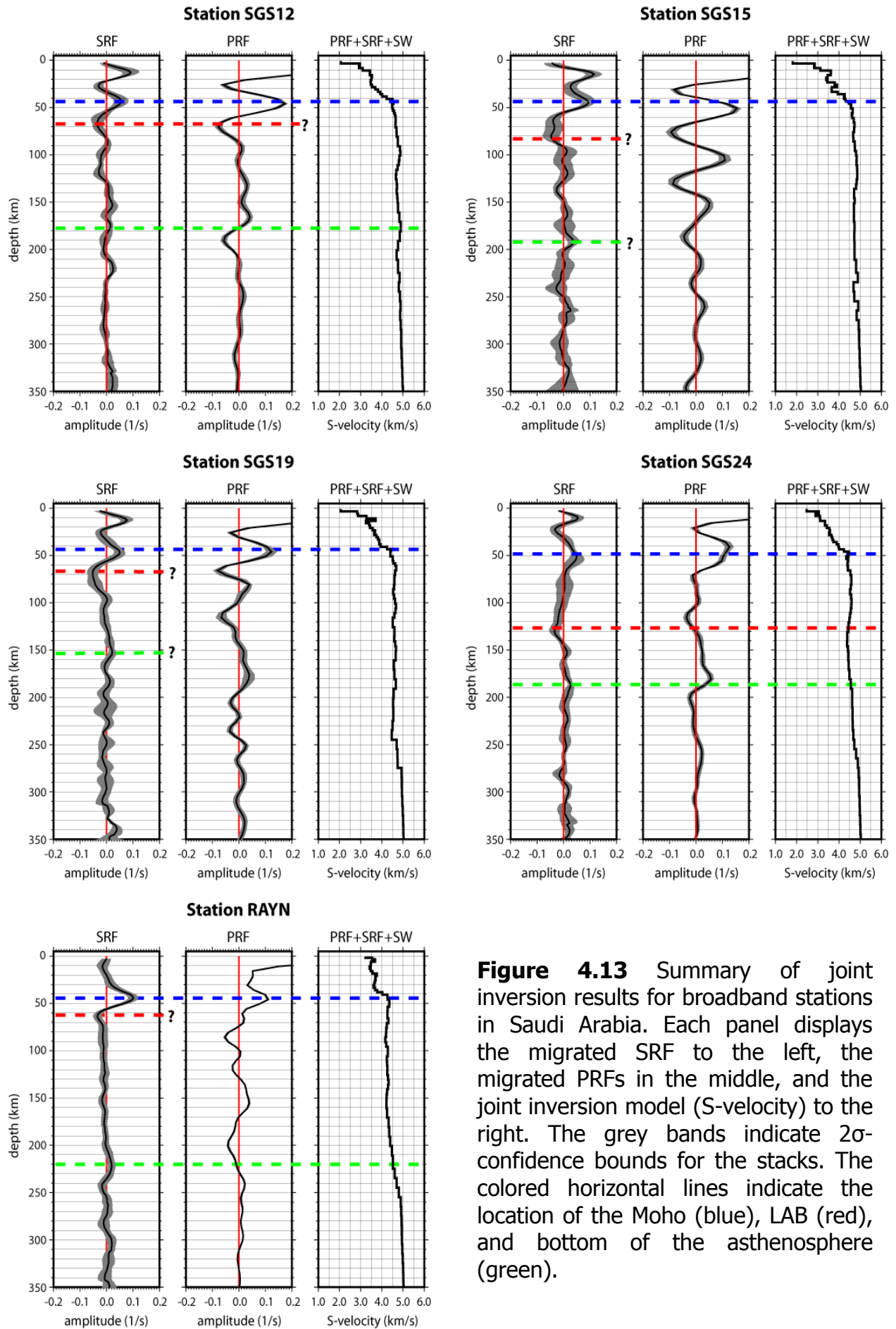


Figure 4.13 Summary of joint inversion results for broadband stations in Saudi Arabia. Each panel displays the migrated SRF to the left, the migrated PRFs in the middle, and the joint inversion model (S-velocity) to the right. The grey bands indicate 2σ -confidence bounds for the stacks. The colored horizontal lines indicate the location of the Moho (blue), LAB (red), and bottom of the asthenosphere (green).

CONCLUSIONS & RECOMMENDATIONS

We have developed lithospheric and sub-lithospheric velocity models for 17 broadband stations in Saudi Arabia from the joint inversion of PRFs, SRFs, and Rayleigh-wave group-velocities (fundamental mode). The velocity models successfully image detailed S-velocity variation with depth down to \sim 250 km depth, giving important constraints on key structural parameters such as crustal thickness, lithospheric thickness, lid velocity and (in some instances) thickness and minimum velocity of the low-velocity channel (asthenosphere). Models of crustal and uppermost mantle velocity for the Arabian Shield had been developed in the past from the joint inversion of PRFs and Rayleigh-wave group velocities (e.g. Julià et al., 2003); the novelty of the velocity models developed under this project has consisted in the addition of SRF data to extend the velocity models down to lithospheric and sub-lithospheric depths.

It is perhaps a bit disappointing that, out of 50 stations considered (Figure 1), joint inversion velocity models have been developed for just 17 of them. The reason for this low rate of success has to be sought in the computation of stable SRF waveforms. As explained during our report of Task 1, computation of stable SRF waveform averages requires a data set significantly larger than that required for computing stable PRF waveform averages; unfortunately, files containing about 5 years worth of data for KACST and SGS stations were corrupted and could not be used in our analysis. Nonetheless, velocity models from the joint inversion of PRFs and Rayleigh-wave group-velocities have been developed for the remaining 33 stations; if the missing data can be recovered, SRFs can be easily computed and

added to the joint inversion scheme to extend the velocity models down to lithospheric depths for those stations.

In summary, the 17 S-velocity models have been developed under this project from the joint inversion of PRFs, SRFs and surface-wave (ballistic) dispersion velocities. These models will help better constrain the deep crustal, lithospheric, and sub-lithospheric structure under Saudi Arabia and, in turn, help further our understanding of regional wave propagation in and tectonic evolution of the Arabian shield and platform.

RECOMMENDATIONS FOR FURTHER INVESTIGATIONS

In order to fully understand the detail geophysical, seismological and seismic hazard picture of the Arabian Peninsula, this study recommends an extensive research covering :

- A. An expensive but potentially insightful line of research is to carry out a detailed seismic deep refraction and gravity profiles in the Arabian Platform and along the coast of the Gulf of Aqabah to obtain a precise bulk composition of crustal layers and improve velocity model.
- B. Installation of strong motion accelerographs in various areas of the Arabian Shield to precisely estimate the attenuation characteristics of the region and to improve seismic hazard parameters.
- C. Assessment of seismic hazard in seismically active zones by constructing a probabilistic ground-shaking hazard map. This map will provide an estimate of the level of ground shaking at all sites expected from earthquake sources throughout the region (both local and regional). The map integrates the seismicity, attenuation and sit response factors.

D. A comprehensive study of the geotechnical engineering aspects should be done to account for local site effects and soil amplification.

E. A comprehensive study of seismogenic and faulting sources is needed for seismic zonation and microzonation of the Arabian Peninsula.

F. Geodetic measurements are recommended in order to identify and quantify very recent neotectonic activity and thus, provide prediction of specific future event and crustal deformation. Geodetic techniques range from ground technique using strain meters and laser-ranging devices to space technique using very-long-baseline radio interferometry (VLBI) and the global positioning system (GPS).

REFERENCES

- Al-Amri, A. M.(1998), The crustal structure of the western Arabian Platform from the spectral analysis of long-period P-wave amplitude ratios, *Tectonophysics*, 290, 271-283.
- Al-Amri, A. M.(1999). The crustal and upper-mantle structure of the interior Arabian platform, *Geophys. J. Int.*, 136, 421-430.
- Al-Damegh, K, E. Sandvol and M. Barazangi (2005). Crustal structure of the Arabian plate : New constraints from the analysis of teleseismic receiver functions, *Earth and Planetary Science Letter*, 231, 177-196.
- Al-Husseini M I (2000) Origin of the Arabian plate structures: Amar collision and Najd rift, *GeoArabia*, 5(4), 527-542
- Ammon, C.J., G.E. Randall, and G. Zandt (1990). On the non-uniqueness of receiver function inversions, *J. Geophys. Res.*, 95, 15303-15318.
- Ammon, C.J. (1991). The isolation of receiver effects from teleseismic P waveforms, *Bull. Seism. Soc. Am.*, 81, 2504-2510.
- Benoit, M., A. Nyblade, J. VanDecar, H. Gurrola (2003). Upper mantle P wave velocity structure and transition zone thickness beneath the Arabian Shield, *Geophys. Res. Lett.* 30, 1-4.
- Bensen, G.D., Ritzwoller, M.H., Barmin, M.P., Levshin, A.L., Lin, F., Moschetti, M.P., Shapiro, N.M. & Yang, Y(2007). Processing seismic ambient noise data to obtain reliable broad-band surface wave dispersion measurements, *Geophys. J. Int.*, 169, 1239–1260.
- Berteussen, K.A. (1977). Moho depth determinations based on spectral ratio analysis of NORSAR long-period P waves, *Phys. Earth Planet. Interiors*, 31, 313-326.
- Bostock, M.G. (1999). Seismic waves converted from velocity gradient anomalies in the Earth's upper mantle, *Geophys. J. Int.*, 138, 747-756.
- Camp, V. E., and M. J. Roobol (1992). Upwelling asthenosphere beneath western Arabia and its regional implications, *J. Geophys. Res.*, 97, 15255-15271.
- Campillo, M., and A. Paul (2003). Long-range correlations in the diffuse seismic coda: *Science* 229, 547–549.
- Cassidy, J. (1992). Numerical experiments in broadband receiver function analysis, *Bull. Seis. Soc. Am.*, 82, 1453-1474.

Crotwell, H.P., T.J. Owens, and J. Ritsema(1999). The TauP Toolkit: Flexible seismic travel-time and ray-path utilities, *Seism. Res. Lett.* 70, 154-160.

Debayle, E., J. Leveque, M. Cara, Seismic evidence for a deeply rooted low-velocity anomaly in the upper mantle beneath the northeastern Afro/Arabian continent (2001). *Earth Planet. Sci. Lett.* 193, 423-436.

Dugda, M.T., A.A. Nyblade, J. Julià (2007). Thin Lithosphere Beneath the Ethiopian Plateau Revealed by a Joint Inversion of Rayleigh Wave Group Velocities and Receiver Functions, *J. Geophys. Res.*, 112, B08308, doi:10.1029/2006JB004918.

Durrheim, R. and Mooney, W.D. (1991). Archean and Proterozoic crustal evolution: Evidence from crustal Seismology, *Geology*, 19, 606-609.

Dziewonski, A., and D. Anderson (1980). Preliminary reference earth model, *Phys. Earth Plant. Int.*, 25, 297-356.

Efron, B. and R. Tibshirani (1991). Statistical data analysis in the computer age. *Science* 253, 390-395.

Ekström, G., J. Tromp, and E. Larson (1997). Measurements and global models of surface wave propagation, *J. Geophys. Res.*, 102, 8137-8157.

Farra, V., and L. Vinnik (2000). Upper mantle stratification by P and S receiver functions, *Geophys. J. Int.*, 141, 699-712.

Fuchs, K. and G. Muller (1971). Computation of synthetic seismograms with the reflectivity method and comparison with observations, *Geophys. J. R. Astron. Soc.*, 23, 417-433.

Geissler, W.H., Sodoudi, F., Kind, R. (2010). Thickness of the central and eastern European lithosphere as seen by S receiver functions, *Geophys. J. Int.*, 181, 604-634.

Gettings, M., H. Blank, W. Mooney and J. Healey (1986). Crustal structure of southwestern Saudi Arabia, *J. Geophys. Res.*, 91, 6491-6512.

Hansen, S., A. Rodgers, S. Schwartz, and A. Al-Amri (2007). Imaging ruptured lithosphere beneath the Red Sea and Arabian Peninsula, *Earth Planet. Sci. Lett.*, 259, 256-265.

Hennino, R., N. Trégourès, N. M. Shapiro, L. Margerin, M. Campillo, B. A. van Tiggelen, and R. L. Weaver(2001). Observation of equipartition of seismic waves:

Physical Review Letters, 86, 3447–3450.

Julià, J. (2007), Constraining velocity and density contrasts across the crust-mantle boundary with receiver function amplitudes, *Geophys. J. Int.*, 171, 286-301.

Julià, J., C.J. Ammon, R.B. Herrmann, and A.M. Correig (2000), Joint inversion of receiver function and surface wave dispersion observations, *Geophys. J. Int.*, 143, 99-112.

Julià, J., C.J. Ammon, and R.B. Herrmann (2003). Lithospheric structure of the Arabian shield from the joint inversion of receiver functions and surface-wave group velocities, *Tectonophysics*, 371, 1-21.

Julià, J., C.J. Ammon, and A.A. Nyblade (2005). Evidence for mafic lower crust in Tanzania, East Africa, from joint inversion of receiver functions and Rayleigh wave dispersion velocities, *Geophys. J. Int.*, 162, 555-569.

Julià, J., M. Assumpção, and M.P. Rocha (2008). Deep crustal structure of the Paraná Basin from receiver functions and Rayleigh-wave dispersion: Evidence for a fragmented cratonic root, *J. Geophys. Res.*, 113, B08318, doi:10.1029/2007JB005374.

Julià, J., S. Jagadeesh, S.S. Rai, and T.J. Owens (2009). Deep crustal structure of the Indian shield from joint inversion of P wave receiver functions and Rayleigh wave group velocities: Implications for Precambrian crustal evolution, *J. Geophys. Res.*, 114, B10313, doi:10.1029/2007JB006261.

Karato, S.I. (2003). The Dynamic Structure of the Deep Earth. An Interdisciplinary Approach, Princeton University Press, 241 pp.

Kennett, B.L.N. (1983). *Seismic Wave Propagation in Stratified Media*, Cambridge University Press, 342 pp., New York, NY.

Kennett, B., E. Engdahl, and R. Buland (1994). Constraints on seismic velocities in the Earth from traveltimes, *Geophys. J. Int.*, 122, 108-124.

Keranen, K.M., S.L. Klemperer, J. Julià, J.F. Lawrence, and A.A. Nyblade (2009). Low lower crustal velocity across Ethiopia: Is the Main Ethiopian Rift a narrow rift in a hot craton?, *Geochem. Geophys. Geosyst.*, 10, Q0AB01, doi:10.1029//2008GC002293.

Kgaswane, E., A.A. Nyblade , J. Julià , P. Dirks, R.J. Durrheim , and M. Pasyanos (2009). Shear wave velocity structure of the lower crust in southern Africa:

Evidence for compositional heterogeneity within Archaean and Proterozoic terrains, *J. Geophys. Res.*, 114, B12304, doi:10.1029/2008JB00621.

Kosarev, G., R. Kind, S. Sobolev, X. Yuan, W. Hanka, and S. Oreshin (1999). Seismic evidence for adetached Indian lithosphere mantle beneath Tibet, *Science*, 283, 1306-1309.

Kumar, P., R. Kind, W. Hanka, K. Wylegalla, C. Reigber, X. Yuan, I. Woelbern, P. Schwintzer, K. Fleming, T. Dahl-Jensen, T. Larsen, J. Schweitzer, K. Priestley, O. Gudmundsson, andD. Wolf (2005). The lithosphere-asthenosphere boundary in the North-West Atlantic region,*Earth Planet. Sci. Lett.*, 236, 249-257, 2005.

Kumar, P., X. Yuan, M. Ravi Kumar, R. Kind, X. Li, and R. Chadha (2007). The rapid drift of the Indian tectonic plate, *Nature*, 449, 894-897.

Langston, C.A. (1977). The effect of planar dipping structure on source and receiver responses forconstant ray parameter, *Bull. Seis. Soc. Am.*, 67, 1029-1050.

Langston, C.A. (1979). Structure under Mount Rainier, Washington, inferred from teleseismic body waves, *J. Geophys. Res.*, 84, 4749-4762.

Larose, E., A. Derode, M. Campillo, and M. Fink (2004). Imaging from one-bit correlations of wideband diffuse wavefields: *Journal of Applied Physics*, 95, 8393–8399.

Levin, V., and J. Park (1997). P-SH conversions in a flat-layered medium with anisotropy of arbitrary orientation, *Geophys. J. Int.*, 131, 253-266, 1997.

Li, X., R. Kind, X. Yuan, I. Wölbern, and W. Hanka (2004). Rejuvenation of the lithosphere by theHawaiian plume, *Nature*, 427, 827-829, 2004.

Lin, F., Moschetti, M.P. & Ritzwoller, M.H.(2008). Surface wave tomography of the western United States from ambient seismic noise: Rayleigh and Love wave phase velocity maps, *Geophys. J. Int.*

Ligorría, J.P., C.J. Ammon (1999). Poisson's ratio variations of the crust beneath North America, *Seism. Res. Lett.*, 70, 274.

Looseveld R J H, Bell A, Terken J J M (1996) The tectonic evolution of interior Oman, *GeoArabia*, 1 (1), 28-51

Malcolm,A. E., J. A. Scales, and B. A. van der (2004). Tiggelen, Retrieving the Green function from diffuse, equipartitioned waves: *Physical Review E*, 70.

- Matzel, E. (2008). Attenuation tomography using ambient noise correlation, *Seismological Research Letters*, 79 (2), 358.
- Mellors, R., Vernon, F., Camp, V., Al-Amri, A.M and Gharib, A. (1999). Regional waveform propagation in the Saudi Arabian Peninsula and evidence for a hot upper mantle under western Arabia. *J. Geophys. Res.*, 104, 20,221–20,235
- Mooney, M. Gettings, H. Blank, J. Healy, Saudi Arabian seismic refraction profile: A travelttime interpretation of crustal and upper mantle structure (1985). *Tectonophysics* 111, 173-246.
- Moschetti, M.P., M. H. Ritzwoller, and N. M. Shapiro (2007). Surface wave tomography of the western United States from ambient seismic noise: Rayleigh wave group velocity maps, *Geochem., Geophys., Geosys.*, 8, Q08010.
- Nolet, G. (1990). Partitioned waveform inversion and two-dimensional structure under the network of autonomously recording seismographs, *J. Geophys. Res.*, 95(B6), 8499–8512.
- Owens, T., G. Zandt, and S. Taylor (1984). Seismic evidence for an ancient rift beneath the Cumberland Plateau, Tennessee: A detailed analysis of broadband teleseismic P waveforms, *J. Geophys. Res.*, 89, 7783-7795.
- Pasyanos, M.E. (2005). A variable resolution surface wave dispersion study of Eurasia, North Africa, and surrounding regions, *J. Geophys. Res.*, 110, doi: 10.1029/2005JB003749.
- Pasyanos, M.E., W.R. Walter, and E.M. Matzel (2009b). A simultaneous multi-phase approach to determine P-wave and S-wave attenuation of the crust and upper mantle, *Bull. Seism. Soc. Amer.*, 99-6, DOI: 10.1785/0120090061.
- Powers R W, Ramirez L F, Redmond C D, Elberg E L (1966) Geology of the Arabian Peninsula, Sedimentary geology of Saudi Arabia: U. S. Geological Survey professional paper 560-D D1-D147
- Prieto, G. A., and G. C. Beroza (2008). Earthquake ground motion prediction using the ambient seismic field, *Geophysical Research Letters*, 35, L14304.
- Randall, G. E. (1994). Efficient calculation of complete differential seismograms for laterally homogeneous earth models, *Geophys. J. Int.*, 118, 245-254.
- Richards, P.G. (1972). Seismic waves reflected from velocity gradient anomalies within the Earth's upper mantle, *J. Geophys.*, 38, 517-527.
- Rodgers, A., Walter, W., Mellors, R., Al-Amri, A. and Y. Zhang (1999). Lithospheric structure of the Arabian Shield and Platform from complete regional waveform modeling and surface wave group velocities, *Geophys. J. Int.*, 138, 871-878.

- Rychert, C.A., K.M. Fischer, and S. Rondenay (2005). A sharp lithosphere-asthenosphere boundary imaged beneath eastern North America, *Nature*, 436, 542-545.
- Rychert, C.A., S. Rondenay, and K.M. Fisher (2007). P-to-S and S-to-P imaging of a sharp lithosphere-asthenosphere boundary beneath eastern North America, *J. Geophys. Res.*, 112, B08314, doi:10.1029/2006JB004619.
- Rychert, C.A, and P.M. Shearer (2009). A global view of the lithosphere-asthenosphere boundary, *Science*, 324, 495-498.
- Sandvol, E., D. Seber, A. Calvert and M. Barazangi (1998). Grid search modeling of receiver functions: Implications for crustal structure in the Middle East and North Africa, *J. Geophys. Res.*, 103, 26,899-26,917.
- Sen, M. and Stoffa, P. L.(1995). Global optimization methods in geophysical inversion, Elsevier.
- Shapiro, N.M, M. Campillo, L. Stehly, and M.H. Ritzwoller (2005). High-Resolution surface wave tomography from ambient seismic noise, *Science*, 307, 1615-1618.
- Snieder, R., and E. Safak (2006). Extracting the building response using seismic interferometry: Theory and application to the Millikan Library in Pasadena, California, *Bull. Seismol. Soc. Am.*, 96, 586– 598.
- Sodoudi, F. (2005). Lithospheric structure of the Aegean obtained from P and S receiver functions, PhD Thesis, Freie Universität Berlin.
- Stoeser, D., and V. Camp (1985). Pan-African microplate accretion of the Arabian Shield, *Geological Society of America Bulletin*, 96, 817-826.
- Takeuchi, H., and M. Saito (1972). Seismic surface waves, in *Methods of Computational Physics*, pp. 217-295, eds. Bolt, B.A., Academic Press, New York.
- Tkalcic, H., Pasmanos, M., Rodgers, A., Gok, R., Walter, W., and Al-Amri, A. (2006). A multi-step approach in joint modeling of surface wave dispersion and teleseismic receiver functions: Implications for lithospheric structure of the Arabian Peninsula. *J. Geophys. Res.*, 111, doi : 10.1029/2005JB 004130.
- Vernon, F. and J. Berger, Broadband seismic characterization of the Arabian Shield(1997). Final Scientific Technical Report, Department of Energy Contract No. F 19628-95-K-0015, 36 pp.

- Wapenaar, K.(2004). Retrieving the elastodynamic Green's function of an arbitrary inhomogeneous medium by cross correlation: *Physical Review Letters*, 93, 254301.
- Weaver, R. L., and O. I. Lobkis, (2001). Ultrasonics without a source: Thermal fluctuation correlations at MHz frequencies: *Physical Review Letters*, 87, 134301.
- Wilson, D., D. Angus, J. Ni, and S. Grand (2006). Constraints on the interpretation of S-to-P receiver functions, *Geophys. J. Int.*, 165, 969 –980.
- Wittlinger, G., and V. Farra (2007). Converted waves reveal a thick and layered tectosphere beneath the Kalahari super-craton, *Earth Planet. Sci. Lett.*, 254, 404-415.
- Yuan, X., et al. (2000). New constraints on subduction and collision processes in the Central Andes from P-to-S converted seismic phases, *Nature*, 408, 958-961.
- Zandt, G., S.G. Myers, and T.C. Wallace (1995). Crust and mantle structure across the Basin and Range-Colorado Plateau boundary at 37°N latitude and implications for Cenozoic extensional mechanism, *J. Geophys. Res.*, 100, 10529-10548.
- Zhu, H., and H. Kanamori (2000). Moho depth variation in southern California from teleseismic receiver functions, *J. Geophys. Res.*, 105, 2969-2980.

RESPONSE TO REVIEWER'S COMMENTS ON THE FINAL

REPORT OF AR - 30 - 36

**الردود على ملئيات المحكمين بخصوص التقرير النهائي للبحث
رقم أت - 36 - 30 - 36**

المحكم الاول Reviewer # 1

1. The title is mentioning the term of new technology will be used in this project and actually it is not new technology. It was used by many researchers in the world.

We respectfully disagree with this statement. Joint inversion methodologies have been published for either PRFs and dispersion [Julia et al., 2000], or PRFs and SRFs [Kiselev et al., 2008], and been applied in different parts of the world by a number of authors. However, to date, we are not aware of any joint inversion that includes PRFs, SRFs, and dispersion velocities altogether into a single joint inversion scheme.

2. Arabic and English summaries are not similar and the English one is more loose than the Arabic one.

Both Arabic and English summaries are improved and identical

3. Literature review and methodology are sufficient.

OK.

4. Objectives of this project are achieved but in general sense without a detailed results.

We concur with the reviewer that results are not as detailed as expected. As explained in the final report, some data files were corrupted during the archiving process, which made it impossible to obtain stable SRF estimates for all the stations. Lithospheric structure strongly depends on SRFs so, regrettfully, we were not able to produce detailed lithospheric structure for a significant number of seismic stations.

5. Data that were used in this project are not enough to fulfill the outmost goal

As explained above, that was due to corruption of data files during the archiving process.

6. Most of the results are general and are known based on the plate tectonics and seismicity sciences but it is ok to be obtained in this region and to be compared to other areas.

OK.

7. The work in this research seems to be built on the research done by the following people : Dr. Julia which is one of the consultants in this project, Dr. Ligorria, and Dr. Pasyanos, in addition to Dr. Al-Amri.

Dr. Ligorria did not participate in the project. The reviewer probably

refers to Dr. Matzel (LLNL), who produced the results on ambient noise tomography.

8. Most of the recommendations are detailed work which not supporting the regional scale used in this study.

Not sure what the reviewer means with this statement.

9. There are six references were mentioned in the text without putting them in the references list. Also there are some other listed references were not mentioned in the text.

Checked and corrected

10. Work done in this project does not reflect the budget used.

In the original research proposal , the reviewers considered the assigned budget is reasonable.

11. This research project will help in understanding the lithospheric structure in regional sense and not in detailed as was mentioned.

We agree. Once again, the lack of detail was due to insufficient data for SRF computation.

Reviewer # 2 المُحَكِّمُ الثَّالِثُ

1. The deduced lithospheric model, fig. (3-6), page 45 is represented by the crust and only one very thick layer. Is this justified?

What is shown in figure 3.6 (page 45) is just a numerical, noise-free example to emphasize that SRF data is critical for constraining the velocity decrease at the base of the lithosphere (placed at 140 km depth in the example). Certainly, true lithospheric structure can get more complicated than that, but for the purpose of illustrating data sensitivity to earth structure we think it is enough.

2. Results of table (2) are more understood by either a cross-section or an isopach map.

A graphical representation of the results listed in table 2 is given in figure 4.3 (page 57) of the final report. We opted for showing the point measurements directly rather than producing an interpolated map of isopach lines, as suggested by the reviewer, because data points are unevenly spaced throughout the study area. Station density in the Gulf of Aqaba, for instance, is much higher than in the platform area, and might lead to artifacts in the interpolated areas.

3. The Vp/Vs values of table (2) show a relatively large range of variation (1.63-1.81). Does this variation show any spatial variation? Furthermore these variations require further discussion and interpretation.

Vp/Vs ratio is mostly sensitive to silica content [e.g. Christensen, 1996] and, especially, fluids in the crust. Receiver function studies in neovolcanic areas, for instance, have revealed Vp/Vs ratios as large as 1.89 [e.g. Julià et al., 2005]. Some of the Vp/Vs ratios reported in Table 2 are indeed very large. However, a close inspection of Table 2 reveals that most of those large values have large confidence bounds (i.e. SGS24 – 1.81 ± 0.08 ; YNBS – 1.93 ± 0.05) which prevents a reliable interpretation in terms of composition and/or partial melt. The remaining values do not show a clear pattern and/or correlation with either tectonic terrains or Cenozoic volcanism (harrats) in the shield. Expected variations in Vp/Vs ratio from those geological features are probably within confidence bounds of the measured Vp/Vs ratios.

4. The deduced crustal thickness for the area east of the Gulf of Aqaba, fig. (4-3), p. 57, show variations in the range 28 km – 39.3 km, but the crust appears to be thinner further north and east? This does not agree with previous results. This matter requires further clarification and discussion.

Indeed, the crustal thickness reported for station SGS25 ($H=39.3 \pm 1.6$ km, $Vp/Vs = 1.75 \pm 0.05$), located in the southernmost tip in the region east of the Gulf of Aqaba, is abnormally large.

We checked with the velocity-depth profile from the joint inversion (see figure attached) and noticed that there is a large velocity contrast at 27.5 km depth, which would be more consistent with crustal thicknesses generally reported for the area.

Interestingly, the velocity-depth profile also displays a low-velocity zone

(LVZ) at 32.5-37.5 km depth. The bottom of this LVZ is more consistent with the crustal thickness result shown in figure 4.3 (obtained from hk-stacking analysis). This, together with the large V_p/V_s ratio for this station, would suggest this LVZ corresponds to partially molten material, perhaps related to the opening of the Red Sea.

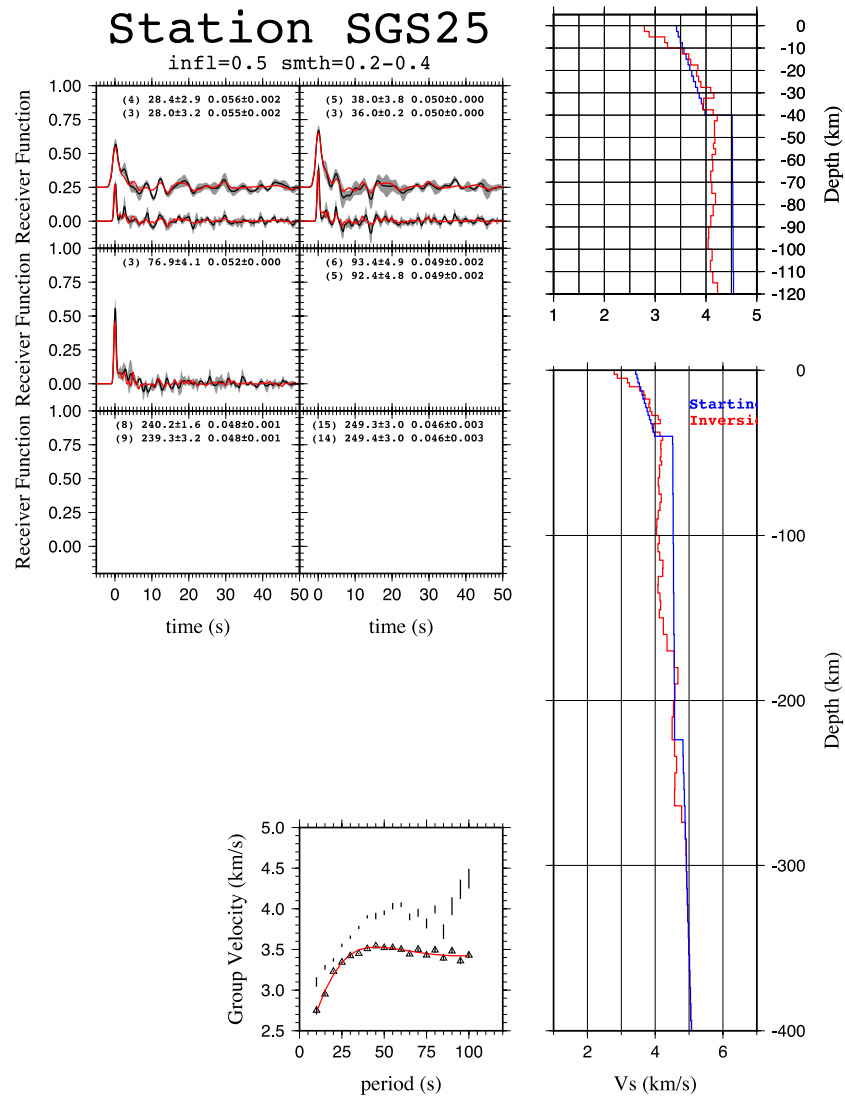
In any case, the velocity-depth profile for SGS25 demonstrates the 1D structure under this station is complex. Apparently, the hk-stacking result (Table 2, Fig. 4.3) refers to the base of the LVZ rather than the base of the crust.

5. The investigator claims that his crustal results do not differ from the previously deduced results. What is the point then of using all these five rather complicated techniques in such studies. One would expect some improvements on previous results !!!

Crustal S-velocity structure for the Arabian shield had been reported from the joint inversion of PRFs and dispersion velocities in Julià et al.[2003]. The results shown in the final report for this project include a significantly larger number of stations in the shield, as well as stations in the Arabian platform and Gulf of Aqaba. We are not sure what line/page of the report the reviewer is referring to, but the comparison most likely refers to the common stations in both studies. We were just trying to emphasize that, where there is overlap of data, both studies are consistent.

In any case, the main goal of the project was to improve on lithospheric mantle structure through the addition of SRF data to the joint inversion, rather than crustal structure. The results on lithospheric mantle

structure are summarized in figure 4.13 of the final report, and those represent a dramatic improvement with respect to previously published results.



GLOSSARY

المصطلحات اللاتينية وترجمتها الى العربية

Arabian Plate	الصفيحة العربية
Arabian Platform	الرصيف العربي
Arabian Shield	الدرع العربي
Asthenosphere	الغلاف الوهن
Azimuth	الإتجاه الزاوي
Broadband Stations	محطات واسعة المدى
Correlation Coefficient	معامل المضاهاه
Crustal Structure	التركيب الفشري
Crustal Thickness	السمك الفشري
Harrat Lunayyir	حرّة لونبیر
Delay Time	زمن التأخير
Epicenter	المركز السطحي للزلزال
Focal Mechanism Solutions	حلول ميكانيكية البؤرة
Fast Polarization	الاستقطاب السريع
Focal Depth	العمق البؤري
Group Velocities	السرعة الجماعية
International Association of Seismology & Physics of the Earth (Iasp91)	نموذج حساب معدل السرعة
Frequency	التردد
Aeromagnetics	المغناطيسيّة الجوية
Magma	صهارة
Lithosphere	الغلاف الصخري
Chronology	العمر الجيولوجي
Broadband seismic station	محطة رصد ذات فتره دوريه واسعة المدى
Longitude (E)	خط الطول
Lower Crust	القشره السفلية
Magnitude	القدر الزلزالى
Mantle	الوشاح (لحاء)

Miocene	فترة الميوسين
Moho Discontinuity	إنقطاع موهو
Monthly Listing	النشرةزلاليه الشهريه
Spreading Centers	مراكز التمدد
Tertiary	العصر الثلاثي
Origin Time	زمن حدوث الزلزال عند بؤره
Preliminary Determination of Epicenters (PDE)	التحديد المبدئي لمراكز الزلزال
Plate Tectonics	حركة الصفائح
Polar Projection	إسقاطقطبي
Primary Wave Velocity (Vp)	سرعة الموجات الطوليه
Quaternary	العصر الرابع
Receiver Function	دالة المستقبل
Response Curve	منحنى الاستجابة
Review Events Bulletin (REB)	نشرة الأحداث المراجعه
Rock Density	الكتافه الصخريه
SANDSN	الشبكة السعودية الوطنيه الرقمية للزلزال
Seismic Analysis Code (SAC)	كود التحليلزلالي
Seismic Attenuation	التعتيمزلالي
Seismic Hazards	خطر زلالي
Seismic Noise	الضوضاء السيسزميه
Seismic Tomography	زلالية ثلاثة الأبعاد
Seismic Waves	الموجاتزلاليه
Seismogram	سجل زلالي
Shear Wave Velocity (Vs)	سرعة موجات القص
Shear Wave Splitting	فصل موجات القص
Spectral Amplitude	السعه الطيفيه
Spectral Analysis	التحليل الطيفي
Surface Wave dispersion	تشتت الموجة السطحي
Surficial Sediments	رواسب سطحية
Synthetic Waveform	الشكل الموجي المركب
Take-off Angle	زاوية خروج الشعاع عند بؤرة الزلزال
Teleseismic Earthquakes	الزلزال البعيد
Tertiary	العصر الثالث

Theoretical Spectral Ratios	النسب الطيفية النظرية
Thickness	السمك
Transition Zone	منطقة إنتقالية
Travel Times	أزمنة المسار
Upper Crust	القشرة العلوية
Wave Propagation	الانتشار الموجي
Waveform Modeling	نمذجة الشكل الموجي

Appendix A

Station List

The raw data for this study consisted of continuous waveform data for the month of January 2010 from 33 stations in the Saudi national network and 6 stations from networks surrounding Saudi Arabia, which were included to extend coverage. The Saudi network data were obtained from the Saudi Geological Survey (SGS) and King Abdulaziz Center for Science and Technology (KACST). External network data were obtained from the publicly available archive at the Incorporated Research Institutes for Seismology (IRIS/PASSCAL).

Saudi network station list

station	latitude	longitude	elevation
AFFS	24.5554	42.4823	964.8
ARSS	25.8275	43.1541	950.0
BDAS	28.4300	35.1000	100.0
BIDS	26.8669	36.9575	100.0
BLJS	19.9571	41.6051	100.0
BTHS	24.0462	50.8460	100.0
DJNS	17.7014	43.5449	100.0
DRBS	17.8281	42.3010	160.5
ENMS	19.0707	42.5717	1654.0
FDAS	21.8336	40.3589	200.0
FRAS	21.0584	40.5182	2000.0
FRJS	22.5907	39.3638	181.4
FRSS	16.7388	42.1146	100.0
HAQS	29.0500	34.9200	100.0
JAZS	17.0684	42.9174	173.0
JEDS	21.7197	39.4161	215.8
JLOS	28.7352	35.4916	100.0
KBRS	25.7886	39.2644	100.0
KFJS	28.1866	47.9416	100.0
LBNS	21.0469	39.9016	289.0
LNYS	25.0815	37.9439	1029.0
MDRS	22.0879	40.0017	896.4
NAMS	19.1702	42.2021	100.0
QLBS	28.6517	37.5942	999.0
RSHS	28.2998	34.7968	100.0
SHBS	21.0048	39.6829	100.0
SHMS	21.4485	39.6908	280.0
SLWS	24.7977	50.6438	100.0

TBKS	28.2292	36.5504	100.0
UMJS	25.2323	37.3109	100.0
WJHS	26.7320	36.3934	100.0
YNBS	24.3396	37.9939	100.0
YOBS	24.3575	38.7432	100.0

External network station list

station	latitude	longitude	elevation
ABKT	37.9304	58.1189	678.0
ANTO	39.8680	32.7934	895.0
FURI	8.8952	38.6798	2565.0
GNI	40.1480	44.7410	1509.0
KIV	43.9553	42.6863	1054.0
UOSS	24.9453	56.2042	284.4

Green's functions

The collection of empirical Green's function is being sent as a separate file

Saudi_ambient_noise_correlation_GFs.tar

which expands into a directory containing a collection of SAC formatted seismograms. The files use the following naming convention:

STA1.STA2.COMPONENT.HOURS.stacked.sac

and it's complement:

STA1.STA2.COMPONENT.HOURS.stacked.sac.rev

STA1 is listed in the SAC header variable kevnm representing the "virtual source".

STA2 is listed in the SAC header variable kstnm representing the reference station.

COMPONENT is listed in the SAC header variable kcmpnm and will be one of E,N or Z, representing either a correlation of the two East components, a correlation of the two North components, or a correlation of the two vertical components.

HOURS is the number of continuous hours that were correlated and stacked for the trace and is also listed in the SAC header variable unused15.

Files ending with the suffix "sac" are the raw Green's functions and will appear assymetric due to the azimuthal dependence of the source of the ambient noise.

Files ending with the suffix rev indicate that correlation trace was reversed around zero and stacked with the unreversed original. This combines the "causal" ($t > 0$) and "acausal" ($t < 0$) portions of the empirical Green's function and is done because the ambient noise energy in different bands often comes from different directions, some stacking preferentially on the "acausal" side others stacking preferentially on the "causal" side. This step results in Green's functions that look symmetric around zero. The measurements described elsewhere in this report were performed on these *.rev files.

1D Model inversions

Each trace was inverted using the Reflectivity method to obtain the best 1D velocity model along each of the 741 paths. Two inversion runs were done: One for a frequency band between 0.05-0.25 Hz and the other for a frequency band between 0.03-0.09 Hz. All models for distances less than 500 km are the result of the 0.05-0.25 Hz run. All models for distances greater than 1100 km are the result of the 0.03-0.09 Hz run. Models for distances between 500-1100 km are the result of the better of the two runs and tie directly to the SNR measurements listed below.

These 1D model results are provided in a separate spreadsheet

Saudi_ANC_1D_bestfit_model_results_ALL_DATA.xlsx.

The spreadsheet header contains the following variables:

seismogram file:	the name of the ANC Green's function SAC file.
distance:	inter-station distance in km.
azimuth:	azimuth from station1 to station2
seismogram:	an integer index used for sorting
0 130 :	the depth (km) of the layer. (40 layers total).

Localized 3D tomography

We used the results of the 1D model inversions to develop a 3D tomogram beneath the Saudi network. The locations of the stations determine the resolution of the model and for this study, the majority lie in the west, along the Red Sea coast. For this reason, together with the high SNR at long interstation distances, we've restricted the tomography to a region between $15^\circ - 30^\circ$ latitude and $34^\circ - 44^\circ$ longitude and used only the paths for stations separated by less than 1150 km. The results are provided separately in a file named:

Saudi_ambient_noise_correlation_local_tomography.tar

This tar file expands into a directory named SAUDI_TOMOGRAPHY containing 40 files (one for each layer in the model). The naming convention of the model files is

Saudi_local_tomography_ANC_DATA_###km.xyz

where ### is the depth (km) of the layer. The values in the files are GMT parsable (longitude, latitude, velocity) for each point in the model.

Group Velocity Measurements

We measured the group velocity for 23 bands with center frequencies ranging from 0.02 to 4.10 Hz. These bands were selected so that the center frequencies were evenly sampled in log10 space. The bands were defined such that

$$\text{lowpass} = 10^{(\log_{10}(\text{centerfreq}) - 0.1)}$$

$$\text{highpass} = 10^{(\log_{10}(\text{centerfreq}) + 0.1)}$$

Group velocities were measured over a time window defined by

$$\text{startcut} = \text{distance} / 4.8$$

$$\text{endcut} = \text{distance} / 2.0$$

The signal to noise ratio (SNR) for each trace was measured by calculating the time-domain RMS amplitude over a signal window and a noise window. The signal window was defined by the start and endcut above, with the exception that the duration of the time window was enforced to be at least 2/lowpass. The noise window was defined to begin 60 seconds after the signal window and be 60 seconds long, likewise with the exception that it's duration was forced to be at least 2/lowpass.

Below are the group velocity measurements for each of the (23) bands for all (741) station-pairs, listed in order of inter-station distance. These were all measured on the vertical component correlations and should be regarded as Rayleigh wave group velocities.

For each pair, there is a header line containing the following variables:

sta1	sta2	lat1	long1	lat2	long2	distance
------	------	------	-------	------	-------	----------

Followed by the string of measurements in each of 23 bands:

sta1	sta2	lowpass	highpass	distance	km/sec	SNR
------	------	---------	----------	----------	--------	-----

Note that where the group velocity (km/s) and SNR are listed as "-", the measurement was discarded, typically because an artifact in the trace led to a spurious result. Where SNR is listed as **-999.000** the noise window was of insufficient length for a measurement to be made.

LBNS	SHBS	21.047	39.902	21.005	39.683	23.17840
sta1	sta2	lowpass	highpass	distance	km/sec	SNR
LBNS	SHBS	0.01589	0.02518	23.17840	-	-
LBNS	SHBS	0.02000	0.03170	23.17840	-	-
LBNS	SHBS	0.02518	0.03991	23.17840	-	-
LBNS	SHBS	0.03170	0.05024	23.17840	-	-
LBNS	SHBS	0.03991	0.06325	23.17840	-	-
LBNS	SHBS	0.05024	0.07962	23.17840	4.750	35.139
LBNS	SHBS	0.06325	0.10024	23.17840	4.750	36.604

LBNS	SHBS	0.07962	0.12619	23.17840	-	-
LBNS	SHBS	0.10024	0.15887	23.17840	3.255	31.805
LBNS	SHBS	0.12619	0.20000	23.17840	3.738	30.750
LBNS	SHBS	0.15887	0.25179	23.17840	4.750	27.644
LBNS	SHBS	0.20000	0.31698	23.17840	2.130	12.931
LBNS	SHBS	0.25179	0.39905	23.17840	3.622	12.642
LBNS	SHBS	0.31698	0.50238	23.17840	2.941	16.317
LBNS	SHBS	0.39905	0.63246	23.17840	2.927	19.480
LBNS	SHBS	0.50238	0.79621	23.17840	2.927	14.588
LBNS	SHBS	0.63246	1.00237	23.17840	2.869	6.549
LBNS	SHBS	0.79621	1.26191	23.17840	2.786	4.053
LBNS	SHBS	1.00237	1.58866	23.17840	2.799	3.348
LBNS	SHBS	1.26191	2.00000	23.17840	2.799	2.545
LBNS	SHBS	1.58866	2.51785	23.17840	4.789	4.245
LBNS	SHBS	2.00000	3.16979	23.17840	4.789	4.157
LBNS	SHBS	2.51785	3.99052	23.17840	2.840	2.672
LBNS	SHBS	3.16979	5.02377	23.17840	4.110	3.087
BDAS	RSHS	28.430	35.100	28.300	34.797	33.01397
sta1	sta2	lowpass	highpass	distance	km/sec	SNR
BDAS	RSHS	0.01589	0.02518	33.01397	-	-
BDAS	RSHS	0.02000	0.03170	33.01397	-	-
BDAS	RSHS	0.02518	0.03991	33.01397	-	-
BDAS	RSHS	0.03170	0.05024	33.01397	-	-
BDAS	RSHS	0.03991	0.06325	33.01397	-	-
BDAS	RSHS	0.05024	0.07962	33.01397	-	-
BDAS	RSHS	0.06325	0.10024	33.01397	-	-
BDAS	RSHS	0.07962	0.12619	33.01397	3.328	37.262
BDAS	RSHS	0.10024	0.15887	33.01397	-	-
BDAS	RSHS	0.12619	0.20000	33.01397	-	-
BDAS	RSHS	0.15887	0.25179	33.01397	3.604	11.704
BDAS	RSHS	0.20000	0.31698	33.01397	2.231	11.799
BDAS	RSHS	0.25179	0.39905	33.01397	2.018	14.389
BDAS	RSHS	0.31698	0.50238	33.01397	-	-
BDAS	RSHS	0.39905	0.63246	33.01397	-	-
BDAS	RSHS	0.50238	0.79621	33.01397	2.595	2.757
BDAS	RSHS	0.63246	1.00237	33.01397	2.178	4.134
BDAS	RSHS	0.79621	1.26191	33.01397	2.161	3.820
BDAS	RSHS	1.00237	1.58866	33.01397	3.803	2.826
BDAS	RSHS	1.26191	2.00000	33.01397	3.875	2.010
BDAS	RSHS	1.58866	2.51785	33.01397	3.968	1.316
BDAS	RSHS	2.00000	3.16979	33.01397	2.213	1.545
BDAS	RSHS	2.51785	3.99052	33.01397	3.369	2.172
BDAS	RSHS	3.16979	5.02377	33.01397	3.328	2.222
ENMS	NAMS	19.071	42.572	19.170	42.202	40.37606
sta1	sta2	lowpass	highpass	distance	km/sec	SNR
ENMS	NAMS	0.01589	0.02518	40.37606	-	-
ENMS	NAMS	0.02000	0.03170	40.37606	3.505	1.119
ENMS	NAMS	0.02518	0.03991	40.37606	-	-
ENMS	NAMS	0.03170	0.05024	40.37606	-	-
ENMS	NAMS	0.03991	0.06325	40.37606	-	-
ENMS	NAMS	0.05024	0.07962	40.37606	2.582	11.852
ENMS	NAMS	0.06325	0.10024	40.37606	3.277	13.894
ENMS	NAMS	0.07962	0.12619	40.37606	3.542	19.990
ENMS	NAMS	0.10024	0.15887	40.37606	3.618	9.027
ENMS	NAMS	0.12619	0.20000	40.37606	3.554	4.817
ENMS	NAMS	0.15887	0.25179	40.37606	2.649	11.368
ENMS	NAMS	0.20000	0.31698	40.37606	2.917	17.413
ENMS	NAMS	0.25179	0.39905	40.37606	3.246	15.256
ENMS	NAMS	0.31698	0.50238	40.37606	3.184	8.204

ENMS	NAMS	0.39905	0.63246	40.37606	3.115	6.858
ENMS	NAMS	0.50238	0.79621	40.37606	3.077	6.289
ENMS	NAMS	0.63246	1.00237	40.37606	3.022	5.479
ENMS	NAMS	0.79621	1.26191	40.37606	2.969	4.022
ENMS	NAMS	1.00237	1.58866	40.37606	2.934	3.238
ENMS	NAMS	1.26191	2.00000	40.37606	-	-
ENMS	NAMS	1.58866	2.51785	40.37606	-	-
ENMS	NAMS	2.00000	3.16979	40.37606	3.752	1.296
ENMS	NAMS	2.51785	3.99052	40.37606	-	-
ENMS	NAMS	3.16979	5.02377	40.37606	3.096	4.083
JEDS	SHMS	21.720	39.416	21.448	39.691	41.42632
sta1	sta2	lowpass	highpass	distance	km/sec	SNR
JEDS	SHMS	0.01589	0.02518	41.42632	-	-
JEDS	SHMS	0.02000	0.03170	41.42632	-	-
JEDS	SHMS	0.02518	0.03991	41.42632	-	-
JEDS	SHMS	0.03170	0.05024	41.42632	-	-
JEDS	SHMS	0.03991	0.06325	41.42632	-	-
JEDS	SHMS	0.05024	0.07962	41.42632	2.830	5.481
JEDS	SHMS	0.06325	0.10024	41.42632	3.363	17.731
JEDS	SHMS	0.07962	0.12619	41.42632	3.647	27.818
JEDS	SHMS	0.10024	0.15887	41.42632	3.808	22.781
JEDS	SHMS	0.12619	0.20000	41.42632	-	-
JEDS	SHMS	0.15887	0.25179	41.42632	4.333	7.331
JEDS	SHMS	0.20000	0.31698	41.42632	-	-
JEDS	SHMS	0.25179	0.39905	41.42632	2.769	5.972
JEDS	SHMS	0.31698	0.50238	41.42632	2.784	9.009
JEDS	SHMS	0.39905	0.63246	41.42632	2.711	7.548
JEDS	SHMS	0.50238	0.79621	41.42632	2.642	3.152
JEDS	SHMS	0.63246	1.00237	41.42632	2.642	2.666
JEDS	SHMS	0.79621	1.26191	41.42632	3.571	3.861
JEDS	SHMS	1.00237	1.58866	41.42632	3.487	3.843
JEDS	SHMS	1.26191	2.00000	41.42632	3.547	2.131
JEDS	SHMS	1.58866	2.51785	41.42632	3.511	1.324
JEDS	SHMS	2.00000	3.16979	41.42632	3.475	1.073
JEDS	SHMS	2.51785	3.99052	41.42632	3.177	1.268
JEDS	SHMS	3.16979	5.02377	41.42632	-	-
FDAS	MDRS	21.834	40.359	22.088	40.002	46.43343
sta1	sta2	lowpass	highpass	distance	km/sec	SNR
FDAS	MDRS	0.01589	0.02518	46.43343	-	-
FDAS	MDRS	0.02000	0.03170	46.43343	-	-
FDAS	MDRS	0.02518	0.03991	46.43343	3.434	2.226
FDAS	MDRS	0.03170	0.05024	46.43343	-	-
FDAS	MDRS	0.03991	0.06325	46.43343	-	-
FDAS	MDRS	0.05024	0.07962	46.43343	2.880	13.803
FDAS	MDRS	0.06325	0.10024	46.43343	3.709	6.054
FDAS	MDRS	0.07962	0.12619	46.43343	3.445	5.360
FDAS	MDRS	0.10024	0.15887	46.43343	2.294	8.102
FDAS	MDRS	0.12619	0.20000	46.43343	3.745	14.746
FDAS	MDRS	0.15887	0.25179	46.43343	3.650	10.453
FDAS	MDRS	0.20000	0.31698	46.43343	3.279	4.687
FDAS	MDRS	0.25179	0.39905	46.43343	3.261	7.344
FDAS	MDRS	0.31698	0.50238	46.43343	3.063	6.861
FDAS	MDRS	0.39905	0.63246	46.43343	3.015	9.311
FDAS	MDRS	0.50238	0.79621	46.43343	2.984	7.701
FDAS	MDRS	0.63246	1.00237	46.43343	2.954	4.489
FDAS	MDRS	0.79621	1.26191	46.43343	2.784	3.114
FDAS	MDRS	1.00237	1.58866	46.43343	2.700	3.091
FDAS	MDRS	1.26191	2.00000	46.43343	2.738	1.832
FDAS	MDRS	1.58866	2.51785	46.43343	4.299	1.293

FDAS	MDRS	2.00000	3.16979	46.43343	3.307	1.048
FDAS	MDRS	2.51785	3.99052	46.43343	3.307	0.925
FDAS	MDRS	3.16979	5.02377	46.43343	4.059	1.115
SHBS	SHMS	21.005	39.683	21.448	39.691	49.34177
sta1	sta2	lowpass	highpass	distance	km/sec	SNR
SHBS	SHMS	0.01589	0.02518	49.34177	-	-
SHBS	SHMS	0.02000	0.03170	49.34177	2.559	6.184
SHBS	SHMS	0.02518	0.03991	49.34177	2.729	2.321
SHBS	SHMS	0.03170	0.05024	49.34177	-	-
SHBS	SHMS	0.03991	0.06325	49.34177	-	-
SHBS	SHMS	0.05024	0.07962	49.34177	2.855	12.140
SHBS	SHMS	0.06325	0.10024	49.34177	3.316	36.943
SHBS	SHMS	0.07962	0.12619	49.34177	3.307	14.577
SHBS	SHMS	0.10024	0.15887	49.34177	2.944	7.706
SHBS	SHMS	0.12619	0.20000	49.34177	4.098	9.610
SHBS	SHMS	0.15887	0.25179	49.34177	3.187	10.566
SHBS	SHMS	0.20000	0.31698	49.34177	3.221	25.395
SHBS	SHMS	0.25179	0.39905	49.34177	3.204	19.750
SHBS	SHMS	0.31698	0.50238	49.34177	3.107	12.815
SHBS	SHMS	0.39905	0.63246	49.34177	3.001	10.479
SHBS	SHMS	0.50238	0.79621	49.34177	3.016	8.290
SHBS	SHMS	0.63246	1.00237	49.34177	3.555	4.109
SHBS	SHMS	0.79621	1.26191	49.34177	-	-
SHBS	SHMS	1.00237	1.58866	49.34177	2.699	2.488
SHBS	SHMS	1.26191	2.00000	49.34177	2.909	2.367
SHBS	SHMS	1.58866	2.51785	49.34177	2.902	2.143
SHBS	SHMS	2.00000	3.16979	49.34177	3.928	1.966
SHBS	SHMS	2.51785	3.99052	49.34177	-	-
SHBS	SHMS	3.16979	5.02377	49.34177	4.800	3.292
LBNS	SHMS	21.047	39.902	21.448	39.691	49.71332
sta1	sta2	lowpass	highpass	distance	km/sec	SNR
LBNS	SHMS	0.01589	0.02518	49.71332	-	-
LBNS	SHMS	0.02000	0.03170	49.71332	2.547	10.334
LBNS	SHMS	0.02518	0.03991	49.71332	2.780	7.483
LBNS	SHMS	0.03170	0.05024	49.71332	2.451	7.917
LBNS	SHMS	0.03991	0.06325	49.71332	-	-
LBNS	SHMS	0.05024	0.07962	49.71332	3.433	9.456
LBNS	SHMS	0.06325	0.10024	49.71332	3.551	14.516
LBNS	SHMS	0.07962	0.12619	49.71332	2.447	11.669
LBNS	SHMS	0.10024	0.15887	49.71332	2.738	6.168
LBNS	SHMS	0.12619	0.20000	49.71332	4.171	10.515
LBNS	SHMS	0.15887	0.25179	49.71332	-	-
LBNS	SHMS	0.20000	0.31698	49.71332	4.271	3.890
LBNS	SHMS	0.25179	0.39905	49.71332	3.279	2.492
LBNS	SHMS	0.31698	0.50238	49.71332	3.179	2.215
LBNS	SHMS	0.39905	0.63246	49.71332	3.203	3.674
LBNS	SHMS	0.50238	0.79621	49.71332	3.179	4.512
LBNS	SHMS	0.63246	1.00237	49.71332	3.138	5.453
LBNS	SHMS	0.79621	1.26191	49.71332	3.054	6.605
LBNS	SHMS	1.00237	1.58866	49.71332	2.924	4.802
LBNS	SHMS	1.26191	2.00000	49.71332	2.911	2.955
LBNS	SHMS	1.58866	2.51785	49.71332	2.911	2.348
LBNS	SHMS	2.00000	3.16979	49.71332	4.439	2.638
LBNS	SHMS	2.51785	3.99052	49.71332	4.471	2.542
LBNS	SHMS	3.16979	5.02377	49.71332	4.157	2.547
BDAS	JLOS	28.430	35.100	28.735	35.492	51.12733
sta1	sta2	lowpass	highpass	distance	km/sec	SNR
BDAS	JLOS	0.01589	0.02518	51.12733	-	-

BDAS	JLOS	0.02000	0.03170	51.12733	-	-
BDAS	JLOS	0.02518	0.03991	51.12733	-	-
BDAS	JLOS	0.03170	0.05024	51.12733	-	-
BDAS	JLOS	0.03991	0.06325	51.12733	-	-
BDAS	JLOS	0.05024	0.07962	51.12733	3.080	30.090
BDAS	JLOS	0.06325	0.10024	51.12733	3.286	24.769
BDAS	JLOS	0.07962	0.12619	51.12733	3.195	17.739
BDAS	JLOS	0.10024	0.15887	51.12733	-	-
BDAS	JLOS	0.12619	0.20000	51.12733	-	-
BDAS	JLOS	0.15887	0.25179	51.12733	4.097	7.262
BDAS	JLOS	0.20000	0.31698	51.12733	2.398	5.371
BDAS	JLOS	0.25179	0.39905	51.12733	3.148	5.510
BDAS	JLOS	0.31698	0.50238	51.12733	3.195	6.580
BDAS	JLOS	0.39905	0.63246	51.12733	3.065	5.132
BDAS	JLOS	0.50238	0.79621	51.12733	3.087	3.933
BDAS	JLOS	0.63246	1.00237	51.12733	2.966	3.636
BDAS	JLOS	0.79621	1.26191	51.12733	2.912	3.494
BDAS	JLOS	1.00237	1.58866	51.12733	2.879	2.706
BDAS	JLOS	1.26191	2.00000	51.12733	2.952	2.366
BDAS	JLOS	1.58866	2.51785	51.12733	4.084	1.987
BDAS	JLOS	2.00000	3.16979	51.12733	4.110	2.573
BDAS	JLOS	2.51785	3.99052	51.12733	3.445	2.912
BDAS	JLOS	3.16979	5.02377	51.12733	3.125	3.327
BIDS	WJHS	26.867	36.958	26.732	36.393	57.96276
sta1	sta2	lowpass	highpass	distance	km/sec	SNR
BIDS	WJHS	0.01589	0.02518	57.96276	-	-
BIDS	WJHS	0.02000	0.03170	57.96276	-	-
BIDS	WJHS	0.02518	0.03991	57.96276	-	-
BIDS	WJHS	0.03170	0.05024	57.96276	-	-
BIDS	WJHS	0.03991	0.06325	57.96276	-	-
BIDS	WJHS	0.05024	0.07962	57.96276	3.271	33.150
BIDS	WJHS	0.06325	0.10024	57.96276	3.057	30.582
BIDS	WJHS	0.07962	0.12619	57.96276	3.032	18.846
BIDS	WJHS	0.10024	0.15887	57.96276	3.083	13.686
BIDS	WJHS	0.12619	0.20000	57.96276	2.975	11.682
BIDS	WJHS	0.15887	0.25179	57.96276	4.176	10.193
BIDS	WJHS	0.20000	0.31698	57.96276	2.910	5.247
BIDS	WJHS	0.25179	0.39905	57.96276	2.830	8.653
BIDS	WJHS	0.31698	0.50238	57.96276	2.755	11.987
BIDS	WJHS	0.39905	0.63246	57.96276	2.744	10.897
BIDS	WJHS	0.50238	0.79621	57.96276	2.760	8.532
BIDS	WJHS	0.63246	1.00237	57.96276	2.547	9.606
BIDS	WJHS	0.79621	1.26191	57.96276	2.529	6.607
BIDS	WJHS	1.00237	1.58866	57.96276	2.511	4.157
BIDS	WJHS	1.26191	2.00000	57.96276	2.565	1.866
BIDS	WJHS	1.58866	2.51785	57.96276	2.898	1.038
BIDS	WJHS	2.00000	3.16979	57.96276	2.792	0.993
BIDS	WJHS	2.51785	3.99052	57.96276	2.792	1.997
BIDS	WJHS	3.16979	5.02377	57.96276	3.793	2.116
FRAS	LBNS	21.058	40.518	21.047	39.902	63.99902
sta1	sta2	lowpass	highpass	distance	km/sec	SNR
FRAS	LBNS	0.01589	0.02518	63.99902	2.878	5.639
FRAS	LBNS	0.02000	0.03170	63.99902	-	-
FRAS	LBNS	0.02518	0.03991	63.99902	-	-
FRAS	LBNS	0.03170	0.05024	63.99902	-	-
FRAS	LBNS	0.03991	0.06325	63.99902	2.500	18.905
FRAS	LBNS	0.05024	0.07962	63.99902	2.260	25.128
FRAS	LBNS	0.06325	0.10024	63.99902	3.187	25.595
FRAS	LBNS	0.07962	0.12619	63.99902	3.150	24.992

FRAS	LBNS	0.10024	0.15887	63.99902	2.974	14.474
FRAS	LBNS	0.12619	0.20000	63.99902	3.077	9.567
FRAS	LBNS	0.15887	0.25179	63.99902	3.119	17.714
FRAS	LBNS	0.20000	0.31698	63.99902	2.991	18.971
FRAS	LBNS	0.25179	0.39905	63.99902	2.985	24.969
FRAS	LBNS	0.31698	0.50238	63.99902	2.925	18.476
FRAS	LBNS	0.39905	0.63246	63.99902	2.947	9.707
FRAS	LBNS	0.50238	0.79621	63.99902	2.893	4.612
FRAS	LBNS	0.63246	1.00237	63.99902	2.872	4.206
FRAS	LBNS	0.79621	1.26191	63.99902	2.837	4.633
FRAS	LBNS	1.00237	1.58866	63.99902	-	-
FRAS	LBNS	1.26191	2.00000	63.99902	-	-
FRAS	LBNS	1.58866	2.51785	63.99902	2.744	1.615
FRAS	LBNS	2.00000	3.16979	63.99902	3.756	1.412
FRAS	LBNS	2.51785	3.99052	63.99902	3.921	1.544
FRAS	LBNS	3.16979	5.02377	63.99902	3.883	1.763
HAQS	JLOS	29.050	34.920	28.735	35.492	65.73812
sta1	sta2	lowpass	highpass	distance	km/sec	SNR
HAQS	JLOS	0.01589	0.02518	65.73812	-	-
HAQS	JLOS	0.02000	0.03170	65.73812	-	-
HAQS	JLOS	0.02518	0.03991	65.73812	-	-
HAQS	JLOS	0.03170	0.05024	65.73812	2.914	5.539
HAQS	JLOS	0.03991	0.06325	65.73812	3.191	8.460
HAQS	JLOS	0.05024	0.07962	65.73812	3.179	12.709
HAQS	JLOS	0.06325	0.10024	65.73812	3.119	18.954
HAQS	JLOS	0.07962	0.12619	65.73812	3.445	28.556
HAQS	JLOS	0.10024	0.15887	65.73812	-	-
HAQS	JLOS	0.12619	0.20000	65.73812	2.600	16.070
HAQS	JLOS	0.15887	0.25179	65.73812	3.107	18.776
HAQS	JLOS	0.20000	0.31698	65.73812	3.072	8.668
HAQS	JLOS	0.25179	0.39905	65.73812	2.843	4.857
HAQS	JLOS	0.31698	0.50238	65.73812	2.771	4.805
HAQS	JLOS	0.39905	0.63246	65.73812	2.712	4.125
HAQS	JLOS	0.50238	0.79621	65.73812	2.730	3.637
HAQS	JLOS	0.63246	1.00237	65.73812	2.625	2.535
HAQS	JLOS	0.79621	1.26191	65.73812	-	-
HAQS	JLOS	1.00237	1.58866	65.73812	-	-
HAQS	JLOS	1.26191	2.00000	65.73812	-	-
HAQS	JLOS	1.58866	2.51785	65.73812	3.095	1.612
HAQS	JLOS	2.00000	3.16979	65.73812	3.089	1.553
HAQS	JLOS	2.51785	3.99052	65.73812	3.242	2.355
HAQS	JLOS	3.16979	5.02377	65.73812	3.222	3.246
LNYS	UMJS	25.081	37.944	25.232	37.311	65.87750
sta1	sta2	lowpass	highpass	distance	km/sec	SNR
LNYS	UMJS	0.01589	0.02518	65.87750	2.825	7.552
LNYS	UMJS	0.02000	0.03170	65.87750	-	-
LNYS	UMJS	0.02518	0.03991	65.87750	-	-
LNYS	UMJS	0.03170	0.05024	65.87750	-	-
LNYS	UMJS	0.03991	0.06325	65.87750	3.519	4.386
LNYS	UMJS	0.05024	0.07962	65.87750	3.417	14.011
LNYS	UMJS	0.06325	0.10024	65.87750	3.090	8.496
LNYS	UMJS	0.07962	0.12619	65.87750	3.186	5.310
LNYS	UMJS	0.10024	0.15887	65.87750	-	-
LNYS	UMJS	0.12619	0.20000	65.87750	2.820	5.813
LNYS	UMJS	0.15887	0.25179	65.87750	4.212	9.276
LNYS	UMJS	0.20000	0.31698	65.87750	3.179	3.896
LNYS	UMJS	0.25179	0.39905	65.87750	3.192	3.577
LNYS	UMJS	0.31698	0.50238	65.87750	3.000	3.096
LNYS	UMJS	0.39905	0.63246	65.87750	2.978	2.760

LNYS	UMJS	0.50238	0.79621	65.87750	2.884	2.288
LNYS	UMJS	0.63246	1.00237	65.87750	2.815	2.144
LNYS	UMJS	0.79621	1.26191	65.87750	2.754	1.867
LNYS	UMJS	1.00237	1.58866	65.87750	2.534	1.280
LNYS	UMJS	1.26191	2.00000	65.87750	3.769	1.064
LNYS	UMJS	1.58866	2.51785	65.87750	3.795	0.962
LNYS	UMJS	2.00000	3.16979	65.87750	-	-
LNYS	UMJS	2.51785	3.99052	65.87750	-	-
LNYS	UMJS	3.16979	5.02377	65.87750	3.684	2.031
BDAS	HAQS	28.430	35.100	29.050	34.920	71.13932
sta1	sta2	lowpass	highpass	distance	km/sec	SNR
BDAS	HAQS	0.01589	0.02518	71.13932	2.974	8.035
BDAS	HAQS	0.02000	0.03170	71.13932	3.051	6.820
BDAS	HAQS	0.02518	0.03991	71.13932	2.707	10.996
BDAS	HAQS	0.03170	0.05024	71.13932	2.749	12.171
BDAS	HAQS	0.03991	0.06325	71.13932	3.388	26.489
BDAS	HAQS	0.05024	0.07962	71.13932	2.477	20.145
BDAS	HAQS	0.06325	0.10024	71.13932	2.430	12.284
BDAS	HAQS	0.07962	0.12619	71.13932	2.608	14.109
BDAS	HAQS	0.10024	0.15887	71.13932	-	-
BDAS	HAQS	0.12619	0.20000	71.13932	3.768	3.547
BDAS	HAQS	0.15887	0.25179	71.13932	3.952	2.798
BDAS	HAQS	0.20000	0.31698	71.13932	2.078	4.170
BDAS	HAQS	0.25179	0.39905	71.13932	2.724	4.622
BDAS	HAQS	0.31698	0.50238	71.13932	2.757	3.404
BDAS	HAQS	0.39905	0.63246	71.13932	2.766	3.229
BDAS	HAQS	0.50238	0.79621	71.13932	4.234	2.520
BDAS	HAQS	0.63246	1.00237	71.13932	3.009	2.041
BDAS	HAQS	0.79621	1.26191	71.13932	3.004	1.214
BDAS	HAQS	1.00237	1.58866	71.13932	2.749	1.382
BDAS	HAQS	1.26191	2.00000	71.13932	2.775	1.750
BDAS	HAQS	1.58866	2.51785	71.13932	4.584	1.870
BDAS	HAQS	2.00000	3.16979	71.13932	4.413	2.070
BDAS	HAQS	2.51785	3.99052	71.13932	4.391	2.400
BDAS	HAQS	3.16979	5.02377	71.13932	4.042	2.733
JEDS	MDRS	21.720	39.416	22.088	40.002	72.98107
sta1	sta2	lowpass	highpass	distance	km/sec	SNR
JEDS	MDRS	0.01589	0.02518	72.98107	3.077	4.639
JEDS	MDRS	0.02000	0.03170	72.98107	-	-
JEDS	MDRS	0.02518	0.03991	72.98107	-	-
JEDS	MDRS	0.03170	0.05024	72.98107	-	-
JEDS	MDRS	0.03991	0.06325	72.98107	3.430	9.007
JEDS	MDRS	0.05024	0.07962	72.98107	3.098	8.342
JEDS	MDRS	0.06325	0.10024	72.98107	3.140	6.692
JEDS	MDRS	0.07962	0.12619	72.98107	3.241	5.727
JEDS	MDRS	0.10024	0.15887	72.98107	4.064	5.960
JEDS	MDRS	0.12619	0.20000	72.98107	2.887	6.880
JEDS	MDRS	0.15887	0.25179	72.98107	3.140	16.757
JEDS	MDRS	0.20000	0.31698	72.98107	2.943	17.949
JEDS	MDRS	0.25179	0.39905	72.98107	2.756	19.625
JEDS	MDRS	0.31698	0.50238	72.98107	2.735	13.660
JEDS	MDRS	0.39905	0.63246	72.98107	2.769	9.616
JEDS	MDRS	0.50238	0.79621	72.98107	2.559	6.012
JEDS	MDRS	0.63246	1.00237	72.98107	-	-
JEDS	MDRS	0.79621	1.26191	72.98107	-	-
JEDS	MDRS	1.00237	1.58866	72.98107	-	-
JEDS	MDRS	1.26191	2.00000	72.98107	3.072	1.696
JEDS	MDRS	1.58866	2.51785	72.98107	3.693	1.694
JEDS	MDRS	2.00000	3.16979	72.98107	3.671	1.710

JEDS	MDRS	2.51785	3.99052	72.98107	3.716	1.369
JEDS	MDRS	3.16979	5.02377	72.98107	3.701	1.452
YNBS	YOBS	24.340	37.994	24.358	38.743	75.93232
sta1	sta2	lowpass	highpass	distance	km/sec	SNR
YNBS	YOBS	0.01589	0.02518	75.93232	-	-
YNBS	YOBS	0.02000	0.03170	75.93232	-	-
YNBS	YOBS	0.02518	0.03991	75.93232	-	-
YNBS	YOBS	0.03170	0.05024	75.93232	2.943	15.836
YNBS	YOBS	0.03991	0.06325	75.93232	3.273	25.844
YNBS	YOBS	0.05024	0.07962	75.93232	3.228	52.798
YNBS	YOBS	0.06325	0.10024	75.93232	3.228	35.744
YNBS	YOBS	0.07962	0.12619	75.93232	3.196	26.850
YNBS	YOBS	0.10024	0.15887	75.93232	3.245	17.691
YNBS	YOBS	0.12619	0.20000	75.93232	3.279	8.092
YNBS	YOBS	0.15887	0.25179	75.93232	3.273	12.422
YNBS	YOBS	0.20000	0.31698	75.93232	3.153	11.389
YNBS	YOBS	0.25179	0.39905	75.93232	3.052	8.679
YNBS	YOBS	0.31698	0.50238	75.93232	3.042	7.681
YNBS	YOBS	0.39905	0.63246	75.93232	3.013	7.031
YNBS	YOBS	0.50238	0.79621	75.93232	2.966	5.360
YNBS	YOBS	0.63246	1.00237	75.93232	2.920	3.228
YNBS	YOBS	0.79621	1.26191	75.93232	2.939	2.354
YNBS	YOBS	1.00237	1.58866	75.93232	3.087	1.691
YNBS	YOBS	1.26191	2.00000	75.93232	2.138	1.848
YNBS	YOBS	1.58866	2.51785	75.93232	4.456	1.797
YNBS	YOBS	2.00000	3.16979	75.93232	2.674	2.017
YNBS	YOBS	2.51785	3.99052	75.93232	4.200	2.341
YNBS	YOBS	3.16979	5.02377	75.93232	3.866	2.906
MDRS	SHMS	22.088	40.002	21.448	39.691	78.01081
sta1	sta2	lowpass	highpass	distance	km/sec	SNR
MDRS	SHMS	0.01589	0.02518	78.01081	-	-
MDRS	SHMS	0.02000	0.03170	78.01081	-	-
MDRS	SHMS	0.02518	0.03991	78.01081	-	-
MDRS	SHMS	0.03170	0.05024	78.01081	-	-
MDRS	SHMS	0.03991	0.06325	78.01081	3.166	3.000
MDRS	SHMS	0.05024	0.07962	78.01081	3.422	20.657
MDRS	SHMS	0.06325	0.10024	78.01081	3.410	8.985
MDRS	SHMS	0.07962	0.12619	78.01081	3.076	5.348
MDRS	SHMS	0.10024	0.15887	78.01081	3.182	5.280
MDRS	SHMS	0.12619	0.20000	78.01081	-	-
MDRS	SHMS	0.15887	0.25179	78.01081	4.536	5.474
MDRS	SHMS	0.20000	0.31698	78.01081	3.289	11.309
MDRS	SHMS	0.25179	0.39905	78.01081	3.166	14.382
MDRS	SHMS	0.31698	0.50238	78.01081	3.166	10.739
MDRS	SHMS	0.39905	0.63246	78.01081	3.096	9.272
MDRS	SHMS	0.50238	0.79621	78.01081	3.024	7.279
MDRS	SHMS	0.63246	1.00237	78.01081	2.973	5.740
MDRS	SHMS	0.79621	1.26191	78.01081	2.964	4.391
MDRS	SHMS	1.00237	1.58866	78.01081	3.005	2.607
MDRS	SHMS	1.26191	2.00000	78.01081	3.645	1.559
MDRS	SHMS	1.58866	2.51785	78.01081	3.618	1.676
MDRS	SHMS	2.00000	3.16979	78.01081	3.300	1.553
MDRS	SHMS	2.51785	3.99052	78.01081	2.818	2.903
MDRS	SHMS	3.16979	5.02377	78.01081	3.802	3.117
FDAS	SHMS	21.834	40.359	21.448	39.691	81.24832
sta1	sta2	lowpass	highpass	distance	km/sec	SNR
FDAS	SHMS	0.01589	0.02518	81.24832	-	-
FDAS	SHMS	0.02000	0.03170	81.24832	-	-

FDAS	SHMS	0.02518	0.03991	81.24832	-	-
FDAS	SHMS	0.03170	0.05024	81.24832	2.898	6.864
FDAS	SHMS	0.03991	0.06325	81.24832	3.303	17.328
FDAS	SHMS	0.05024	0.07962	81.24832	3.466	17.257
FDAS	SHMS	0.06325	0.10024	81.24832	3.490	11.213
FDAS	SHMS	0.07962	0.12619	81.24832	3.276	11.342
FDAS	SHMS	0.10024	0.15887	81.24832	3.125	10.180
FDAS	SHMS	0.12619	0.20000	81.24832	3.234	9.933
FDAS	SHMS	0.15887	0.25179	81.24832	3.260	7.049
FDAS	SHMS	0.20000	0.31698	81.24832	3.260	13.104
FDAS	SHMS	0.25179	0.39905	81.24832	3.229	20.292
FDAS	SHMS	0.31698	0.50238	81.24832	3.149	17.257
FDAS	SHMS	0.39905	0.63246	81.24832	3.111	14.178
FDAS	SHMS	0.50238	0.79621	81.24832	3.068	11.356
FDAS	SHMS	0.63246	1.00237	81.24832	3.032	8.999
FDAS	SHMS	0.79621	1.26191	81.24832	3.005	4.729
FDAS	SHMS	1.00237	1.58866	81.24832	2.961	3.445
FDAS	SHMS	1.26191	2.00000	81.24832	3.570	2.006
FDAS	SHMS	1.58866	2.51785	81.24832	3.589	1.470
FDAS	SHMS	2.00000	3.16979	81.24832	3.693	1.702
FDAS	SHMS	2.51785	3.99052	81.24832	3.209	4.805
FDAS	SHMS	3.16979	5.02377	81.24832	3.204	4.995
LNYs	YNBS	25.081	37.944	24.340	37.994	82.65443
sta1	sta2	lowpass	highpass	distance	km/sec	SNR
LNYs	YNBS	0.01589	0.02518	82.65443	-	-
LNYs	YNBS	0.02000	0.03170	82.65443	-	-
LNYs	YNBS	0.02518	0.03991	82.65443	-	-
LNYs	YNBS	0.03170	0.05024	82.65443	2.348	2.041
LNYs	YNBS	0.03991	0.06325	82.65443	2.478	5.728
LNYs	YNBS	0.05024	0.07962	82.65443	3.285	10.148
LNYs	YNBS	0.06325	0.10024	82.65443	3.317	9.515
LNYs	YNBS	0.07962	0.12619	82.65443	3.234	4.597
LNYs	YNBS	0.10024	0.15887	82.65443	3.229	4.447
LNYs	YNBS	0.12619	0.20000	82.65443	3.338	6.967
LNYs	YNBS	0.15887	0.25179	82.65443	3.103	14.552
LNYs	YNBS	0.20000	0.31698	82.65443	3.121	11.451
LNYs	YNBS	0.25179	0.39905	82.65443	3.121	8.540
LNYs	YNBS	0.31698	0.50238	82.65443	3.052	5.172
LNYs	YNBS	0.39905	0.63246	82.65443	3.012	4.077
LNYs	YNBS	0.50238	0.79621	82.65443	3.008	4.950
LNYs	YNBS	0.63246	1.00237	82.65443	2.939	6.290
LNYs	YNBS	0.79621	1.26191	82.65443	2.850	3.380
LNYs	YNBS	1.00237	1.58866	82.65443	2.751	1.735
LNYs	YNBS	1.26191	2.00000	82.65443	2.719	2.015
LNYs	YNBS	1.58866	2.51785	82.65443	3.496	2.883
LNYs	YNBS	2.00000	3.16979	82.65443	3.455	3.518
LNYs	YNBS	2.51785	3.99052	82.65443	4.654	3.169
LNYs	YNBS	3.16979	5.02377	82.65443	3.600	3.240
JLOS	RSHS	28.735	35.492	28.300	34.797	83.38469
sta1	sta2	lowpass	highpass	distance	km/sec	SNR
JLOS	RSHS	0.01589	0.02518	83.38469	-	-
JLOS	RSHS	0.02000	0.03170	83.38469	-	-
JLOS	RSHS	0.02518	0.03991	83.38469	-	-
JLOS	RSHS	0.03170	0.05024	83.38469	-	-
JLOS	RSHS	0.03991	0.06325	83.38469	3.222	25.859
JLOS	RSHS	0.05024	0.07962	83.38469	3.492	24.164
JLOS	RSHS	0.06325	0.10024	83.38469	3.457	17.826
JLOS	RSHS	0.07962	0.12619	83.38469	3.469	13.800
JLOS	RSHS	0.10024	0.15887	83.38469	2.306	13.407

JLOS	RSHS	0.12619	0.20000	83.38469	2.402	10.565
JLOS	RSHS	0.15887	0.25179	83.38469	3.504	6.942
JLOS	RSHS	0.20000	0.31698	83.38469	3.217	5.895
JLOS	RSHS	0.25179	0.39905	83.38469	2.612	4.130
JLOS	RSHS	0.31698	0.50238	83.38469	2.382	3.246
JLOS	RSHS	0.39905	0.63246	83.38469	2.353	3.007
JLOS	RSHS	0.50238	0.79621	83.38469	2.306	2.322
JLOS	RSHS	0.63246	1.00237	83.38469	2.293	1.441
JLOS	RSHS	0.79621	1.26191	83.38469	2.283	1.807
JLOS	RSHS	1.00237	1.58866	83.38469	-	-
JLOS	RSHS	1.26191	2.00000	83.38469	-	-
JLOS	RSHS	1.58866	2.51785	83.38469	2.916	1.549
JLOS	RSHS	2.00000	3.16979	83.38469	2.622	1.822
JLOS	RSHS	2.51785	3.99052	83.38469	2.616	2.580
JLOS	RSHS	3.16979	5.02377	83.38469	4.522	2.790
JEDS	SHBS	21.720	39.416	21.005	39.683	84.15485
sta1	sta2	lowpass	highpass	distance	km/sec	SNR
JEDS	SHBS	0.01589	0.02518	84.15485	2.959	0.609
JEDS	SHBS	0.02000	0.03170	84.15485	2.972	0.659
JEDS	SHBS	0.02518	0.03991	84.15485	3.010	1.201
JEDS	SHBS	0.03170	0.05024	84.15485	2.673	4.270
JEDS	SHBS	0.03991	0.06325	84.15485	2.667	7.139
JEDS	SHBS	0.05024	0.07962	84.15485	2.646	6.820
JEDS	SHBS	0.06325	0.10024	84.15485	2.926	11.568
JEDS	SHBS	0.07962	0.12619	84.15485	2.993	24.435
JEDS	SHBS	0.10024	0.15887	84.15485	3.501	14.915
JEDS	SHBS	0.12619	0.20000	84.15485	3.318	10.208
JEDS	SHBS	0.15887	0.25179	84.15485	3.062	5.636
JEDS	SHBS	0.20000	0.31698	84.15485	3.049	9.470
JEDS	SHBS	0.25179	0.39905	84.15485	3.080	9.483
JEDS	SHBS	0.31698	0.50238	84.15485	3.049	6.174
JEDS	SHBS	0.39905	0.63246	84.15485	2.988	5.325
JEDS	SHBS	0.50238	0.79621	84.15485	3.006	2.571
JEDS	SHBS	0.63246	1.00237	84.15485	2.967	2.688
JEDS	SHBS	0.79621	1.26191	84.15485	2.855	3.324
JEDS	SHBS	1.00237	1.58866	84.15485	2.828	2.395
JEDS	SHBS	1.26191	2.00000	84.15485	3.685	1.696
JEDS	SHBS	1.58866	2.51785	84.15485	3.089	1.447
JEDS	SHBS	2.00000	3.16979	84.15485	3.103	1.226
JEDS	SHBS	2.51785	3.99052	84.15485	3.089	1.504
JEDS	SHBS	3.16979	5.02377	84.15485	3.665	1.984
HAQS	RSHS	29.050	34.920	28.300	34.797	84.28017
sta1	sta2	lowpass	highpass	distance	km/sec	SNR
HAQS	RSHS	0.01589	0.02518	84.28017	-	-
HAQS	RSHS	0.02000	0.03170	84.28017	-	-
HAQS	RSHS	0.02518	0.03991	84.28017	-	-
HAQS	RSHS	0.03170	0.05024	84.28017	2.963	13.242
HAQS	RSHS	0.03991	0.06325	84.28017	3.085	21.674
HAQS	RSHS	0.05024	0.07962	84.28017	3.040	27.260
HAQS	RSHS	0.06325	0.10024	84.28017	2.821	25.582
HAQS	RSHS	0.07962	0.12619	84.28017	2.878	15.106
HAQS	RSHS	0.10024	0.15887	84.28017	3.135	17.409
HAQS	RSHS	0.12619	0.20000	84.28017	3.426	11.767
HAQS	RSHS	0.15887	0.25179	84.28017	4.521	5.468
HAQS	RSHS	0.20000	0.31698	84.28017	2.794	4.974
HAQS	RSHS	0.25179	0.39905	84.28017	2.712	4.684
HAQS	RSHS	0.31698	0.50238	84.28017	2.588	3.124
HAQS	RSHS	0.39905	0.63246	84.28017	2.427	2.396
HAQS	RSHS	0.50238	0.79621	84.28017	3.398	1.961

HAQS	RSHS	0.63246	1.00237	84.28017	3.471	1.497
HAQS	RSHS	0.79621	1.26191	84.28017	3.483	1.658
HAQS	RSHS	1.00237	1.58866	84.28017	3.523	1.870
HAQS	RSHS	1.26191	2.00000	84.28017	4.521	1.250
HAQS	RSHS	1.58866	2.51785	84.28017	2.526	1.114
HAQS	RSHS	2.00000	3.16979	84.28017	2.984	1.637
HAQS	RSHS	2.51785	3.99052	84.28017	4.600	2.485
HAQS	RSHS	3.16979	5.02377	84.28017	3.671	2.768
BTHS	SLWS	24.046	50.846	24.798	50.644	86.03723
sta1	sta2	lowpass	highpass	distance	km/sec	SNR
BTHS	SLWS	0.01589	0.02518	86.03723	-	-
BTHS	SLWS	0.02000	0.03170	86.03723	-	-
BTHS	SLWS	0.02518	0.03991	86.03723	-	-
BTHS	SLWS	0.03170	0.05024	86.03723	2.620	4.679
BTHS	SLWS	0.03991	0.06325	86.03723	2.315	2.766
BTHS	SLWS	0.05024	0.07962	86.03723	2.455	3.526
BTHS	SLWS	0.06325	0.10024	86.03723	2.567	4.689
BTHS	SLWS	0.07962	0.12619	86.03723	2.826	8.344
BTHS	SLWS	0.10024	0.15887	86.03723	4.528	6.466
BTHS	SLWS	0.12619	0.20000	86.03723	4.606	6.584
BTHS	SLWS	0.15887	0.25179	86.03723	4.606	8.028
BTHS	SLWS	0.20000	0.31698	86.03723	4.646	3.125
BTHS	SLWS	0.25179	0.39905	86.03723	2.346	2.204
BTHS	SLWS	0.31698	0.50238	86.03723	2.008	1.704
BTHS	SLWS	0.39905	0.63246	86.03723	2.255	1.853
BTHS	SLWS	0.50238	0.79621	86.03723	2.231	2.163
BTHS	SLWS	0.63246	1.00237	86.03723	2.153	1.748
BTHS	SLWS	0.79621	1.26191	86.03723	2.144	1.117
BTHS	SLWS	1.00237	1.58866	86.03723	2.963	1.157
BTHS	SLWS	1.26191	2.00000	86.03723	2.967	1.035
BTHS	SLWS	1.58866	2.51785	86.03723	2.105	0.949
BTHS	SLWS	2.00000	3.16979	86.03723	3.520	0.973
BTHS	SLWS	2.51785	3.99052	86.03723	2.695	1.007
BTHS	SLWS	3.16979	5.02377	86.03723	2.692	1.127
FRJS	MDRS	22.591	39.364	22.088	40.002	86.19830
sta1	sta2	lowpass	highpass	distance	km/sec	SNR
FRJS	MDRS	0.01589	0.02518	86.19830	-	-
FRJS	MDRS	0.02000	0.03170	86.19830	-	-
FRJS	MDRS	0.02518	0.03991	86.19830	-	-
FRJS	MDRS	0.03170	0.05024	86.19830	3.741	3.618
FRJS	MDRS	0.03991	0.06325	86.19830	-	-
FRJS	MDRS	0.05024	0.07962	86.19830	3.031	9.269
FRJS	MDRS	0.06325	0.10024	86.19830	3.174	4.954
FRJS	MDRS	0.07962	0.12619	86.19830	3.132	3.183
FRJS	MDRS	0.10024	0.15887	86.19830	3.169	8.664
FRJS	MDRS	0.12619	0.20000	86.19830	2.590	6.589
FRJS	MDRS	0.15887	0.25179	86.19830	4.301	4.465
FRJS	MDRS	0.20000	0.31698	86.19830	3.421	6.026
FRJS	MDRS	0.25179	0.39905	86.19830	3.155	6.299
FRJS	MDRS	0.31698	0.50238	86.19830	3.128	5.247
FRJS	MDRS	0.39905	0.63246	86.19830	3.128	4.270
FRJS	MDRS	0.50238	0.79621	86.19830	2.972	2.836
FRJS	MDRS	0.63246	1.00237	86.19830	2.972	2.332
FRJS	MDRS	0.79621	1.26191	86.19830	3.092	2.103
FRJS	MDRS	1.00237	1.58866	86.19830	3.083	1.573
FRJS	MDRS	1.26191	2.00000	86.19830	2.964	1.667
FRJS	MDRS	1.58866	2.51785	86.19830	4.035	1.459
FRJS	MDRS	2.00000	3.16979	86.19830	2.365	1.043
FRJS	MDRS	2.51785	3.99052	86.19830	-	-

FRJS	MDRS	3.16979	5.02377	86.19830	-	-
FRAS	SHBS	21.058	40.518	21.005	39.683	86.90001
sta1	sta2	lowpass	highpass	distance	km/sec	SNR
FRAS	SHBS	0.01589	0.02518	86.90001	2.692	1.621
FRAS	SHBS	0.02000	0.03170	86.90001	-	-
FRAS	SHBS	0.02518	0.03991	86.90001	3.056	3.981
FRAS	SHBS	0.03170	0.05024	86.90001	3.465	8.204
FRAS	SHBS	0.03991	0.06325	86.90001	3.337	17.974
FRAS	SHBS	0.05024	0.07962	86.90001	3.095	34.641
FRAS	SHBS	0.06325	0.10024	86.90001	3.095	28.445
FRAS	SHBS	0.07962	0.12619	86.90001	3.099	25.414
FRAS	SHBS	0.10024	0.15887	86.90001	3.144	7.343
FRAS	SHBS	0.12619	0.20000	86.90001	3.034	4.387
FRAS	SHBS	0.15887	0.25179	86.90001	3.043	6.464
FRAS	SHBS	0.20000	0.31698	86.90001	3.009	10.685
FRAS	SHBS	0.25179	0.39905	86.90001	3.013	9.860
FRAS	SHBS	0.31698	0.50238	86.90001	2.960	10.498
FRAS	SHBS	0.39905	0.63246	86.90001	2.924	10.564
FRAS	SHBS	0.50238	0.79621	86.90001	2.901	6.793
FRAS	SHBS	0.63246	1.00237	86.90001	2.885	2.983
FRAS	SHBS	0.79621	1.26191	86.90001	3.651	2.417
FRAS	SHBS	1.00237	1.58866	86.90001	3.633	1.965
FRAS	SHBS	1.26191	2.00000	86.90001	3.615	1.319
FRAS	SHBS	1.58866	2.51785	86.90001	2.792	0.970
FRAS	SHBS	2.00000	3.16979	86.90001	2.874	0.953
FRAS	SHBS	2.51785	3.99052	86.90001	4.652	1.142
FRAS	SHBS	3.16979	5.02377	86.90001	4.154	1.969
FDAS	FRAS	21.834	40.359	21.058	40.518	87.76305
sta1	sta2	lowpass	highpass	distance	km/sec	SNR
FDAS	FRAS	0.01589	0.02518	87.76305	-	-
FDAS	FRAS	0.02000	0.03170	87.76305	-	-
FDAS	FRAS	0.02518	0.03991	87.76305	-	-
FDAS	FRAS	0.03170	0.05024	87.76305	3.706	5.403
FDAS	FRAS	0.03991	0.06325	87.76305	3.143	4.907
FDAS	FRAS	0.05024	0.07962	87.76305	2.631	8.456
FDAS	FRAS	0.06325	0.10024	87.76305	3.621	11.577
FDAS	FRAS	0.07962	0.12619	87.76305	3.161	16.183
FDAS	FRAS	0.10024	0.15887	87.76305	3.675	21.521
FDAS	FRAS	0.12619	0.20000	87.76305	-	-
FDAS	FRAS	0.15887	0.25179	87.76305	3.227	5.979
FDAS	FRAS	0.20000	0.31698	87.76305	3.340	9.130
FDAS	FRAS	0.25179	0.39905	87.76305	3.386	10.141
FDAS	FRAS	0.31698	0.50238	87.76305	3.134	5.660
FDAS	FRAS	0.39905	0.63246	87.76305	3.108	4.092
FDAS	FRAS	0.50238	0.79621	87.76305	3.117	4.448
FDAS	FRAS	0.63246	1.00237	87.76305	3.082	4.397
FDAS	FRAS	0.79621	1.26191	87.76305	3.060	3.232
FDAS	FRAS	1.00237	1.58866	87.76305	3.052	1.599
FDAS	FRAS	1.26191	2.00000	87.76305	3.022	1.365
FDAS	FRAS	1.58866	2.51785	87.76305	2.941	1.398
FDAS	FRAS	2.00000	3.16979	87.76305	4.397	1.449
FDAS	FRAS	2.51785	3.99052	87.76305	4.388	1.455
FDAS	FRAS	3.16979	5.02377	87.76305	4.379	1.695
JEDS	LBNS	21.720	39.416	21.047	39.902	90.13186
sta1	sta2	lowpass	highpass	distance	km/sec	SNR
JEDS	LBNS	0.01589	0.02518	90.13186	-	-
JEDS	LBNS	0.02000	0.03170	90.13186	-	-
JEDS	LBNS	0.02518	0.03991	90.13186	-	-

JEDS	LBNS	0.03170	0.05024	90.13186	3.974	4.071
JEDS	LBNS	0.03991	0.06325	90.13186	-	-
JEDS	LBNS	0.05024	0.07962	90.13186	3.285	11.136
JEDS	LBNS	0.06325	0.10024	90.13186	2.981	9.098
JEDS	LBNS	0.07962	0.12619	90.13186	2.938	11.612
JEDS	LBNS	0.10024	0.15887	90.13186	3.826	16.587
JEDS	LBNS	0.12619	0.20000	90.13186	-	-
JEDS	LBNS	0.15887	0.25179	90.13186	4.325	4.594
JEDS	LBNS	0.20000	0.31698	90.13186	3.289	6.628
JEDS	LBNS	0.25179	0.39905	90.13186	3.121	8.170
JEDS	LBNS	0.31698	0.50238	90.13186	3.078	4.947
JEDS	LBNS	0.39905	0.63246	90.13186	3.138	2.640
JEDS	LBNS	0.50238	0.79621	90.13186	-	-
JEDS	LBNS	0.63246	1.00237	90.13186	-	-
JEDS	LBNS	0.79621	1.26191	90.13186	3.205	11.443
JEDS	LBNS	1.00237	1.58866	90.13186	3.156	9.882
JEDS	LBNS	1.26191	2.00000	90.13186	2.856	4.434
JEDS	LBNS	1.58866	2.51785	90.13186	3.560	3.657
JEDS	LBNS	2.00000	3.16979	90.13186	3.560	1.413
JEDS	LBNS	2.51785	3.99052	90.13186	3.358	0.968
JEDS	LBNS	3.16979	5.02377	90.13186	2.569	0.964
FRSS	JAZS	16.739	42.115	17.068	42.917	92.94145
sta1	sta2	lowpass	highpass	distance	km/sec	SNR
FRSS	JAZS	0.01589	0.02518	92.94145	-	-
FRSS	JAZS	0.02000	0.03170	92.94145	-	-
FRSS	JAZS	0.02518	0.03991	92.94145	3.597	3.175
FRSS	JAZS	0.03170	0.05024	92.94145	3.712	4.226
FRSS	JAZS	0.03991	0.06325	92.94145	3.608	7.378
FRSS	JAZS	0.05024	0.07962	92.94145	3.422	14.904
FRSS	JAZS	0.06325	0.10024	92.94145	3.136	7.595
FRSS	JAZS	0.07962	0.12619	92.94145	2.378	3.776
FRSS	JAZS	0.10024	0.15887	92.94145	2.078	2.285
FRSS	JAZS	0.12619	0.20000	92.94145	-	-
FRSS	JAZS	0.15887	0.25179	92.94145	4.781	1.876
FRSS	JAZS	0.20000	0.31698	92.94145	-	-
FRSS	JAZS	0.25179	0.39905	92.94145	2.040	3.330
FRSS	JAZS	0.31698	0.50238	92.94145	2.128	2.201
FRSS	JAZS	0.39905	0.63246	92.94145	2.163	1.351
FRSS	JAZS	0.50238	0.79621	92.94145	2.226	1.192
FRSS	JAZS	0.63246	1.00237	92.94145	3.718	1.729
FRSS	JAZS	0.79621	1.26191	92.94145	3.515	1.404
FRSS	JAZS	1.00237	1.58866	92.94145	2.708	0.961
FRSS	JAZS	1.26191	2.00000	92.94145	2.338	0.899
FRSS	JAZS	1.58866	2.51785	92.94145	2.338	0.842
FRSS	JAZS	2.00000	3.16979	92.94145	3.254	0.839
FRSS	JAZS	2.51785	3.99052	92.94145	2.923	0.971
FRSS	JAZS	3.16979	5.02377	92.94145	3.828	0.997
FRAS	SHMS	21.058	40.518	21.448	39.691	96.09250
sta1	sta2	lowpass	highpass	distance	km/sec	SNR
FRAS	SHMS	0.01589	0.02518	96.09250	-	-
FRAS	SHMS	0.02000	0.03170	96.09250	-	-
FRAS	SHMS	0.02518	0.03991	96.09250	3.393	5.940
FRAS	SHMS	0.03170	0.05024	96.09250	3.437	10.087
FRAS	SHMS	0.03991	0.06325	96.09250	3.203	5.528
FRAS	SHMS	0.05024	0.07962	96.09250	3.088	9.518
FRAS	SHMS	0.06325	0.10024	96.09250	3.153	23.465
FRAS	SHMS	0.07962	0.12619	96.09250	3.251	14.384
FRAS	SHMS	0.10024	0.15887	96.09250	3.323	10.825
FRAS	SHMS	0.12619	0.20000	96.09250	3.220	11.003

FRAS	SHMS	0.15887	0.25179	96.09250	3.136	7.248
FRAS	SHMS	0.20000	0.31698	96.09250	3.144	8.544
FRAS	SHMS	0.25179	0.39905	96.09250	3.144	9.283
FRAS	SHMS	0.31698	0.50238	96.09250	3.096	7.180
FRAS	SHMS	0.39905	0.63246	96.09250	3.033	5.112
FRAS	SHMS	0.50238	0.79621	96.09250	2.988	5.181
FRAS	SHMS	0.63246	1.00237	96.09250	2.966	4.843
FRAS	SHMS	0.79621	1.26191	96.09250	2.969	3.983
FRAS	SHMS	1.00237	1.58866	96.09250	2.981	3.878
FRAS	SHMS	1.26191	2.00000	96.09250	3.033	2.000
FRAS	SHMS	1.58866	2.51785	96.09250	3.022	1.407
FRAS	SHMS	2.00000	3.16979	96.09250	3.602	1.977
FRAS	SHMS	2.51785	3.99052	96.09250	4.290	3.082
FRAS	SHMS	3.16979	5.02377	96.09250	3.825	3.870
DJNS	JAZS	17.701	43.545	17.068	42.917	96.89205
sta1	sta2	lowpass	highpass	distance	km/sec	SNR
DJNS	JAZS	0.01589	0.02518	96.89205	-	-
DJNS	JAZS	0.02000	0.03170	96.89205	-	-
DJNS	JAZS	0.02518	0.03991	96.89205	-	-
DJNS	JAZS	0.03170	0.05024	96.89205	2.547	9.763
DJNS	JAZS	0.03991	0.06325	96.89205	3.300	21.806
DJNS	JAZS	0.05024	0.07962	96.89205	3.282	20.941
DJNS	JAZS	0.06325	0.10024	96.89205	3.113	11.193
DJNS	JAZS	0.07962	0.12619	96.89205	2.998	11.531
DJNS	JAZS	0.10024	0.15887	96.89205	3.296	19.203
DJNS	JAZS	0.12619	0.20000	96.89205	3.158	7.702
DJNS	JAZS	0.15887	0.25179	96.89205	3.162	4.365
DJNS	JAZS	0.20000	0.31698	96.89205	3.035	7.699
DJNS	JAZS	0.25179	0.39905	96.89205	3.013	5.907
DJNS	JAZS	0.31698	0.50238	96.89205	3.043	3.175
DJNS	JAZS	0.39905	0.63246	96.89205	2.990	3.747
DJNS	JAZS	0.50238	0.79621	96.89205	2.972	4.316
DJNS	JAZS	0.63246	1.00237	96.89205	2.778	3.254
DJNS	JAZS	0.79621	1.26191	96.89205	2.800	1.591
DJNS	JAZS	1.00237	1.58866	96.89205	3.626	1.313
DJNS	JAZS	1.26191	2.00000	96.89205	3.578	1.455
DJNS	JAZS	1.58866	2.51785	96.89205	3.426	1.349
DJNS	JAZS	2.00000	3.16979	96.89205	4.071	1.069
DJNS	JAZS	2.51785	3.99052	96.89205	4.396	1.643
DJNS	JAZS	3.16979	5.02377	96.89205	4.412	2.206
FRJS	JEDS	22.591	39.364	21.720	39.416	97.00046
sta1	sta2	lowpass	highpass	distance	km/sec	SNR
FRJS	JEDS	0.01589	0.02518	97.00046	-	-
FRJS	JEDS	0.02000	0.03170	97.00046	-	-
FRJS	JEDS	0.02518	0.03991	97.00046	3.504	2.796
FRJS	JEDS	0.03170	0.05024	97.00046	3.469	2.731
FRJS	JEDS	0.03991	0.06325	97.00046	3.203	2.062
FRJS	JEDS	0.05024	0.07962	97.00046	3.121	3.653
FRJS	JEDS	0.06325	0.10024	97.00046	3.273	8.209
FRJS	JEDS	0.07962	0.12619	97.00046	2.856	21.815
FRJS	JEDS	0.10024	0.15887	97.00046	2.442	10.882
FRJS	JEDS	0.12619	0.20000	97.00046	2.292	6.106
FRJS	JEDS	0.15887	0.25179	97.00046	4.593	5.059
FRJS	JEDS	0.20000	0.31698	97.00046	2.662	4.055
FRJS	JEDS	0.25179	0.39905	97.00046	2.569	4.282
FRJS	JEDS	0.31698	0.50238	97.00046	2.547	3.251
FRJS	JEDS	0.39905	0.63246	97.00046	2.588	2.121
FRJS	JEDS	0.50238	0.79621	97.00046	4.783	2.016
FRJS	JEDS	0.63246	1.00237	97.00046	2.569	1.536

FRJS	JEDS	0.79621	1.26191	97.00046	2.580	2.081
FRJS	JEDS	1.00237	1.58866	97.00046	2.594	2.292
FRJS	JEDS	1.26191	2.00000	97.00046	2.932	1.619
FRJS	JEDS	1.58866	2.51785	97.00046	2.947	1.307
FRJS	JEDS	2.00000	3.16979	97.00046	3.899	1.301
FRJS	JEDS	2.51785	3.99052	97.00046	2.911	1.418
FRJS	JEDS	3.16979	5.02377	97.00046	3.742	1.608
FDAS	JEDS	21.834	40.359	21.720	39.416	98.16840
sta1	sta2	lowpass	highpass	distance	km/sec	SNR
FDAS	JEDS	0.01589	0.02518	98.16840	-	-
FDAS	JEDS	0.02000	0.03170	98.16840	-	-
FDAS	JEDS	0.02518	0.03991	98.16840	-	-
FDAS	JEDS	0.03170	0.05024	98.16840	3.567	4.397
FDAS	JEDS	0.03991	0.06325	98.16840	3.371	4.365
FDAS	JEDS	0.05024	0.07962	98.16840	3.087	9.624
FDAS	JEDS	0.06325	0.10024	98.16840	3.064	10.975
FDAS	JEDS	0.07962	0.12619	98.16840	3.083	10.378
FDAS	JEDS	0.10024	0.15887	98.16840	3.095	11.456
FDAS	JEDS	0.12619	0.20000	98.16840	3.134	10.623
FDAS	JEDS	0.15887	0.25179	98.16840	3.083	6.222
FDAS	JEDS	0.20000	0.31698	98.16840	3.019	8.731
FDAS	JEDS	0.25179	0.39905	98.16840	2.936	12.452
FDAS	JEDS	0.31698	0.50238	98.16840	2.922	7.755
FDAS	JEDS	0.39905	0.63246	98.16840	2.854	4.779
FDAS	JEDS	0.50238	0.79621	98.16840	2.476	5.619
FDAS	JEDS	0.63246	1.00237	98.16840	2.243	4.728
FDAS	JEDS	0.79621	1.26191	98.16840	2.245	4.793
FDAS	JEDS	1.00237	1.58866	98.16840	2.241	3.422
FDAS	JEDS	1.26191	2.00000	98.16840	3.171	1.807
FDAS	JEDS	1.58866	2.51785	98.16840	3.447	2.392
FDAS	JEDS	2.00000	3.16979	98.16840	3.437	2.022
FDAS	JEDS	2.51785	3.99052	98.16840	3.196	1.986
FDAS	JEDS	3.16979	5.02377	98.16840	3.423	2.316
FDAS	LBNS	21.834	40.359	21.047	39.902	99.45891
sta1	sta2	lowpass	highpass	distance	km/sec	SNR
FDAS	LBNS	0.01589	0.02518	99.45891	-	-
FDAS	LBNS	0.02000	0.03170	99.45891	2.788	0.819
FDAS	LBNS	0.02518	0.03991	99.45891	3.473	3.292
FDAS	LBNS	0.03170	0.05024	99.45891	3.522	5.625
FDAS	LBNS	0.03991	0.06325	99.45891	3.347	9.831
FDAS	LBNS	0.05024	0.07962	99.45891	3.217	12.666
FDAS	LBNS	0.06325	0.10024	99.45891	3.276	8.599
FDAS	LBNS	0.07962	0.12619	99.45891	3.728	7.294
FDAS	LBNS	0.10024	0.15887	99.45891	3.229	6.094
FDAS	LBNS	0.12619	0.20000	99.45891	3.221	3.729
FDAS	LBNS	0.15887	0.25179	99.45891	3.280	8.495
FDAS	LBNS	0.20000	0.31698	99.45891	3.259	18.350
FDAS	LBNS	0.25179	0.39905	99.45891	3.229	18.782
FDAS	LBNS	0.31698	0.50238	99.45891	3.167	19.570
FDAS	LBNS	0.39905	0.63246	99.45891	3.132	16.015
FDAS	LBNS	0.50238	0.79621	99.45891	3.074	8.128
FDAS	LBNS	0.63246	1.00237	99.45891	3.055	5.256
FDAS	LBNS	0.79621	1.26191	99.45891	3.010	4.499
FDAS	LBNS	1.00237	1.58866	99.45891	3.861	2.916
FDAS	LBNS	1.26191	2.00000	99.45891	3.066	1.481
FDAS	LBNS	1.58866	2.51785	99.45891	3.706	1.236
FDAS	LBNS	2.00000	3.16979	99.45891	4.294	1.294
FDAS	LBNS	2.51785	3.99052	99.45891	4.265	1.348
FDAS	LBNS	3.16979	5.02377	99.45891	4.529	1.436

DRBS	JAZS	17.828	42.301	17.068	42.917	106.82409
sta1	sta2	lowpass	highpass	distance	km/sec	SNR
DRBS	JAZS	0.01589	0.02518	106.82409	-	-
DRBS	JAZS	0.02000	0.03170	106.82409	2.994	0.479
DRBS	JAZS	0.02518	0.03991	106.82409	2.811	1.411
DRBS	JAZS	0.03170	0.05024	106.82409	3.359	3.485
DRBS	JAZS	0.03991	0.06325	106.82409	3.322	5.088
DRBS	JAZS	0.05024	0.07962	106.82409	3.330	5.082
DRBS	JAZS	0.06325	0.10024	106.82409	3.179	5.921
DRBS	JAZS	0.07962	0.12619	106.82409	2.928	5.604
DRBS	JAZS	0.10024	0.15887	106.82409	3.164	5.182
DRBS	JAZS	0.12619	0.20000	106.82409	3.848	5.630
DRBS	JAZS	0.15887	0.25179	106.82409	2.909	4.551
DRBS	JAZS	0.20000	0.31698	106.82409	2.875	7.570
DRBS	JAZS	0.25179	0.39905	106.82409	2.932	7.471
DRBS	JAZS	0.31698	0.50238	106.82409	2.938	3.830
DRBS	JAZS	0.39905	0.63246	106.82409	2.925	1.595
DRBS	JAZS	0.50238	0.79621	106.82409	2.642	1.817
DRBS	JAZS	0.63246	1.00237	106.82409	2.684	2.338
DRBS	JAZS	0.79621	1.26191	106.82409	2.642	2.145
DRBS	JAZS	1.00237	1.58866	106.82409	2.616	1.875
DRBS	JAZS	1.26191	2.00000	106.82409	2.558	1.576
DRBS	JAZS	1.58866	2.51785	106.82409	4.010	1.285
DRBS	JAZS	2.00000	3.16979	106.82409	3.704	1.103
DRBS	JAZS	2.51785	3.99052	106.82409	2.314	1.107
DRBS	JAZS	3.16979	5.02377	106.82409	2.292	1.125
BLJS	NAMS	19.957	41.605	19.170	42.202	107.55773
sta1	sta2	lowpass	highpass	distance	km/sec	SNR
BLJS	NAMS	0.01589	0.02518	107.55773	-	-
BLJS	NAMS	0.02000	0.03170	107.55773	-	-
BLJS	NAMS	0.02518	0.03991	107.55773	-	-
BLJS	NAMS	0.03170	0.05024	107.55773	-	-
BLJS	NAMS	0.03991	0.06325	107.55773	3.461	14.185
BLJS	NAMS	0.05024	0.07962	107.55773	3.320	13.230
BLJS	NAMS	0.06325	0.10024	107.55773	2.861	7.066
BLJS	NAMS	0.07962	0.12619	107.55773	3.123	4.239
BLJS	NAMS	0.10024	0.15887	107.55773	4.581	2.784
BLJS	NAMS	0.12619	0.20000	107.55773	4.565	4.152
BLJS	NAMS	0.15887	0.25179	107.55773	4.726	3.077
BLJS	NAMS	0.20000	0.31698	107.55773	3.399	5.365
BLJS	NAMS	0.25179	0.39905	107.55773	3.307	6.533
BLJS	NAMS	0.31698	0.50238	107.55773	3.259	6.618
BLJS	NAMS	0.39905	0.63246	107.55773	3.149	4.359
BLJS	NAMS	0.50238	0.79621	107.55773	3.109	2.653
BLJS	NAMS	0.63246	1.00237	107.55773	3.101	2.604
BLJS	NAMS	0.79621	1.26191	107.55773	2.998	1.776
BLJS	NAMS	1.00237	1.58866	107.55773	2.984	1.321
BLJS	NAMS	1.26191	2.00000	107.55773	3.543	1.257
BLJS	NAMS	1.58866	2.51785	107.55773	3.552	1.316
BLJS	NAMS	2.00000	3.16979	107.55773	3.648	1.326
BLJS	NAMS	2.51785	3.99052	107.55773	3.639	1.519
BLJS	NAMS	3.16979	5.02377	107.55773	3.639	2.667
QLBS	TBKS	28.652	37.594	28.229	36.550	112.35083
sta1	sta2	lowpass	highpass	distance	km/sec	SNR
QLBS	TBKS	0.01589	0.02518	112.35083	-	-
QLBS	TBKS	0.02000	0.03170	112.35083	3.438	2.335
QLBS	TBKS	0.02518	0.03991	112.35083	3.681	3.518
QLBS	TBKS	0.03170	0.05024	112.35083	3.277	4.945

QLBS	TBKS	0.03991	0.06325	112.35083	2.714	6.039
QLBS	TBKS	0.05024	0.07962	112.35083	2.837	8.055
QLBS	TBKS	0.06325	0.10024	112.35083	2.840	5.918
QLBS	TBKS	0.07962	0.12619	112.35083	2.941	5.298
QLBS	TBKS	0.10024	0.15887	112.35083	2.670	6.515
QLBS	TBKS	0.12619	0.20000	112.35083	2.655	6.342
QLBS	TBKS	0.15887	0.25179	112.35083	2.773	4.189
QLBS	TBKS	0.20000	0.31698	112.35083	2.584	3.828
QLBS	TBKS	0.25179	0.39905	112.35083	2.352	3.792
QLBS	TBKS	0.31698	0.50238	112.35083	2.189	4.646
QLBS	TBKS	0.39905	0.63246	112.35083	2.157	4.548
QLBS	TBKS	0.50238	0.79621	112.35083	2.837	2.251
QLBS	TBKS	0.63246	1.00237	112.35083	2.740	1.771
QLBS	TBKS	0.79621	1.26191	112.35083	4.269	1.403
QLBS	TBKS	1.00237	1.58866	112.35083	4.605	2.009
QLBS	TBKS	1.26191	2.00000	112.35083	-	-
QLBS	TBKS	1.58866	2.51785	112.35083	4.402	1.078
QLBS	TBKS	2.00000	3.16979	112.35083	4.149	1.169
QLBS	TBKS	2.51785	3.99052	112.35083	2.530	2.438
QLBS	TBKS	3.16979	5.02377	112.35083	3.348	2.669
LNYS	YOBS	25.081	37.944	24.358	38.743	114.01231
sta1	sta2	lowpass	highpass	distance	km/sec	SNR
LNYS	YOBS	0.01589	0.02518	114.01231	-	-
LNYS	YOBS	0.02000	0.03170	114.01231	-	-
LNYS	YOBS	0.02518	0.03991	114.01231	3.065	7.809
LNYS	YOBS	0.03170	0.05024	114.01231	2.582	8.612
LNYS	YOBS	0.03991	0.06325	114.01231	3.385	8.811
LNYS	YOBS	0.05024	0.07962	114.01231	3.361	3.251
LNYS	YOBS	0.06325	0.10024	114.01231	3.112	3.817
LNYS	YOBS	0.07962	0.12619	114.01231	3.013	7.802
LNYS	YOBS	0.10024	0.15887	114.01231	3.167	5.530
LNYS	YOBS	0.12619	0.20000	114.01231	4.372	2.187
LNYS	YOBS	0.15887	0.25179	114.01231	4.072	2.493
LNYS	YOBS	0.20000	0.31698	114.01231	2.923	6.875
LNYS	YOBS	0.25179	0.39905	114.01231	2.991	6.650
LNYS	YOBS	0.31698	0.50238	114.01231	3.042	3.323
LNYS	YOBS	0.39905	0.63246	114.01231	3.000	1.932
LNYS	YOBS	0.50238	0.79621	114.01231	3.013	1.391
LNYS	YOBS	0.63246	1.00237	114.01231	3.502	1.351
LNYS	YOBS	0.79621	1.26191	114.01231	3.523	1.619
LNYS	YOBS	1.00237	1.58866	114.01231	3.563	1.268
LNYS	YOBS	1.26191	2.00000	114.01231	4.210	1.230
LNYS	YOBS	1.58866	2.51785	114.01231	3.192	2.340
LNYS	YOBS	2.00000	3.16979	114.01231	4.575	4.079
LNYS	YOBS	2.51785	3.99052	114.01231	3.770	3.426
LNYS	YOBS	3.16979	5.02377	114.01231	4.790	2.571
FDAS	SHBS	21.834	40.359	21.005	39.683	115.71104
sta1	sta2	lowpass	highpass	distance	km/sec	SNR
FDAS	SHBS	0.01589	0.02518	115.71104	2.407	0.646
FDAS	SHBS	0.02000	0.03170	115.71104	3.541	1.366
FDAS	SHBS	0.02518	0.03991	115.71104	3.699	2.258
FDAS	SHBS	0.03170	0.05024	115.71104	3.494	9.482
FDAS	SHBS	0.03991	0.06325	115.71104	3.284	9.382
FDAS	SHBS	0.05024	0.07962	115.71104	3.218	6.961
FDAS	SHBS	0.06325	0.10024	115.71104	3.091	7.812
FDAS	SHBS	0.07962	0.12619	115.71104	3.364	17.739
FDAS	SHBS	0.10024	0.15887	115.71104	3.348	18.623
FDAS	SHBS	0.12619	0.20000	115.71104	3.261	6.952
FDAS	SHBS	0.15887	0.25179	115.71104	3.254	6.034

FDAS	SHBS	0.20000	0.31698	115.71104	3.186	10.201
FDAS	SHBS	0.25179	0.39905	115.71104	3.182	15.262
FDAS	SHBS	0.31698	0.50238	115.71104	3.168	12.430
FDAS	SHBS	0.39905	0.63246	115.71104	3.117	6.932
FDAS	SHBS	0.50238	0.79621	115.71104	3.077	4.462
FDAS	SHBS	0.63246	1.00237	115.71104	3.048	3.137
FDAS	SHBS	0.79621	1.26191	115.71104	3.032	2.989
FDAS	SHBS	1.00237	1.58866	115.71104	2.970	2.164
FDAS	SHBS	1.26191	2.00000	115.71104	3.893	1.287
FDAS	SHBS	1.58866	2.51785	115.71104	4.344	0.981
FDAS	SHBS	2.00000	3.16979	115.71104	4.370	1.042
FDAS	SHBS	2.51785	3.99052	115.71104	4.396	1.253
FDAS	SHBS	3.16979	5.02377	115.71104	3.580	1.922
LBNS	MDRS	21.047	39.902	22.088	40.002	116.21587
sta1	sta2	lowpass	highpass	distance	km/sec	SNR
LBNS	MDRS	0.01589	0.02518	116.21587	-	-
LBNS	MDRS	0.02000	0.03170	116.21587	-	-
LBNS	MDRS	0.02518	0.03991	116.21587	3.203	3.784
LBNS	MDRS	0.03170	0.05024	116.21587	2.466	2.444
LBNS	MDRS	0.03991	0.06325	116.21587	3.565	3.896
LBNS	MDRS	0.05024	0.07962	116.21587	3.305	6.765
LBNS	MDRS	0.06325	0.10024	116.21587	3.210	7.641
LBNS	MDRS	0.07962	0.12619	116.21587	3.214	10.211
LBNS	MDRS	0.10024	0.15887	116.21587	3.302	11.220
LBNS	MDRS	0.12619	0.20000	116.21587	3.916	8.323
LBNS	MDRS	0.15887	0.25179	116.21587	4.671	13.748
LBNS	MDRS	0.20000	0.31698	116.21587	3.225	19.230
LBNS	MDRS	0.25179	0.39905	116.21587	3.186	16.319
LBNS	MDRS	0.31698	0.50238	116.21587	3.134	14.175
LBNS	MDRS	0.39905	0.63246	116.21587	3.101	10.858
LBNS	MDRS	0.50238	0.79621	116.21587	3.078	9.419
LBNS	MDRS	0.63246	1.00237	116.21587	3.039	10.452
LBNS	MDRS	0.79621	1.26191	116.21587	2.995	7.241
LBNS	MDRS	1.00237	1.58866	116.21587	2.977	2.960
LBNS	MDRS	1.26191	2.00000	116.21587	2.971	1.106
LBNS	MDRS	1.58866	2.51785	116.21587	-	-
LBNS	MDRS	2.00000	3.16979	116.21587	-	-
LBNS	MDRS	2.51785	3.99052	116.21587	3.547	1.206
LBNS	MDRS	3.16979	5.02377	116.21587	3.355	1.237
JLOS	TBKS	28.735	35.492	28.229	36.550	117.79240
sta1	sta2	lowpass	highpass	distance	km/sec	SNR
JLOS	TBKS	0.01589	0.02518	117.79240	-	-
JLOS	TBKS	0.02000	0.03170	117.79240	3.539	3.599
JLOS	TBKS	0.02518	0.03991	117.79240	3.600	11.356
JLOS	TBKS	0.03170	0.05024	117.79240	3.365	16.639
JLOS	TBKS	0.03991	0.06325	117.79240	3.268	10.944
JLOS	TBKS	0.05024	0.07962	117.79240	3.103	15.967
JLOS	TBKS	0.06325	0.10024	117.79240	2.815	16.318
JLOS	TBKS	0.07962	0.12619	117.79240	3.011	13.822
JLOS	TBKS	0.10024	0.15887	117.79240	3.408	12.318
JLOS	TBKS	0.12619	0.20000	117.79240	2.865	8.380
JLOS	TBKS	0.15887	0.25179	117.79240	2.663	8.945
JLOS	TBKS	0.20000	0.31698	117.79240	2.921	7.564
JLOS	TBKS	0.25179	0.39905	117.79240	3.489	4.404
JLOS	TBKS	0.31698	0.50238	117.79240	2.434	4.545
JLOS	TBKS	0.39905	0.63246	117.79240	2.426	6.049
JLOS	TBKS	0.50238	0.79621	117.79240	2.365	5.446
JLOS	TBKS	0.63246	1.00237	117.79240	2.172	3.116
JLOS	TBKS	0.79621	1.26191	117.79240	2.148	1.988

JLOS	TBKS	1.00237	1.58866	117.79240	2.350	2.017
JLOS	TBKS	1.26191	2.00000	117.79240	2.354	1.941
JLOS	TBKS	1.58866	2.51785	117.79240	2.348	1.507
JLOS	TBKS	2.00000	3.16979	117.79240	2.981	1.549
JLOS	TBKS	2.51785	3.99052	117.79240	2.969	2.680
JLOS	TBKS	3.16979	5.02377	117.79240	3.645	2.683
UMJS	YNBS	25.232	37.311	24.340	37.994	120.86263
sta1	sta2	lowpass	highpass	distance	km/sec	SNR
UMJS	YNBS	0.01589	0.02518	120.86263	-	-
UMJS	YNBS	0.02000	0.03170	120.86263	3.485	1.829
UMJS	YNBS	0.02518	0.03991	120.86263	3.981	6.285
UMJS	YNBS	0.03170	0.05024	120.86263	-	-
UMJS	YNBS	0.03991	0.06325	120.86263	3.218	16.061
UMJS	YNBS	0.05024	0.07962	120.86263	2.911	7.486
UMJS	YNBS	0.06325	0.10024	120.86263	2.813	3.049
UMJS	YNBS	0.07962	0.12619	120.86263	3.267	3.248
UMJS	YNBS	0.10024	0.15887	120.86263	3.395	4.642
UMJS	YNBS	0.12619	0.20000	120.86263	4.656	3.197
UMJS	YNBS	0.15887	0.25179	120.86263	4.714	2.198
UMJS	YNBS	0.20000	0.31698	120.86263	3.141	2.284
UMJS	YNBS	0.25179	0.39905	120.86263	3.141	3.418
UMJS	YNBS	0.31698	0.50238	120.86263	3.161	3.436
UMJS	YNBS	0.39905	0.63246	120.86263	3.134	2.470
UMJS	YNBS	0.50238	0.79621	120.86263	3.093	2.394
UMJS	YNBS	0.63246	1.00237	120.86263	2.965	2.027
UMJS	YNBS	0.79621	1.26191	120.86263	2.936	1.359
UMJS	YNBS	1.00237	1.58866	120.86263	2.720	1.436
UMJS	YNBS	1.26191	2.00000	120.86263	3.177	1.304
UMJS	YNBS	1.58866	2.51785	120.86263	3.542	1.290
UMJS	YNBS	2.00000	3.16979	120.86263	3.509	1.623
UMJS	YNBS	2.51785	3.99052	120.86263	3.509	1.930
UMJS	YNBS	3.16979	5.02377	120.86263	4.758	2.139
DRBS	FRSS	17.828	42.301	16.739	42.115	122.73074
sta1	sta2	lowpass	highpass	distance	km/sec	SNR
DRBS	FRSS	0.01589	0.02518	122.73074	-	-
DRBS	FRSS	0.02000	0.03170	122.73074	3.296	1.914
DRBS	FRSS	0.02518	0.03991	122.73074	2.950	2.407
DRBS	FRSS	0.03170	0.05024	122.73074	2.718	3.256
DRBS	FRSS	0.03991	0.06325	122.73074	3.243	12.124
DRBS	FRSS	0.05024	0.07962	122.73074	3.023	9.296
DRBS	FRSS	0.06325	0.10024	122.73074	2.917	7.456
DRBS	FRSS	0.07962	0.12619	122.73074	2.563	6.180
DRBS	FRSS	0.10024	0.15887	122.73074	2.561	4.975
DRBS	FRSS	0.12619	0.20000	122.73074	4.453	7.587
DRBS	FRSS	0.15887	0.25179	122.73074	4.486	5.091
DRBS	FRSS	0.20000	0.31698	122.73074	4.525	3.443
DRBS	FRSS	0.25179	0.39905	122.73074	4.742	2.443
DRBS	FRSS	0.31698	0.50238	122.73074	3.020	1.791
DRBS	FRSS	0.39905	0.63246	122.73074	2.429	1.294
DRBS	FRSS	0.50238	0.79621	122.73074	2.138	1.354
DRBS	FRSS	0.63246	1.00237	122.73074	2.340	1.286
DRBS	FRSS	0.79621	1.26191	122.73074	2.375	1.005
DRBS	FRSS	1.00237	1.58866	122.73074	3.964	0.914
DRBS	FRSS	1.26191	2.00000	122.73074	2.382	0.962
DRBS	FRSS	1.58866	2.51785	122.73074	2.429	1.026
DRBS	FRSS	2.00000	3.16979	122.73074	2.170	1.132
DRBS	FRSS	2.51785	3.99052	122.73074	2.710	1.245
DRBS	FRSS	3.16979	5.02377	122.73074	2.165	1.140

MDRS	SHBS	22.088	40.002	21.005	39.683	124.86533
sta1	sta2	lowpass	highpass	distance	km/sec	SNR
MDRS	SHBS	0.01589	0.02518	124.86533	-	-
MDRS	SHBS	0.02000	0.03170	124.86533	3.289	3.167
MDRS	SHBS	0.02518	0.03991	124.86533	2.869	1.751
MDRS	SHBS	0.03170	0.05024	124.86533	3.328	2.968
MDRS	SHBS	0.03991	0.06325	124.86533	3.596	12.273
MDRS	SHBS	0.05024	0.07962	124.86533	3.185	12.399
MDRS	SHBS	0.06325	0.10024	124.86533	3.185	7.191
MDRS	SHBS	0.07962	0.12619	124.86533	3.195	7.173
MDRS	SHBS	0.10024	0.15887	124.86533	3.258	6.522
MDRS	SHBS	0.12619	0.20000	124.86533	3.258	3.597
MDRS	SHBS	0.15887	0.25179	124.86533	3.353	4.336
MDRS	SHBS	0.20000	0.31698	124.86533	3.198	9.951
MDRS	SHBS	0.25179	0.39905	124.86533	3.147	11.646
MDRS	SHBS	0.31698	0.50238	124.86533	3.134	7.909
MDRS	SHBS	0.39905	0.63246	124.86533	3.128	4.195
MDRS	SHBS	0.50238	0.79621	124.86533	3.140	2.863
MDRS	SHBS	0.63246	1.00237	124.86533	2.835	2.268
MDRS	SHBS	0.79621	1.26191	124.86533	2.864	2.246
MDRS	SHBS	1.00237	1.58866	124.86533	2.843	1.553
MDRS	SHBS	1.26191	2.00000	124.86533	3.085	1.225
MDRS	SHBS	1.58866	2.51785	124.86533	2.134	1.141
MDRS	SHBS	2.00000	3.16979	124.86533	-	-
MDRS	SHBS	2.51785	3.99052	124.86533	4.033	1.343
MDRS	SHBS	3.16979	5.02377	124.86533	3.057	1.637
FRAS	MDRS	21.058	40.518	22.088	40.002	126.32094
sta1	sta2	lowpass	highpass	distance	km/sec	SNR
FRAS	MDRS	0.01589	0.02518	126.32094	-	-
FRAS	MDRS	0.02000	0.03170	126.32094	3.381	2.167
FRAS	MDRS	0.02518	0.03991	126.32094	3.392	11.232
FRAS	MDRS	0.03170	0.05024	126.32094	2.261	2.759
FRAS	MDRS	0.03991	0.06325	126.32094	3.164	2.918
FRAS	MDRS	0.05024	0.07962	126.32094	3.216	2.589
FRAS	MDRS	0.06325	0.10024	126.32094	3.193	4.445
FRAS	MDRS	0.07962	0.12619	126.32094	3.145	6.555
FRAS	MDRS	0.10024	0.15887	126.32094	3.136	8.050
FRAS	MDRS	0.12619	0.20000	126.32094	3.193	8.387
FRAS	MDRS	0.15887	0.25179	126.32094	3.219	5.769
FRAS	MDRS	0.20000	0.31698	126.32094	3.252	5.585
FRAS	MDRS	0.25179	0.39905	126.32094	3.256	3.801
FRAS	MDRS	0.31698	0.50238	126.32094	3.249	2.368
FRAS	MDRS	0.39905	0.63246	126.32094	3.161	2.410
FRAS	MDRS	0.50238	0.79621	126.32094	3.099	1.950
FRAS	MDRS	0.63246	1.00237	126.32094	3.711	1.475
FRAS	MDRS	0.79621	1.26191	126.32094	2.951	1.452
FRAS	MDRS	1.00237	1.58866	126.32094	2.965	1.494
FRAS	MDRS	1.26191	2.00000	126.32094	3.938	1.268
FRAS	MDRS	1.58866	2.51785	126.32094	3.933	1.349
FRAS	MDRS	2.00000	3.16979	126.32094	3.626	1.219
FRAS	MDRS	2.51785	3.99052	126.32094	4.423	1.063
FRAS	MDRS	3.16979	5.02377	126.32094	4.617	1.284
FRJS	SHMS	22.591	39.364	21.448	39.691	131.40378
sta1	sta2	lowpass	highpass	distance	km/sec	SNR
FRJS	SHMS	0.01589	0.02518	131.40378	-	-
FRJS	SHMS	0.02000	0.03170	131.40378	3.968	0.769
FRJS	SHMS	0.02518	0.03991	131.40378	-	-
FRJS	SHMS	0.03170	0.05024	131.40378	-	-
FRJS	SHMS	0.03991	0.06325	131.40378	3.404	4.877

FRJS	SHMS	0.05024	0.07962	131.40378	3.102	7.267
FRJS	SHMS	0.06325	0.10024	131.40378	3.025	5.413
FRJS	SHMS	0.07962	0.12619	131.40378	2.882	6.740
FRJS	SHMS	0.10024	0.15887	131.40378	2.637	6.365
FRJS	SHMS	0.12619	0.20000	131.40378	2.323	5.784
FRJS	SHMS	0.15887	0.25179	131.40378	2.259	6.418
FRJS	SHMS	0.20000	0.31698	131.40378	3.339	6.482
FRJS	SHMS	0.25179	0.39905	131.40378	2.854	5.675
FRJS	SHMS	0.31698	0.50238	131.40378	2.825	3.539
FRJS	SHMS	0.39905	0.63246	131.40378	2.832	4.468
FRJS	SHMS	0.50238	0.79621	131.40378	3.540	2.718
FRJS	SHMS	0.63246	1.00237	131.40378	3.563	1.544
FRJS	SHMS	0.79621	1.26191	131.40378	3.575	2.190
FRJS	SHMS	1.00237	1.58866	131.40378	3.418	1.921
FRJS	SHMS	1.26191	2.00000	131.40378	3.920	1.391
FRJS	SHMS	1.58866	2.51785	131.40378	2.136	1.049
FRJS	SHMS	2.00000	3.16979	131.40378	2.163	1.006
FRJS	SHMS	2.51785	3.99052	131.40378	3.397	1.706
FRJS	SHMS	3.16979	5.02377	131.40378	3.679	2.445
DJNS	DRBS	17.701	43.545	17.828	42.301	132.47115
sta1	sta2	lowpass	highpass	distance	km/sec	SNR
DJNS	DRBS	0.01589	0.02518	132.47115	-	-
DJNS	DRBS	0.02000	0.03170	132.47115	3.464	3.254
DJNS	DRBS	0.02518	0.03991	132.47115	3.421	6.077
DJNS	DRBS	0.03170	0.05024	132.47115	3.276	4.499
DJNS	DRBS	0.03991	0.06325	132.47115	3.148	8.467
DJNS	DRBS	0.05024	0.07962	132.47115	3.113	21.088
DJNS	DRBS	0.06325	0.10024	132.47115	3.089	18.115
DJNS	DRBS	0.07962	0.12619	132.47115	3.197	11.495
DJNS	DRBS	0.10024	0.15887	132.47115	3.244	12.011
DJNS	DRBS	0.12619	0.20000	132.47115	3.218	8.183
DJNS	DRBS	0.15887	0.25179	132.47115	3.101	5.176
DJNS	DRBS	0.20000	0.31698	132.47115	3.061	8.304
DJNS	DRBS	0.25179	0.39905	132.47115	3.101	9.069
DJNS	DRBS	0.31698	0.50238	132.47115	3.084	8.100
DJNS	DRBS	0.39905	0.63246	132.47115	3.024	6.460
DJNS	DRBS	0.50238	0.79621	132.47115	2.986	7.650
DJNS	DRBS	0.63246	1.00237	132.47115	2.981	4.735
DJNS	DRBS	0.79621	1.26191	132.47115	2.915	3.033
DJNS	DRBS	1.00237	1.58866	132.47115	2.867	1.988
DJNS	DRBS	1.26191	2.00000	132.47115	3.815	1.578
DJNS	DRBS	1.58866	2.51785	132.47115	2.218	1.066
DJNS	DRBS	2.00000	3.16979	132.47115	2.220	1.097
DJNS	DRBS	2.51785	3.99052	132.47115	2.284	1.104
DJNS	DRBS	3.16979	5.02377	132.47115	3.573	1.512
FDAS	FRJS	21.834	40.359	22.591	39.364	132.58727
sta1	sta2	lowpass	highpass	distance	km/sec	SNR
FDAS	FRJS	0.01589	0.02518	132.58727	-	-
FDAS	FRJS	0.02000	0.03170	132.58727	3.767	2.015
FDAS	FRJS	0.02518	0.03991	132.58727	-	-
FDAS	FRJS	0.03170	0.05024	132.58727	-	-
FDAS	FRJS	0.03991	0.06325	132.58727	3.154	3.347
FDAS	FRJS	0.05024	0.07962	132.58727	3.215	4.297
FDAS	FRJS	0.06325	0.10024	132.58727	3.041	5.263
FDAS	FRJS	0.07962	0.12619	132.58727	3.234	7.183
FDAS	FRJS	0.10024	0.15887	132.58727	3.234	6.421
FDAS	FRJS	0.12619	0.20000	132.58727	3.178	4.535
FDAS	FRJS	0.15887	0.25179	132.58727	3.259	4.872
FDAS	FRJS	0.20000	0.31698	132.58727	3.206	5.142

FDAS	FRJS	0.25179	0.39905	132.58727	3.145	6.066
FDAS	FRJS	0.31698	0.50238	132.58727	3.121	4.344
FDAS	FRJS	0.39905	0.63246	132.58727	3.112	3.436
FDAS	FRJS	0.50238	0.79621	132.58727	3.072	2.234
FDAS	FRJS	0.63246	1.00237	132.58727	3.348	2.468
FDAS	FRJS	0.79621	1.26191	132.58727	3.345	2.638
FDAS	FRJS	1.00237	1.58866	132.58727	3.372	1.857
FDAS	FRJS	1.26191	2.00000	132.58727	2.790	2.307
FDAS	FRJS	1.58866	2.51785	132.58727	3.414	2.488
FDAS	FRJS	2.00000	3.16979	132.58727	3.675	1.608
FDAS	FRJS	2.51785	3.99052	132.58727	2.933	1.368
FDAS	FRJS	3.16979	5.02377	132.58727	3.414	1.497
FRAS	JEDS	21.058	40.518	21.720	39.416	135.74760
sta1	sta2	lowpass	highpass	distance	km/sec	SNR
FRAS	JEDS	0.01589	0.02518	135.74760	-	-
FRAS	JEDS	0.02000	0.03170	135.74760	3.199	4.555
FRAS	JEDS	0.02518	0.03991	135.74760	-	-
FRAS	JEDS	0.03170	0.05024	135.74760	3.614	4.428
FRAS	JEDS	0.03991	0.06325	135.74760	3.105	5.528
FRAS	JEDS	0.05024	0.07962	135.74760	3.019	8.443
FRAS	JEDS	0.06325	0.10024	135.74760	3.308	12.547
FRAS	JEDS	0.07962	0.12619	135.74760	3.154	8.260
FRAS	JEDS	0.10024	0.15887	135.74760	3.148	6.926
FRAS	JEDS	0.12619	0.20000	135.74760	4.605	5.008
FRAS	JEDS	0.15887	0.25179	135.74760	4.655	3.276
FRAS	JEDS	0.20000	0.31698	135.74760	2.913	2.114
FRAS	JEDS	0.25179	0.39905	135.74760	2.951	4.914
FRAS	JEDS	0.31698	0.50238	135.74760	2.964	5.175
FRAS	JEDS	0.39905	0.63246	135.74760	2.969	3.083
FRAS	JEDS	0.50238	0.79621	135.74760	-	-
FRAS	JEDS	0.63246	1.00237	135.74760	2.523	2.524
FRAS	JEDS	0.79621	1.26191	135.74760	2.518	3.465
FRAS	JEDS	1.00237	1.58866	135.74760	4.413	3.581
FRAS	JEDS	1.26191	2.00000	135.74760	3.136	2.754
FRAS	JEDS	1.58866	2.51785	135.74760	3.561	3.491
FRAS	JEDS	2.00000	3.16979	135.74760	3.580	3.250
FRAS	JEDS	2.51785	3.99052	135.74760	3.321	2.528
FRAS	JEDS	3.16979	5.02377	135.74760	3.595	2.697
DRBS	ENMS	17.828	42.301	19.071	42.572	141.09013
sta1	sta2	lowpass	highpass	distance	km/sec	SNR
DRBS	ENMS	0.01589	0.02518	141.09013	-	-
DRBS	ENMS	0.02000	0.03170	141.09013	3.428	3.904
DRBS	ENMS	0.02518	0.03991	141.09013	-	-
DRBS	ENMS	0.03170	0.05024	141.09013	3.863	9.521
DRBS	ENMS	0.03991	0.06325	141.09013	2.688	14.311
DRBS	ENMS	0.05024	0.07962	141.09013	2.840	5.272
DRBS	ENMS	0.06325	0.10024	141.09013	3.272	3.756
DRBS	ENMS	0.07962	0.12619	141.09013	-	-
DRBS	ENMS	0.10024	0.15887	141.09013	-	-
DRBS	ENMS	0.12619	0.20000	141.09013	2.453	3.966
DRBS	ENMS	0.15887	0.25179	141.09013	3.135	5.733
DRBS	ENMS	0.20000	0.31698	141.09013	3.141	6.422
DRBS	ENMS	0.25179	0.39905	141.09013	3.172	7.166
DRBS	ENMS	0.31698	0.50238	141.09013	3.183	4.682
DRBS	ENMS	0.39905	0.63246	141.09013	3.195	3.290
DRBS	ENMS	0.50238	0.79621	141.09013	3.124	4.729
DRBS	ENMS	0.63246	1.00237	141.09013	3.078	5.404
DRBS	ENMS	0.79621	1.26191	141.09013	3.083	3.460
DRBS	ENMS	1.00237	1.58866	141.09013	3.089	2.279

DRBS	ENMS	1.26191	2.00000	141.09013	2.110	1.200
DRBS	ENMS	1.58866	2.51785	141.09013	4.059	0.967
DRBS	ENMS	2.00000	3.16979	141.09013	2.378	0.979
DRBS	ENMS	2.51785	3.99052	141.09013	3.826	1.238
DRBS	ENMS	3.16979	5.02377	141.09013	3.838	2.958
BLJS	ENMS	19.957	41.605	19.071	42.572	141.34224
sta1	sta2	lowpass	highpass	distance	km/sec	SNR
BLJS	ENMS	0.01589	0.02518	141.34224	-	-
BLJS	ENMS	0.02000	0.03170	141.34224	-	-
BLJS	ENMS	0.02518	0.03991	141.34224	-	-
BLJS	ENMS	0.03170	0.05024	141.34224	3.012	6.182
BLJS	ENMS	0.03991	0.06325	141.34224	3.227	7.920
BLJS	ENMS	0.05024	0.07962	141.34224	3.015	8.595
BLJS	ENMS	0.06325	0.10024	141.34224	2.959	8.109
BLJS	ENMS	0.07962	0.12619	141.34224	3.337	5.336
BLJS	ENMS	0.10024	0.15887	141.34224	3.372	5.439
BLJS	ENMS	0.12619	0.20000	141.34224	3.290	6.821
BLJS	ENMS	0.15887	0.25179	141.34224	3.305	3.618
BLJS	ENMS	0.20000	0.31698	141.34224	3.236	6.927
BLJS	ENMS	0.25179	0.39905	141.34224	3.224	10.512
BLJS	ENMS	0.31698	0.50238	141.34224	3.195	8.974
BLJS	ENMS	0.39905	0.63246	141.34224	3.189	6.141
BLJS	ENMS	0.50238	0.79621	141.34224	3.138	2.982
BLJS	ENMS	0.63246	1.00237	141.34224	3.113	1.799
BLJS	ENMS	0.79621	1.26191	141.34224	3.100	1.598
BLJS	ENMS	1.00237	1.58866	141.34224	2.870	1.357
BLJS	ENMS	1.26191	2.00000	141.34224	2.354	1.183
BLJS	ENMS	1.58866	2.51785	141.34224	2.370	0.929
BLJS	ENMS	2.00000	3.16979	141.34224	2.110	0.995
BLJS	ENMS	2.51785	3.99052	141.34224	2.761	1.585
BLJS	ENMS	3.16979	5.02377	141.34224	4.202	3.068
BDAS	TBKS	28.430	35.100	28.229	36.550	143.70564
sta1	sta2	lowpass	highpass	distance	km/sec	SNR
BDAS	TBKS	0.01589	0.02518	143.70564	3.405	4.044
BDAS	TBKS	0.02000	0.03170	143.70564	3.719	9.599
BDAS	TBKS	0.02518	0.03991	143.70564	3.696	29.185
BDAS	TBKS	0.03170	0.05024	143.70564	3.248	18.364
BDAS	TBKS	0.03991	0.06325	143.70564	3.171	14.187
BDAS	TBKS	0.05024	0.07962	143.70564	2.921	25.494
BDAS	TBKS	0.06325	0.10024	143.70564	2.977	11.067
BDAS	TBKS	0.07962	0.12619	143.70564	3.127	6.133
BDAS	TBKS	0.10024	0.15887	143.70564	3.127	7.110
BDAS	TBKS	0.12619	0.20000	143.70564	2.640	8.368
BDAS	TBKS	0.15887	0.25179	143.70564	2.525	5.512
BDAS	TBKS	0.20000	0.31698	143.70564	2.466	4.270
BDAS	TBKS	0.25179	0.39905	143.70564	2.822	3.205
BDAS	TBKS	0.31698	0.50238	143.70564	2.699	3.336
BDAS	TBKS	0.39905	0.63246	143.70564	2.622	4.203
BDAS	TBKS	0.50238	0.79621	143.70564	2.466	3.322
BDAS	TBKS	0.63246	1.00237	143.70564	2.432	2.394
BDAS	TBKS	0.79621	1.26191	143.70564	2.000	2.256
BDAS	TBKS	1.00237	1.58866	143.70564	3.536	2.297
BDAS	TBKS	1.26191	2.00000	143.70564	3.481	1.882
BDAS	TBKS	1.58866	2.51785	143.70564	2.454	1.476
BDAS	TBKS	2.00000	3.16979	143.70564	3.428	1.831
BDAS	TBKS	2.51785	3.99052	143.70564	4.355	5.333
BDAS	TBKS	3.16979	5.02377	143.70564	4.125	4.664
DRBS	NAMS	17.828	42.301	19.170	42.202	149.59866

sta1	sta2	lowpass	highpass	distance	km/sec	SNR
DRBS	NAMS	0.01589	0.02518	149.59866	3.221	7.241
DRBS	NAMS	0.02000	0.03170	149.59866	3.572	4.824
DRBS	NAMS	0.02518	0.03991	149.59866	-	-
DRBS	NAMS	0.03170	0.05024	149.59866	3.528	2.286
DRBS	NAMS	0.03991	0.06325	149.59866	3.230	3.042
DRBS	NAMS	0.05024	0.07962	149.59866	3.896	8.568
DRBS	NAMS	0.06325	0.10024	149.59866	3.703	11.134
DRBS	NAMS	0.07962	0.12619	149.59866	3.175	6.098
DRBS	NAMS	0.10024	0.15887	149.59866	3.061	2.696
DRBS	NAMS	0.12619	0.20000	149.59866	2.059	2.733
DRBS	NAMS	0.15887	0.25179	149.59866	3.394	3.640
DRBS	NAMS	0.20000	0.31698	149.59866	3.304	3.513
DRBS	NAMS	0.25179	0.39905	149.59866	3.210	3.829
DRBS	NAMS	0.31698	0.50238	149.59866	3.156	3.466
DRBS	NAMS	0.39905	0.63246	149.59866	3.148	3.240
DRBS	NAMS	0.50238	0.79621	149.59866	3.175	2.030
DRBS	NAMS	0.63246	1.00237	149.59866	2.565	2.037
DRBS	NAMS	0.79621	1.26191	149.59866	2.708	1.975
DRBS	NAMS	1.00237	1.58866	149.59866	3.958	1.590
DRBS	NAMS	1.26191	2.00000	149.59866	4.101	1.417
DRBS	NAMS	1.58866	2.51785	149.59866	4.110	1.177
DRBS	NAMS	2.00000	3.16979	149.59866	3.499	1.489
DRBS	NAMS	2.51785	3.99052	149.59866	3.502	1.682
DRBS	NAMS	3.16979	5.02377	149.59866	4.240	2.557
KBRS	LNYS	25.789	39.264	25.081	37.944	154.15781
sta1	sta2	lowpass	highpass	distance	km/sec	SNR
KBRS	LNYS	0.01589	0.02518	154.15781	3.214	2.939
KBRS	LNYS	0.02000	0.03170	154.15781	3.808	2.853
KBRS	LNYS	0.02518	0.03991	154.15781	-	-
KBRS	LNYS	0.03170	0.05024	154.15781	3.481	2.087
KBRS	LNYS	0.03991	0.06325	154.15781	3.030	1.861
KBRS	LNYS	0.05024	0.07962	154.15781	3.905	5.834
KBRS	LNYS	0.06325	0.10024	154.15781	3.133	4.534
KBRS	LNYS	0.07962	0.12619	154.15781	3.056	4.656
KBRS	LNYS	0.10024	0.15887	154.15781	3.002	6.563
KBRS	LNYS	0.12619	0.20000	154.15781	3.006	5.109
KBRS	LNYS	0.15887	0.25179	154.15781	3.073	3.800
KBRS	LNYS	0.20000	0.31698	154.15781	3.054	7.198
KBRS	LNYS	0.25179	0.39905	154.15781	2.983	10.362
KBRS	LNYS	0.31698	0.50238	154.15781	2.940	8.323
KBRS	LNYS	0.39905	0.63246	154.15781	2.917	6.425
KBRS	LNYS	0.50238	0.79621	154.15781	2.935	3.294
KBRS	LNYS	0.63246	1.00237	154.15781	3.337	2.442
KBRS	LNYS	0.79621	1.26191	154.15781	3.314	2.264
KBRS	LNYS	1.00237	1.58866	154.15781	3.351	1.682
KBRS	LNYS	1.26191	2.00000	154.15781	3.118	1.373
KBRS	LNYS	1.58866	2.51785	154.15781	2.965	1.363
KBRS	LNYS	2.00000	3.16979	154.15781	2.618	1.444
KBRS	LNYS	2.51785	3.99052	154.15781	2.608	1.318
KBRS	LNYS	3.16979	5.02377	154.15781	3.182	1.458
BIDS	TBKS	26.867	36.958	28.229	36.550	156.70729
sta1	sta2	lowpass	highpass	distance	km/sec	SNR
BIDS	TBKS	0.01589	0.02518	156.70729	3.614	5.044
BIDS	TBKS	0.02000	0.03170	156.70729	-	-
BIDS	TBKS	0.02518	0.03991	156.70729	3.351	12.267
BIDS	TBKS	0.03170	0.05024	156.70729	3.109	28.350
BIDS	TBKS	0.03991	0.06325	156.70729	3.085	18.969
BIDS	TBKS	0.05024	0.07962	156.70729	3.085	24.200

BIDS	TBKS	0.06325	0.10024	156.70729	2.991	12.131
BIDS	TBKS	0.07962	0.12619	156.70729	2.893	10.599
BIDS	TBKS	0.10024	0.15887	156.70729	3.267	16.545
BIDS	TBKS	0.12619	0.20000	156.70729	3.675	14.100
BIDS	TBKS	0.15887	0.25179	156.70729	2.715	9.662
BIDS	TBKS	0.20000	0.31698	156.70729	2.680	14.547
BIDS	TBKS	0.25179	0.39905	156.70729	2.610	16.516
BIDS	TBKS	0.31698	0.50238	156.70729	2.499	10.676
BIDS	TBKS	0.39905	0.63246	156.70729	2.350	4.545
BIDS	TBKS	0.50238	0.79621	156.70729	2.347	1.902
BIDS	TBKS	0.63246	1.00237	156.70729	3.175	1.715
BIDS	TBKS	0.79621	1.26191	156.70729	3.216	1.468
BIDS	TBKS	1.00237	1.58866	156.70729	2.841	1.452
BIDS	TBKS	1.26191	2.00000	156.70729	2.561	1.311
BIDS	TBKS	1.58866	2.51785	156.70729	3.728	1.238
BIDS	TBKS	2.00000	3.16979	156.70729	3.735	1.950
BIDS	TBKS	2.51785	3.99052	156.70729	4.477	5.715
BIDS	TBKS	3.16979	5.02377	156.70729	4.477	4.832
AFFS	ARSS	24.555	42.482	25.827	43.154	156.76732
sta1	sta2	lowpass	highpass	distance	km/sec	SNR
AFFS	ARSS	0.01589	0.02518	156.76732	3.244	1.068
AFFS	ARSS	0.02000	0.03170	156.76732	-	-
AFFS	ARSS	0.02518	0.03991	156.76732	-	-
AFFS	ARSS	0.03170	0.05024	156.76732	2.477	6.006
AFFS	ARSS	0.03991	0.06325	156.76732	3.244	6.436
AFFS	ARSS	0.05024	0.07962	156.76732	3.040	4.202
AFFS	ARSS	0.06325	0.10024	156.76732	3.050	4.384
AFFS	ARSS	0.07962	0.12619	156.76732	3.234	7.942
AFFS	ARSS	0.10024	0.15887	156.76732	3.266	6.521
AFFS	ARSS	0.12619	0.20000	156.76732	3.277	3.040
AFFS	ARSS	0.15887	0.25179	156.76732	3.158	4.420
AFFS	ARSS	0.20000	0.31698	156.76732	3.161	13.375
AFFS	ARSS	0.25179	0.39905	156.76732	3.161	14.312
AFFS	ARSS	0.31698	0.50238	156.76732	3.103	9.881
AFFS	ARSS	0.39905	0.63246	156.76732	3.067	7.266
AFFS	ARSS	0.50238	0.79621	156.76732	3.052	4.424
AFFS	ARSS	0.63246	1.00237	156.76732	3.012	2.423
AFFS	ARSS	0.79621	1.26191	156.76732	2.895	2.764
AFFS	ARSS	1.00237	1.58866	156.76732	2.897	2.388
AFFS	ARSS	1.26191	2.00000	156.76732	2.920	2.092
AFFS	ARSS	1.58866	2.51785	156.76732	3.857	1.905
AFFS	ARSS	2.00000	3.16979	156.76732	3.865	1.638
AFFS	ARSS	2.51785	3.99052	156.76732	3.880	2.372
AFFS	ARSS	3.16979	5.02377	156.76732	3.086	2.709
BLJS	FRAS	19.957	41.605	21.058	40.518	166.76157
sta1	sta2	lowpass	highpass	distance	km/sec	SNR
BLJS	FRAS	0.01589	0.02518	166.76157	-	-
BLJS	FRAS	0.02000	0.03170	166.76157	-	-
BLJS	FRAS	0.02518	0.03991	166.76157	-	-
BLJS	FRAS	0.03170	0.05024	166.76157	2.447	3.421
BLJS	FRAS	0.03991	0.06325	166.76157	2.214	5.265
BLJS	FRAS	0.05024	0.07962	166.76157	2.124	3.125
BLJS	FRAS	0.06325	0.10024	166.76157	3.506	3.534
BLJS	FRAS	0.07962	0.12619	166.76157	3.257	8.847
BLJS	FRAS	0.10024	0.15887	166.76157	3.232	8.961
BLJS	FRAS	0.12619	0.20000	166.76157	3.262	6.120
BLJS	FRAS	0.15887	0.25179	166.76157	3.262	5.638
BLJS	FRAS	0.20000	0.31698	166.76157	3.296	5.573
BLJS	FRAS	0.25179	0.39905	166.76157	3.200	6.579

BLJS	FRAS	0.31698	0.50238	166.76157	3.102	6.183
BLJS	FRAS	0.39905	0.63246	166.76157	3.061	2.824
BLJS	FRAS	0.50238	0.79621	166.76157	3.982	1.832
BLJS	FRAS	0.63246	1.00237	166.76157	4.695	1.828
BLJS	FRAS	0.79621	1.26191	166.76157	4.016	2.004
BLJS	FRAS	1.00237	1.58866	166.76157	4.005	1.810
BLJS	FRAS	1.26191	2.00000	166.76157	2.661	1.299
BLJS	FRAS	1.58866	2.51785	166.76157	2.667	1.256
BLJS	FRAS	2.00000	3.16979	166.76157	3.070	1.348
BLJS	FRAS	2.51785	3.99052	166.76157	4.402	1.721
BLJS	FRAS	3.16979	5.02377	166.76157	4.152	3.450
TBKS	WJHS	28.229	36.550	26.732	36.393	167.20091
sta1	sta2	lowpass	highpass	distance	km/sec	SNR
TBKS	WJHS	0.01589	0.02518	167.20091	3.133	1.471
TBKS	WJHS	0.02000	0.03170	167.20091	2.873	2.078
TBKS	WJHS	0.02518	0.03991	167.20091	3.466	8.378
TBKS	WJHS	0.03170	0.05024	167.20091	3.230	10.021
TBKS	WJHS	0.03991	0.06325	167.20091	2.933	17.475
TBKS	WJHS	0.05024	0.07962	167.20091	2.948	30.259
TBKS	WJHS	0.06325	0.10024	167.20091	2.940	21.169
TBKS	WJHS	0.07962	0.12619	167.20091	3.085	24.661
TBKS	WJHS	0.10024	0.15887	167.20091	3.136	16.675
TBKS	WJHS	0.12619	0.20000	167.20091	3.921	8.066
TBKS	WJHS	0.15887	0.25179	167.20091	3.966	8.579
TBKS	WJHS	0.20000	0.31698	167.20091	3.328	5.839
TBKS	WJHS	0.25179	0.39905	167.20091	3.307	3.083
TBKS	WJHS	0.31698	0.50238	167.20091	2.394	1.723
TBKS	WJHS	0.39905	0.63246	167.20091	2.346	2.361
TBKS	WJHS	0.50238	0.79621	167.20091	3.914	2.247
TBKS	WJHS	0.63246	1.00237	167.20091	3.203	1.735
TBKS	WJHS	0.79621	1.26191	167.20091	3.176	1.789
TBKS	WJHS	1.00237	1.58866	167.20091	2.351	1.776
TBKS	WJHS	1.26191	2.00000	167.20091	2.739	1.305
TBKS	WJHS	1.58866	2.51785	167.20091	2.728	1.184
TBKS	WJHS	2.00000	3.16979	167.20091	4.665	1.746
TBKS	WJHS	2.51785	3.99052	167.20091	4.227	4.931
TBKS	WJHS	3.16979	5.02377	167.20091	4.209	4.674
KBRS	YOBS	25.789	39.264	24.358	38.743	167.56093
sta1	sta2	lowpass	highpass	distance	km/sec	SNR
KBRS	YOBS	0.01589	0.02518	167.56093	3.627	1.974
KBRS	YOBS	0.02000	0.03170	167.56093	-	-
KBRS	YOBS	0.02518	0.03991	167.56093	-	-
KBRS	YOBS	0.03170	0.05024	167.56093	3.133	10.993
KBRS	YOBS	0.03991	0.06325	167.56093	2.927	14.551
KBRS	YOBS	0.05024	0.07962	167.56093	3.058	20.296
KBRS	YOBS	0.06325	0.10024	167.56093	3.124	8.295
KBRS	YOBS	0.07962	0.12619	167.56093	3.186	7.557
KBRS	YOBS	0.10024	0.15887	167.56093	3.225	6.308
KBRS	YOBS	0.12619	0.20000	167.56093	3.176	3.853
KBRS	YOBS	0.15887	0.25179	167.56093	2.665	2.430
KBRS	YOBS	0.20000	0.31698	167.56093	2.990	3.863
KBRS	YOBS	0.25179	0.39905	167.56093	3.001	4.536
KBRS	YOBS	0.31698	0.50238	167.56093	2.999	4.414
KBRS	YOBS	0.39905	0.63246	167.56093	2.984	2.560
KBRS	YOBS	0.50238	0.79621	167.56093	4.032	2.013
KBRS	YOBS	0.63246	1.00237	167.56093	2.965	1.521
KBRS	YOBS	0.79621	1.26191	167.56093	3.559	1.565
KBRS	YOBS	1.00237	1.58866	167.56093	3.456	1.645
KBRS	YOBS	1.26191	2.00000	167.56093	3.479	1.528

KBRS	YOBS	1.58866	2.51785	167.56093	3.395	1.684
KBRS	YOBS	2.00000	3.16979	167.56093	2.944	1.877
KBRS	YOBS	2.51785	3.99052	167.56093	3.544	1.785
KBRS	YOBS	3.16979	5.02377	167.56093	3.544	1.562
RSHS	TBKS	28.300	34.797	28.229	36.550	171.92442
sta1	sta2	lowpass	highpass	distance	km/sec	SNR
RSHS	TBKS	0.01589	0.02518	171.92442	3.689	2.064
RSHS	TBKS	0.02000	0.03170	171.92442	-	-
RSHS	TBKS	0.02518	0.03991	171.92442	3.289	4.699
RSHS	TBKS	0.03170	0.05024	171.92442	3.301	10.267
RSHS	TBKS	0.03991	0.06325	171.92442	3.038	33.786
RSHS	TBKS	0.05024	0.07962	171.92442	2.960	29.451
RSHS	TBKS	0.06325	0.10024	171.92442	3.167	23.019
RSHS	TBKS	0.07962	0.12619	171.92442	3.020	11.445
RSHS	TBKS	0.10024	0.15887	171.92442	3.121	8.805
RSHS	TBKS	0.12619	0.20000	171.92442	3.149	10.050
RSHS	TBKS	0.15887	0.25179	171.92442	3.210	5.891
RSHS	TBKS	0.20000	0.31698	171.92442	2.153	5.652
RSHS	TBKS	0.25179	0.39905	171.92442	2.516	5.634
RSHS	TBKS	0.31698	0.50238	171.92442	2.580	4.696
RSHS	TBKS	0.39905	0.63246	171.92442	2.183	3.988
RSHS	TBKS	0.50238	0.79621	171.92442	2.162	2.041
RSHS	TBKS	0.63246	1.00237	171.92442	3.398	1.143
RSHS	TBKS	0.79621	1.26191	171.92442	3.683	1.511
RSHS	TBKS	1.00237	1.58866	171.92442	3.686	1.721
RSHS	TBKS	1.26191	2.00000	171.92442	-	-
RSHS	TBKS	1.58866	2.51785	171.92442	-	-
RSHS	TBKS	2.00000	3.16979	171.92442	4.043	1.859
RSHS	TBKS	2.51785	3.99052	171.92442	4.040	5.207
RSHS	TBKS	3.16979	5.02377	171.92442	4.399	4.056
UMJS	YOBS	25.232	37.311	24.358	38.743	174.25420
sta1	sta2	lowpass	highpass	distance	km/sec	SNR
UMJS	YOBS	0.01589	0.02518	174.25420	3.714	8.177
UMJS	YOBS	0.02000	0.03170	174.25420	-	-
UMJS	YOBS	0.02518	0.03991	174.25420	-	-
UMJS	YOBS	0.03170	0.05024	174.25420	2.932	4.469
UMJS	YOBS	0.03991	0.06325	174.25420	3.182	5.337
UMJS	YOBS	0.05024	0.07962	174.25420	3.256	6.421
UMJS	YOBS	0.06325	0.10024	174.25420	3.194	8.130
UMJS	YOBS	0.07962	0.12619	174.25420	3.057	7.875
UMJS	YOBS	0.10024	0.15887	174.25420	3.308	9.091
UMJS	YOBS	0.12619	0.20000	174.25420	3.377	5.881
UMJS	YOBS	0.15887	0.25179	174.25420	2.275	3.192
UMJS	YOBS	0.20000	0.31698	174.25420	3.114	2.193
UMJS	YOBS	0.25179	0.39905	174.25420	3.061	2.266
UMJS	YOBS	0.31698	0.50238	174.25420	3.053	2.995
UMJS	YOBS	0.39905	0.63246	174.25420	3.015	2.703
UMJS	YOBS	0.50238	0.79621	174.25420	2.851	2.366
UMJS	YOBS	0.63246	1.00237	174.25420	3.577	1.629
UMJS	YOBS	0.79621	1.26191	174.25420	3.545	1.465
UMJS	YOBS	1.00237	1.58866	174.25420	3.460	1.472
UMJS	YOBS	1.26191	2.00000	174.25420	3.460	1.394
UMJS	YOBS	1.58866	2.51785	174.25420	2.475	1.376
UMJS	YOBS	2.00000	3.16979	174.25420	3.070	3.201
UMJS	YOBS	2.51785	3.99052	174.25420	4.263	3.066
UMJS	YOBS	3.16979	5.02377	174.25420	4.595	1.640
FRJS	SHBS	22.591	39.364	21.005	39.683	179.39232
sta1	sta2	lowpass	highpass	distance	km/sec	SNR

FRJS	SHBS	0.01589	0.02518	179.39232	3.740	2.401
FRJS	SHBS	0.02000	0.03170	179.39232	-	-
FRJS	SHBS	0.02518	0.03991	179.39232	-	-
FRJS	SHBS	0.03170	0.05024	179.39232	3.661	7.600
FRJS	SHBS	0.03991	0.06325	179.39232	3.823	4.817
FRJS	SHBS	0.05024	0.07962	179.39232	3.026	6.344
FRJS	SHBS	0.06325	0.10024	179.39232	2.974	6.928
FRJS	SHBS	0.07962	0.12619	179.39232	2.996	7.578
FRJS	SHBS	0.10024	0.15887	179.39232	2.762	7.482
FRJS	SHBS	0.12619	0.20000	179.39232	3.469	5.417
FRJS	SHBS	0.15887	0.25179	179.39232	3.000	5.369
FRJS	SHBS	0.20000	0.31698	179.39232	3.008	5.511
FRJS	SHBS	0.25179	0.39905	179.39232	2.964	4.922
FRJS	SHBS	0.31698	0.50238	179.39232	2.918	2.565
FRJS	SHBS	0.39905	0.63246	179.39232	2.897	2.392
FRJS	SHBS	0.50238	0.79621	179.39232	2.924	1.829
FRJS	SHBS	0.63246	1.00237	179.39232	2.736	1.271
FRJS	SHBS	0.79621	1.26191	179.39232	2.016	1.239
FRJS	SHBS	1.00237	1.58866	179.39232	2.725	1.478
FRJS	SHBS	1.26191	2.00000	179.39232	4.696	1.467
FRJS	SHBS	1.58866	2.51785	179.39232	3.557	1.624
FRJS	SHBS	2.00000	3.16979	179.39232	2.860	1.316
FRJS	SHBS	2.51785	3.99052	179.39232	4.786	1.333
FRJS	SHBS	3.16979	5.02377	179.39232	4.681	1.453
FRJS	LBNS	22.591	39.364	21.047	39.902	180.41600
sta1	sta2	lowpass	highpass	distance	km/sec	SNR
FRJS	LBNS	0.01589	0.02518	180.41600	3.307	1.387
FRJS	LBNS	0.02000	0.03170	180.41600	3.368	1.003
FRJS	LBNS	0.02518	0.03991	180.41600	4.324	1.257
FRJS	LBNS	0.03170	0.05024	180.41600	-	-
FRJS	LBNS	0.03991	0.06325	180.41600	3.321	6.096
FRJS	LBNS	0.05024	0.07962	180.41600	3.050	9.361
FRJS	LBNS	0.06325	0.10024	180.41600	3.087	7.201
FRJS	LBNS	0.07962	0.12619	180.41600	3.190	9.990
FRJS	LBNS	0.10024	0.15887	180.41600	3.348	8.856
FRJS	LBNS	0.12619	0.20000	180.41600	3.386	6.317
FRJS	LBNS	0.15887	0.25179	180.41600	3.206	7.594
FRJS	LBNS	0.20000	0.31698	180.41600	3.174	3.969
FRJS	LBNS	0.25179	0.39905	180.41600	3.094	4.403
FRJS	LBNS	0.31698	0.50238	180.41600	3.037	3.258
FRJS	LBNS	0.39905	0.63246	180.41600	3.013	2.792
FRJS	LBNS	0.50238	0.79621	180.41600	2.989	2.074
FRJS	LBNS	0.63246	1.00237	180.41600	2.779	1.613
FRJS	LBNS	0.79621	1.26191	180.41600	2.717	1.358
FRJS	LBNS	1.00237	1.58866	180.41600	3.276	1.406
FRJS	LBNS	1.26191	2.00000	180.41600	2.652	1.395
FRJS	LBNS	1.58866	2.51785	180.41600	3.456	1.411
FRJS	LBNS	2.00000	3.16979	180.41600	-	-
FRJS	LBNS	2.51785	3.99052	180.41600	4.483	1.498
FRJS	LBNS	3.16979	5.02377	180.41600	4.728	1.493
HAQS	TBKS	29.050	34.920	28.229	36.550	183.42645
sta1	sta2	lowpass	highpass	distance	km/sec	SNR
HAQS	TBKS	0.01589	0.02518	183.42645	3.809	16.033
HAQS	TBKS	0.02000	0.03170	183.42645	3.692	12.628
HAQS	TBKS	0.02518	0.03991	183.42645	3.255	6.487
HAQS	TBKS	0.03170	0.05024	183.42645	3.364	12.177
HAQS	TBKS	0.03991	0.06325	183.42645	3.061	20.250
HAQS	TBKS	0.05024	0.07962	183.42645	3.023	24.401
HAQS	TBKS	0.06325	0.10024	183.42645	2.964	22.275

HAQS	TBKS	0.07962	0.12619	183.42645	3.086	9.349
HAQS	TBKS	0.10024	0.15887	183.42645	3.124	5.466
HAQS	TBKS	0.12619	0.20000	183.42645	2.989	9.589
HAQS	TBKS	0.15887	0.25179	183.42645	2.776	7.931
HAQS	TBKS	0.20000	0.31698	183.42645	2.457	6.591
HAQS	TBKS	0.25179	0.39905	183.42645	2.604	3.189
HAQS	TBKS	0.31698	0.50238	183.42645	2.614	2.641
HAQS	TBKS	0.39905	0.63246	183.42645	2.514	3.968
HAQS	TBKS	0.50238	0.79621	183.42645	2.451	2.739
HAQS	TBKS	0.63246	1.00237	183.42645	2.838	1.565
HAQS	TBKS	0.79621	1.26191	183.42645	2.154	1.680
HAQS	TBKS	1.00237	1.58866	183.42645	2.160	1.774
HAQS	TBKS	1.26191	2.00000	183.42645	4.351	1.721
HAQS	TBKS	1.58866	2.51785	183.42645	3.086	1.626
HAQS	TBKS	2.00000	3.16979	183.42645	3.571	1.763
HAQS	TBKS	2.51785	3.99052	183.42645	3.574	3.343
HAQS	TBKS	3.16979	5.02377	183.42645	3.241	2.990
DJNS	ENMS	17.701	43.545	19.071	42.572	183.65048
sta1	sta2	lowpass	highpass	distance	km/sec	SNR
DJNS	ENMS	0.01589	0.02518	183.65048	3.351	4.868
DJNS	ENMS	0.02000	0.03170	183.65048	-	-
DJNS	ENMS	0.02518	0.03991	183.65048	3.884	3.535
DJNS	ENMS	0.03170	0.05024	183.65048	3.462	8.035
DJNS	ENMS	0.03991	0.06325	183.65048	2.976	3.898
DJNS	ENMS	0.05024	0.07962	183.65048	2.911	4.983
DJNS	ENMS	0.06325	0.10024	183.65048	3.211	4.375
DJNS	ENMS	0.07962	0.12619	183.65048	3.247	4.729
DJNS	ENMS	0.10024	0.15887	183.65048	3.186	6.152
DJNS	ENMS	0.12619	0.20000	183.65048	3.247	4.775
DJNS	ENMS	0.15887	0.25179	183.65048	3.294	5.191
DJNS	ENMS	0.20000	0.31698	183.65048	3.308	5.217
DJNS	ENMS	0.25179	0.39905	183.65048	3.279	6.234
DJNS	ENMS	0.31698	0.50238	183.65048	3.195	5.044
DJNS	ENMS	0.39905	0.63246	183.65048	3.156	4.205
DJNS	ENMS	0.50238	0.79621	183.65048	3.134	4.155
DJNS	ENMS	0.63246	1.00237	183.65048	3.102	3.162
DJNS	ENMS	0.79621	1.26191	183.65048	3.075	2.972
DJNS	ENMS	1.00237	1.58866	183.65048	3.047	2.522
DJNS	ENMS	1.26191	2.00000	183.65048	3.041	2.018
DJNS	ENMS	1.58866	2.51785	183.65048	4.056	1.534
DJNS	ENMS	2.00000	3.16979	183.65048	2.926	1.452
DJNS	ENMS	2.51785	3.99052	183.65048	3.739	1.598
DJNS	ENMS	3.16979	5.02377	183.65048	3.842	3.730
BIDS	UMJS	26.867	36.958	25.232	37.311	185.15718
sta1	sta2	lowpass	highpass	distance	km/sec	SNR
BIDS	UMJS	0.01589	0.02518	185.15718	3.158	0.657
BIDS	UMJS	0.02000	0.03170	185.15718	-	-
BIDS	UMJS	0.02518	0.03991	185.15718	3.611	1.823
BIDS	UMJS	0.03170	0.05024	185.15718	3.577	4.537
BIDS	UMJS	0.03991	0.06325	185.15718	3.155	6.293
BIDS	UMJS	0.05024	0.07962	185.15718	3.208	11.368
BIDS	UMJS	0.06325	0.10024	185.15718	4.498	12.353
BIDS	UMJS	0.07962	0.12619	185.15718	3.045	6.222
BIDS	UMJS	0.10024	0.15887	185.15718	3.276	7.205
BIDS	UMJS	0.12619	0.20000	185.15718	3.342	10.718
BIDS	UMJS	0.15887	0.25179	185.15718	3.212	9.747
BIDS	UMJS	0.20000	0.31698	185.15718	3.186	4.957
BIDS	UMJS	0.25179	0.39905	185.15718	3.158	4.434
BIDS	UMJS	0.31698	0.50238	185.15718	3.528	2.739

BIDS	UMJS	0.39905	0.63246	185.15718	3.473	2.459
BIDS	UMJS	0.50238	0.79621	185.15718	4.601	2.111
BIDS	UMJS	0.63246	1.00237	185.15718	3.674	1.997
BIDS	UMJS	0.79621	1.26191	185.15718	2.990	1.693
BIDS	UMJS	1.00237	1.58866	185.15718	4.159	1.555
BIDS	UMJS	1.26191	2.00000	185.15718	4.140	1.591
BIDS	UMJS	1.58866	2.51785	185.15718	2.180	1.640
BIDS	UMJS	2.00000	3.16979	185.15718	3.586	1.636
BIDS	UMJS	2.51785	3.99052	185.15718	3.588	1.936
BIDS	UMJS	3.16979	5.02377	185.15718	3.591	1.955
DJNS	FRSS	17.701	43.545	16.739	42.115	185.83177
sta1	sta2	lowpass	highpass	distance	km/sec	SNR
DJNS	FRSS	0.01589	0.02518	185.83177	3.878	5.456
DJNS	FRSS	0.02000	0.03170	185.83177	-	-
DJNS	FRSS	0.02518	0.03991	185.83177	3.017	1.921
DJNS	FRSS	0.03170	0.05024	185.83177	3.610	6.676
DJNS	FRSS	0.03991	0.06325	185.83177	3.297	6.723
DJNS	FRSS	0.05024	0.07962	185.83177	3.091	7.501
DJNS	FRSS	0.06325	0.10024	185.83177	2.840	11.176
DJNS	FRSS	0.07962	0.12619	185.83177	2.770	11.184
DJNS	FRSS	0.10024	0.15887	185.83177	2.751	10.034
DJNS	FRSS	0.12619	0.20000	185.83177	2.078	6.876
DJNS	FRSS	0.15887	0.25179	185.83177	2.038	3.986
DJNS	FRSS	0.20000	0.31698	185.83177	3.054	3.365
DJNS	FRSS	0.25179	0.39905	185.83177	2.003	3.642
DJNS	FRSS	0.31698	0.50238	185.83177	2.063	2.534
DJNS	FRSS	0.39905	0.63246	185.83177	3.156	2.236
DJNS	FRSS	0.50238	0.79621	185.83177	-	-
DJNS	FRSS	0.63246	1.00237	185.83177	3.446	1.666
DJNS	FRSS	0.79621	1.26191	185.83177	3.318	1.633
DJNS	FRSS	1.00237	1.58866	185.83177	3.023	1.265
DJNS	FRSS	1.26191	2.00000	185.83177	2.999	1.070
DJNS	FRSS	1.58866	2.51785	185.83177	2.861	1.070
DJNS	FRSS	2.00000	3.16979	185.83177	2.861	1.139
DJNS	FRSS	2.51785	3.99052	185.83177	2.995	1.124
DJNS	FRSS	3.16979	5.02377	185.83177	2.037	1.110
UMJS	WJHS	25.232	37.311	26.732	36.393	190.31262
sta1	sta2	lowpass	highpass	distance	km/sec	SNR
UMJS	WJHS	0.01589	0.02518	190.31262	3.846	3.241
UMJS	WJHS	0.02000	0.03170	190.31262	-	-
UMJS	WJHS	0.02518	0.03991	190.31262	4.053	1.761
UMJS	WJHS	0.03170	0.05024	190.31262	2.917	3.620
UMJS	WJHS	0.03991	0.06325	190.31262	2.933	6.451
UMJS	WJHS	0.05024	0.07962	190.31262	2.948	10.431
UMJS	WJHS	0.06325	0.10024	190.31262	2.908	8.958
UMJS	WJHS	0.07962	0.12619	190.31262	2.963	8.517
UMJS	WJHS	0.10024	0.15887	190.31262	2.974	7.333
UMJS	WJHS	0.12619	0.20000	190.31262	4.772	8.350
UMJS	WJHS	0.15887	0.25179	190.31262	4.772	5.279
UMJS	WJHS	0.20000	0.31698	190.31262	2.287	2.834
UMJS	WJHS	0.25179	0.39905	190.31262	3.991	2.144
UMJS	WJHS	0.31698	0.50238	190.31262	4.049	1.643
UMJS	WJHS	0.39905	0.63246	190.31262	2.765	1.335
UMJS	WJHS	0.50238	0.79621	190.31262	2.757	1.382
UMJS	WJHS	0.63246	1.00237	190.31262	2.012	1.211
UMJS	WJHS	0.79621	1.26191	190.31262	4.506	1.134
UMJS	WJHS	1.00237	1.58866	190.31262	2.088	1.226
UMJS	WJHS	1.26191	2.00000	190.31262	4.263	1.479
UMJS	WJHS	1.58866	2.51785	190.31262	2.536	1.285

UMJS	WJHS	2.00000	3.16979	190.31262	2.536	1.196
UMJS	WJHS	2.51785	3.99052	190.31262	2.953	1.407
UMJS	WJHS	3.16979	5.02377	190.31262	2.948	1.627
JLOS	QLBS	28.735	35.492	28.652	37.594	205.29692
sta1	sta2	lowpass	highpass	distance	km/sec	SNR
JLOS	QLBS	0.01589	0.02518	205.29692	2.507	1.600
JLOS	QLBS	0.02000	0.03170	205.29692	2.226	0.872
JLOS	QLBS	0.02518	0.03991	205.29692	3.473	1.611
JLOS	QLBS	0.03170	0.05024	205.29692	3.176	4.036
JLOS	QLBS	0.03991	0.06325	205.29692	3.032	4.933
JLOS	QLBS	0.05024	0.07962	205.29692	2.919	5.452
JLOS	QLBS	0.06325	0.10024	205.29692	2.977	8.043
JLOS	QLBS	0.07962	0.12619	205.29692	2.970	11.875
JLOS	QLBS	0.10024	0.15887	205.29692	2.933	6.490
JLOS	QLBS	0.12619	0.20000	205.29692	2.880	4.330
JLOS	QLBS	0.15887	0.25179	205.29692	2.746	4.047
JLOS	QLBS	0.20000	0.31698	205.29692	2.657	3.923
JLOS	QLBS	0.25179	0.39905	205.29692	2.487	3.639
JLOS	QLBS	0.31698	0.50238	205.29692	2.331	2.551
JLOS	QLBS	0.39905	0.63246	205.29692	2.207	2.510
JLOS	QLBS	0.50238	0.79621	205.29692	3.461	1.804
JLOS	QLBS	0.63246	1.00237	205.29692	3.442	1.296
JLOS	QLBS	0.79621	1.26191	205.29692	3.470	1.793
JLOS	QLBS	1.00237	1.58866	205.29692	3.141	1.986
JLOS	QLBS	1.26191	2.00000	205.29692	3.296	1.960
JLOS	QLBS	1.58866	2.51785	205.29692	2.792	1.437
JLOS	QLBS	2.00000	3.16979	205.29692	4.653	1.293
JLOS	QLBS	2.51785	3.99052	205.29692	4.696	1.588
JLOS	QLBS	3.16979	5.02377	205.29692	4.709	1.833
KBRS	UMJS	25.789	39.264	25.232	37.311	205.56693
sta1	sta2	lowpass	highpass	distance	km/sec	SNR
KBRS	UMJS	0.01589	0.02518	205.56693	-	-
KBRS	UMJS	0.02000	0.03170	205.56693	-	-
KBRS	UMJS	0.02518	0.03991	205.56693	4.385	1.598
KBRS	UMJS	0.03170	0.05024	205.56693	3.159	2.401
KBRS	UMJS	0.03991	0.06325	205.56693	3.128	11.047
KBRS	UMJS	0.05024	0.07962	205.56693	3.118	18.556
KBRS	UMJS	0.06325	0.10024	205.56693	3.077	14.655
KBRS	UMJS	0.07962	0.12619	205.56693	3.065	7.052
KBRS	UMJS	0.10024	0.15887	205.56693	3.172	8.095
KBRS	UMJS	0.12619	0.20000	205.56693	3.143	7.807
KBRS	UMJS	0.15887	0.25179	205.56693	3.090	4.613
KBRS	UMJS	0.20000	0.31698	205.56693	3.076	3.326
KBRS	UMJS	0.25179	0.39905	205.56693	2.948	2.458
KBRS	UMJS	0.31698	0.50238	205.56693	2.887	2.370
KBRS	UMJS	0.39905	0.63246	205.56693	2.847	2.741
KBRS	UMJS	0.50238	0.79621	205.56693	2.850	2.594
KBRS	UMJS	0.63246	1.00237	205.56693	3.530	1.639
KBRS	UMJS	0.79621	1.26191	205.56693	4.265	1.429
KBRS	UMJS	1.00237	1.58866	205.56693	2.209	1.393
KBRS	UMJS	1.26191	2.00000	205.56693	3.145	1.223
KBRS	UMJS	1.58866	2.51785	205.56693	3.143	1.367
KBRS	UMJS	2.00000	3.16979	205.56693	3.449	1.673
KBRS	UMJS	2.51785	3.99052	205.56693	3.451	1.648
KBRS	UMJS	3.16979	5.02377	205.56693	3.782	1.348
KBRS	YNBS	25.789	39.264	24.340	37.994	205.75529
sta1	sta2	lowpass	highpass	distance	km/sec	SNR
KBRS	YNBS	0.01589	0.02518	205.75529	-	-

KBRS	YNBS	0.02000	0.03170	205.75529	-	-
KBRS	YNBS	0.02518	0.03991	205.75529	3.779	2.022
KBRS	YNBS	0.03170	0.05024	205.75529	3.037	8.681
KBRS	YNBS	0.03991	0.06325	205.75529	3.038	14.161
KBRS	YNBS	0.05024	0.07962	205.75529	3.119	20.602
KBRS	YNBS	0.06325	0.10024	205.75529	3.152	11.580
KBRS	YNBS	0.07962	0.12619	205.75529	3.125	5.749
KBRS	YNBS	0.10024	0.15887	205.75529	3.193	6.995
KBRS	YNBS	0.12619	0.20000	205.75529	3.142	4.433
KBRS	YNBS	0.15887	0.25179	205.75529	3.116	3.882
KBRS	YNBS	0.20000	0.31698	205.75529	3.108	6.441
KBRS	YNBS	0.25179	0.39905	205.75529	3.055	8.125
KBRS	YNBS	0.31698	0.50238	205.75529	2.979	6.413
KBRS	YNBS	0.39905	0.63246	205.75529	2.951	5.558
KBRS	YNBS	0.50238	0.79621	205.75529	2.928	5.308
KBRS	YNBS	0.63246	1.00237	205.75529	2.864	3.525
KBRS	YNBS	0.79621	1.26191	205.75529	3.719	1.894
KBRS	YNBS	1.00237	1.58866	205.75529	2.185	1.673
KBRS	YNBS	1.26191	2.00000	205.75529	4.248	1.380
KBRS	YNBS	1.58866	2.51785	205.75529	4.279	1.187
KBRS	YNBS	2.00000	3.16979	205.75529	3.535	1.393
KBRS	YNBS	2.51785	3.99052	205.75529	3.533	1.568
KBRS	YNBS	3.16979	5.02377	205.75529	2.112	1.448
FRJS	YOBS	22.591	39.364	24.358	38.743	206.40295
sta1	sta2	lowpass	highpass	distance	km/sec	SNR
FRJS	YOBS	0.01589	0.02518	206.40295	-	-
FRJS	YOBS	0.02000	0.03170	206.40295	-	-
FRJS	YOBS	0.02518	0.03991	206.40295	3.951	2.001
FRJS	YOBS	0.03170	0.05024	206.40295	3.868	1.753
FRJS	YOBS	0.03991	0.06325	206.40295	2.865	2.901
FRJS	YOBS	0.05024	0.07962	206.40295	3.127	5.246
FRJS	YOBS	0.06325	0.10024	206.40295	3.143	6.322
FRJS	YOBS	0.07962	0.12619	206.40295	3.227	11.019
FRJS	YOBS	0.10024	0.15887	206.40295	3.304	9.056
FRJS	YOBS	0.12619	0.20000	206.40295	3.239	5.757
FRJS	YOBS	0.15887	0.25179	206.40295	3.201	4.024
FRJS	YOBS	0.20000	0.31698	206.40295	3.150	6.260
FRJS	YOBS	0.25179	0.39905	206.40295	3.114	8.275
FRJS	YOBS	0.31698	0.50238	206.40295	2.940	4.194
FRJS	YOBS	0.39905	0.63246	206.40295	2.957	3.162
FRJS	YOBS	0.50238	0.79621	206.40295	2.997	2.127
FRJS	YOBS	0.63246	1.00237	206.40295	3.016	1.368
FRJS	YOBS	0.79621	1.26191	206.40295	3.314	1.289
FRJS	YOBS	1.00237	1.58866	206.40295	3.551	1.517
FRJS	YOBS	1.26191	2.00000	206.40295	4.704	2.363
FRJS	YOBS	1.58866	2.51785	206.40295	3.839	2.276
FRJS	YOBS	2.00000	3.16979	206.40295	4.522	1.951
FRJS	YOBS	2.51785	3.99052	206.40295	4.721	2.005
FRJS	YOBS	3.16979	5.02377	206.40295	4.670	1.808
FRAS	FRJS	21.058	40.518	22.591	39.364	207.91652
sta1	sta2	lowpass	highpass	distance	km/sec	SNR
FRAS	FRJS	0.01589	0.02518	207.91652	3.505	3.163
FRAS	FRJS	0.02000	0.03170	207.91652	3.500	0.889
FRAS	FRJS	0.02518	0.03991	207.91652	-	-
FRAS	FRJS	0.03170	0.05024	207.91652	3.761	2.441
FRAS	FRJS	0.03991	0.06325	207.91652	3.059	2.396
FRAS	FRJS	0.05024	0.07962	207.91652	3.124	2.571
FRAS	FRJS	0.06325	0.10024	207.91652	4.466	2.126
FRAS	FRJS	0.07962	0.12619	207.91652	3.255	2.243

FRAS	FRJS	0.10024	0.15887	207.91652	3.271	2.844
FRAS	FRJS	0.12619	0.20000	207.91652	3.251	4.103
FRAS	FRJS	0.15887	0.25179	207.91652	3.259	3.604
FRAS	FRJS	0.20000	0.31698	207.91652	3.298	4.269
FRAS	FRJS	0.25179	0.39905	207.91652	3.187	3.112
FRAS	FRJS	0.31698	0.50238	207.91652	3.146	2.062
FRAS	FRJS	0.39905	0.63246	207.91652	3.185	1.691
FRAS	FRJS	0.50238	0.79621	207.91652	3.164	1.827
FRAS	FRJS	0.63246	1.00237	207.91652	3.484	1.752
FRAS	FRJS	0.79621	1.26191	207.91652	2.369	1.622
FRAS	FRJS	1.00237	1.58866	207.91652	4.155	1.627
FRAS	FRJS	1.26191	2.00000	207.91652	3.740	1.838
FRAS	FRJS	1.58866	2.51785	207.91652	3.783	1.788
FRAS	FRJS	2.00000	3.16979	207.91652	3.791	1.413
FRAS	FRJS	2.51785	3.99052	207.91652	3.908	1.585
FRAS	FRJS	3.16979	5.02377	207.91652	2.843	1.829
BIDS	QLBS	26.867	36.958	28.652	37.594	208.11305
sta1	sta2	lowpass	highpass	distance	km/sec	SNR
BIDS	QLBS	0.01589	0.02518	208.11305	2.756	3.723
BIDS	QLBS	0.02000	0.03170	208.11305	3.068	6.480
BIDS	QLBS	0.02518	0.03991	208.11305	3.817	2.599
BIDS	QLBS	0.03170	0.05024	208.11305	2.863	2.805
BIDS	QLBS	0.03991	0.06325	208.11305	2.925	4.558
BIDS	QLBS	0.05024	0.07962	208.11305	3.023	5.966
BIDS	QLBS	0.06325	0.10024	208.11305	3.030	6.278
BIDS	QLBS	0.07962	0.12619	208.11305	3.062	8.639
BIDS	QLBS	0.10024	0.15887	208.11305	3.034	8.771
BIDS	QLBS	0.12619	0.20000	208.11305	2.835	5.503
BIDS	QLBS	0.15887	0.25179	208.11305	2.788	4.027
BIDS	QLBS	0.20000	0.31698	208.11305	2.696	5.101
BIDS	QLBS	0.25179	0.39905	208.11305	2.563	5.876
BIDS	QLBS	0.31698	0.50238	208.11305	2.441	3.981
BIDS	QLBS	0.39905	0.63246	208.11305	2.427	2.470
BIDS	QLBS	0.50238	0.79621	208.11305	3.171	1.691
BIDS	QLBS	0.63246	1.00237	208.11305	3.308	2.192
BIDS	QLBS	0.79621	1.26191	208.11305	3.631	2.100
BIDS	QLBS	1.00237	1.58866	208.11305	4.405	2.058
BIDS	QLBS	1.26191	2.00000	208.11305	4.325	1.830
BIDS	QLBS	1.58866	2.51785	208.11305	2.600	1.311
BIDS	QLBS	2.00000	3.16979	208.11305	2.591	1.403
BIDS	QLBS	2.51785	3.99052	208.11305	-	-
BIDS	QLBS	3.16979	5.02377	208.11305	3.773	1.897
BLJS	LBNS	19.957	41.605	21.047	39.902	214.85291
sta1	sta2	lowpass	highpass	distance	km/sec	SNR
BLJS	LBNS	0.01589	0.02518	214.85291	3.518	0.627
BLJS	LBNS	0.02000	0.03170	214.85291	3.439	0.528
BLJS	LBNS	0.02518	0.03991	214.85291	3.538	1.427
BLJS	LBNS	0.03170	0.05024	214.85291	3.171	3.268
BLJS	LBNS	0.03991	0.06325	214.85291	3.226	5.399
BLJS	LBNS	0.05024	0.07962	214.85291	3.560	6.432
BLJS	LBNS	0.06325	0.10024	214.85291	3.145	10.618
BLJS	LBNS	0.07962	0.12619	214.85291	2.991	10.404
BLJS	LBNS	0.10024	0.15887	214.85291	2.963	5.259
BLJS	LBNS	0.12619	0.20000	214.85291	3.257	4.745
BLJS	LBNS	0.15887	0.25179	214.85291	3.291	5.407
BLJS	LBNS	0.20000	0.31698	214.85291	3.121	6.969
BLJS	LBNS	0.25179	0.39905	214.85291	3.101	6.197
BLJS	LBNS	0.31698	0.50238	214.85291	3.098	5.198
BLJS	LBNS	0.39905	0.63246	214.85291	3.062	3.734

BLJS	LBNS	0.50238	0.79621	214.85291	2.997	2.502
BLJS	LBNS	0.63246	1.00237	214.85291	3.783	1.875
BLJS	LBNS	0.79621	1.26191	214.85291	4.017	2.496
BLJS	LBNS	1.00237	1.58866	214.85291	3.751	2.203
BLJS	LBNS	1.26191	2.00000	214.85291	2.307	1.517
BLJS	LBNS	1.58866	2.51785	214.85291	2.305	1.369
BLJS	LBNS	2.00000	3.16979	214.85291	4.014	1.344
BLJS	LBNS	2.51785	3.99052	214.85291	4.008	1.510
BLJS	LBNS	3.16979	5.02377	214.85291	3.656	1.535
DJNS	NAMS	17.701	43.545	19.170	42.202	216.18854
sta1	sta2	lowpass	highpass	distance	km/sec	SNR
DJNS	NAMS	0.01589	0.02518	216.18854	-	-
DJNS	NAMS	0.02000	0.03170	216.18854	-	-
DJNS	NAMS	0.02518	0.03991	216.18854	-	-
DJNS	NAMS	0.03170	0.05024	216.18854	3.467	10.678
DJNS	NAMS	0.03991	0.06325	216.18854	3.144	34.375
DJNS	NAMS	0.05024	0.07962	216.18854	3.035	15.685
DJNS	NAMS	0.06325	0.10024	216.18854	3.090	4.798
DJNS	NAMS	0.07962	0.12619	216.18854	3.284	3.710
DJNS	NAMS	0.10024	0.15887	216.18854	3.276	5.090
DJNS	NAMS	0.12619	0.20000	216.18854	3.217	7.441
DJNS	NAMS	0.15887	0.25179	216.18854	3.223	6.428
DJNS	NAMS	0.20000	0.31698	216.18854	3.238	8.854
DJNS	NAMS	0.25179	0.39905	216.18854	3.196	10.492
DJNS	NAMS	0.31698	0.50238	216.18854	3.177	9.732
DJNS	NAMS	0.39905	0.63246	216.18854	3.142	6.759
DJNS	NAMS	0.50238	0.79621	216.18854	3.112	4.658
DJNS	NAMS	0.63246	1.00237	216.18854	3.074	2.857
DJNS	NAMS	0.79621	1.26191	216.18854	2.955	2.071
DJNS	NAMS	1.00237	1.58866	216.18854	3.654	1.960
DJNS	NAMS	1.26191	2.00000	216.18854	3.717	2.484
DJNS	NAMS	1.58866	2.51785	216.18854	3.704	1.597
DJNS	NAMS	2.00000	3.16979	216.18854	4.006	1.187
DJNS	NAMS	2.51785	3.99052	216.18854	4.222	1.438
DJNS	NAMS	3.16979	5.02377	216.18854	4.232	2.723
BIDS	LNYS	26.867	36.958	25.081	37.944	221.66298
sta1	sta2	lowpass	highpass	distance	km/sec	SNR
BIDS	LNYS	0.01589	0.02518	221.66298	2.152	1.794
BIDS	LNYS	0.02000	0.03170	221.66298	-	-
BIDS	LNYS	0.02518	0.03991	221.66298	-	-
BIDS	LNYS	0.03170	0.05024	221.66298	-	-
BIDS	LNYS	0.03991	0.06325	221.66298	2.921	4.334
BIDS	LNYS	0.05024	0.07962	221.66298	3.106	4.135
BIDS	LNYS	0.06325	0.10024	221.66298	3.008	4.807
BIDS	LNYS	0.07962	0.12619	221.66298	3.269	7.995
BIDS	LNYS	0.10024	0.15887	221.66298	3.264	5.550
BIDS	LNYS	0.12619	0.20000	221.66298	3.258	6.147
BIDS	LNYS	0.15887	0.25179	221.66298	3.213	5.181
BIDS	LNYS	0.20000	0.31698	221.66298	3.150	5.718
BIDS	LNYS	0.25179	0.39905	221.66298	3.094	7.088
BIDS	LNYS	0.31698	0.50238	221.66298	3.055	2.517
BIDS	LNYS	0.39905	0.63246	221.66298	3.527	2.216
BIDS	LNYS	0.50238	0.79621	221.66298	2.965	1.761
BIDS	LNYS	0.63246	1.00237	221.66298	4.227	1.206
BIDS	LNYS	0.79621	1.26191	221.66298	4.286	1.414
BIDS	LNYS	1.00237	1.58866	221.66298	3.830	1.661
BIDS	LNYS	1.26191	2.00000	221.66298	2.804	1.638
BIDS	LNYS	1.58866	2.51785	221.66298	4.561	1.596
BIDS	LNYS	2.00000	3.16979	221.66298	3.419	1.692

BIDS	LNYs	2.51785	3.99052	221.66298	3.421	3.296
BIDS	LNYs	3.16979	5.02377	221.66298	3.419	3.059
ENMS	JAZS	19.071	42.572	17.068	42.917	225.62440
sta1	sta2	lowpass	highpass	distance	km/sec	SNR
ENMS	JAZS	0.01589	0.02518	225.62440	-	-
ENMS	JAZS	0.02000	0.03170	225.62440	3.890	1.247
ENMS	JAZS	0.02518	0.03991	225.62440	3.441	4.329
ENMS	JAZS	0.03170	0.05024	225.62440	3.245	3.168
ENMS	JAZS	0.03991	0.06325	225.62440	3.127	3.793
ENMS	JAZS	0.05024	0.07962	225.62440	3.155	5.380
ENMS	JAZS	0.06325	0.10024	225.62440	3.245	5.374
ENMS	JAZS	0.07962	0.12619	225.62440	3.240	2.529
ENMS	JAZS	0.10024	0.15887	225.62440	3.328	2.739
ENMS	JAZS	0.12619	0.20000	225.62440	3.266	5.583
ENMS	JAZS	0.15887	0.25179	225.62440	3.151	4.734
ENMS	JAZS	0.20000	0.31698	225.62440	4.032	3.946
ENMS	JAZS	0.25179	0.39905	225.62440	3.232	5.045
ENMS	JAZS	0.31698	0.50238	225.62440	3.103	3.091
ENMS	JAZS	0.39905	0.63246	225.62440	3.059	2.514
ENMS	JAZS	0.50238	0.79621	225.62440	3.044	2.256
ENMS	JAZS	0.63246	1.00237	225.62440	2.999	1.454
ENMS	JAZS	0.79621	1.26191	225.62440	3.716	1.376
ENMS	JAZS	1.00237	1.58866	225.62440	3.475	1.649
ENMS	JAZS	1.26191	2.00000	225.62440	-	-
ENMS	JAZS	1.58866	2.51785	225.62440	3.586	1.559
ENMS	JAZS	2.00000	3.16979	225.62440	2.166	1.668
ENMS	JAZS	2.51785	3.99052	225.62440	3.882	1.746
ENMS	JAZS	3.16979	5.02377	225.62440	3.435	1.974
BDAS	WJHS	28.430	35.100	26.732	36.393	227.80893
sta1	sta2	lowpass	highpass	distance	km/sec	SNR
BDAS	WJHS	0.01589	0.02518	227.80893	3.922	1.351
BDAS	WJHS	0.02000	0.03170	227.80893	2.650	1.194
BDAS	WJHS	0.02518	0.03991	227.80893	2.674	3.489
BDAS	WJHS	0.03170	0.05024	227.80893	3.049	16.391
BDAS	WJHS	0.03991	0.06325	227.80893	3.089	13.459
BDAS	WJHS	0.05024	0.07962	227.80893	2.550	14.152
BDAS	WJHS	0.06325	0.10024	227.80893	2.571	18.859
BDAS	WJHS	0.07962	0.12619	227.80893	2.588	18.016
BDAS	WJHS	0.10024	0.15887	227.80893	2.521	9.055
BDAS	WJHS	0.12619	0.20000	227.80893	3.097	8.698
BDAS	WJHS	0.15887	0.25179	227.80893	4.718	6.320
BDAS	WJHS	0.20000	0.31698	227.80893	4.422	3.202
BDAS	WJHS	0.25179	0.39905	227.80893	3.013	1.695
BDAS	WJHS	0.31698	0.50238	227.80893	3.551	1.287
BDAS	WJHS	0.39905	0.63246	227.80893	3.458	0.999
BDAS	WJHS	0.50238	0.79621	227.80893	2.325	1.267
BDAS	WJHS	0.63246	1.00237	227.80893	2.649	1.461
BDAS	WJHS	0.79621	1.26191	227.80893	3.812	1.484
BDAS	WJHS	1.00237	1.58866	227.80893	2.135	1.522
BDAS	WJHS	1.26191	2.00000	227.80893	2.141	1.751
BDAS	WJHS	1.58866	2.51785	227.80893	2.570	1.578
BDAS	WJHS	2.00000	3.16979	227.80893	2.903	1.611
BDAS	WJHS	2.51785	3.99052	227.80893	-	-
BDAS	WJHS	3.16979	5.02377	227.80893	4.148	2.143
BLJS	SHBS	19.957	41.605	21.005	39.683	231.65176
sta1	sta2	lowpass	highpass	distance	km/sec	SNR
BLJS	SHBS	0.01589	0.02518	231.65176	-	-
BLJS	SHBS	0.02000	0.03170	231.65176	2.916	2.181

BLJS	SHBS	0.02518	0.03991	231.65176	-	-
BLJS	SHBS	0.03170	0.05024	231.65176	3.287	12.393
BLJS	SHBS	0.03991	0.06325	231.65176	3.338	4.354
BLJS	SHBS	0.05024	0.07962	231.65176	3.323	4.441
BLJS	SHBS	0.06325	0.10024	231.65176	3.127	7.349
BLJS	SHBS	0.07962	0.12619	231.65176	3.172	9.419
BLJS	SHBS	0.10024	0.15887	231.65176	3.217	8.108
BLJS	SHBS	0.12619	0.20000	231.65176	3.557	2.683
BLJS	SHBS	0.15887	0.25179	231.65176	3.624	2.989
BLJS	SHBS	0.20000	0.31698	231.65176	3.115	4.014
BLJS	SHBS	0.25179	0.39905	231.65176	3.110	4.658
BLJS	SHBS	0.31698	0.50238	231.65176	3.084	3.763
BLJS	SHBS	0.39905	0.63246	231.65176	3.043	3.006
BLJS	SHBS	0.50238	0.79621	231.65176	2.998	2.356
BLJS	SHBS	0.63246	1.00237	231.65176	3.291	1.977
BLJS	SHBS	0.79621	1.26191	231.65176	3.353	2.089
BLJS	SHBS	1.00237	1.58866	231.65176	2.747	1.994
BLJS	SHBS	1.26191	2.00000	231.65176	3.257	1.758
BLJS	SHBS	1.58866	2.51785	231.65176	3.161	1.409
BLJS	SHBS	2.00000	3.16979	231.65176	3.158	1.333
BLJS	SHBS	2.51785	3.99052	231.65176	3.975	1.471
BLJS	SHBS	3.16979	5.02377	231.65176	3.105	1.413
RSHS	WJHS	28.300	34.797	26.732	36.393	234.90611
sta1	sta2	lowpass	highpass	distance	km/sec	SNR
RSHS	WJHS	0.01589	0.02518	234.90611	-	-
RSHS	WJHS	0.02000	0.03170	234.90611	3.907	0.969
RSHS	WJHS	0.02518	0.03991	234.90611	3.677	2.956
RSHS	WJHS	0.03170	0.05024	234.90611	3.561	6.329
RSHS	WJHS	0.03991	0.06325	234.90611	3.130	20.214
RSHS	WJHS	0.05024	0.07962	234.90611	2.945	13.926
RSHS	WJHS	0.06325	0.10024	234.90611	2.821	9.592
RSHS	WJHS	0.07962	0.12619	234.90611	2.827	12.715
RSHS	WJHS	0.10024	0.15887	234.90611	2.889	10.704
RSHS	WJHS	0.12619	0.20000	234.90611	4.347	7.372
RSHS	WJHS	0.15887	0.25179	234.90611	4.747	4.449
RSHS	WJHS	0.20000	0.31698	234.90611	4.771	2.182
RSHS	WJHS	0.25179	0.39905	234.90611	2.190	1.174
RSHS	WJHS	0.31698	0.50238	234.90611	2.196	1.665
RSHS	WJHS	0.39905	0.63246	234.90611	2.211	1.442
RSHS	WJHS	0.50238	0.79621	234.90611	2.043	1.285
RSHS	WJHS	0.63246	1.00237	234.90611	2.977	1.158
RSHS	WJHS	0.79621	1.26191	234.90611	2.603	1.029
RSHS	WJHS	1.00237	1.58866	234.90611	3.894	1.205
RSHS	WJHS	1.26191	2.00000	234.90611	3.687	1.459
RSHS	WJHS	1.58866	2.51785	234.90611	3.689	1.503
RSHS	WJHS	2.00000	3.16979	234.90611	3.691	1.332
RSHS	WJHS	2.51785	3.99052	234.90611	3.696	1.583
RSHS	WJHS	3.16979	5.02377	234.90611	3.314	1.598
FRJS	YNBS	22.591	39.364	24.340	37.994	239.45290
sta1	sta2	lowpass	highpass	distance	km/sec	SNR
FRJS	YNBS	0.01589	0.02518	239.45290	-	-
FRJS	YNBS	0.02000	0.03170	239.45290	4.154	3.380
FRJS	YNBS	0.02518	0.03991	239.45290	-	-
FRJS	YNBS	0.03170	0.05024	239.45290	2.132	0.758
FRJS	YNBS	0.03991	0.06325	239.45290	2.881	1.304
FRJS	YNBS	0.05024	0.07962	239.45290	2.899	2.523
FRJS	YNBS	0.06325	0.10024	239.45290	2.896	5.560
FRJS	YNBS	0.07962	0.12619	239.45290	2.817	9.426
FRJS	YNBS	0.10024	0.15887	239.45290	2.923	6.839

FRJS	YNBS	0.12619	0.20000	239.45290	3.084	5.403
FRJS	YNBS	0.15887	0.25179	239.45290	3.050	3.736
FRJS	YNBS	0.20000	0.31698	239.45290	2.896	2.472
FRJS	YNBS	0.25179	0.39905	239.45290	2.884	2.646
FRJS	YNBS	0.31698	0.50238	239.45290	2.909	2.389
FRJS	YNBS	0.39905	0.63246	239.45290	2.903	1.661
FRJS	YNBS	0.50238	0.79621	239.45290	3.146	1.161
FRJS	YNBS	0.63246	1.00237	239.45290	3.737	1.398
FRJS	YNBS	0.79621	1.26191	239.45290	2.692	1.405
FRJS	YNBS	1.00237	1.58866	239.45290	2.689	1.518
FRJS	YNBS	1.26191	2.00000	239.45290	2.230	1.585
FRJS	YNBS	1.58866	2.51785	239.45290	3.045	1.418
FRJS	YNBS	2.00000	3.16979	239.45290	3.033	1.354
FRJS	YNBS	2.51785	3.99052	239.45290	3.031	1.550
FRJS	YNBS	3.16979	5.02377	239.45290	3.034	1.454
JLOS	WJHS	28.735	35.492	26.732	36.393	239.77992
sta1	sta2	lowpass	highpass	distance	km/sec	SNR
JLOS	WJHS	0.01589	0.02518	239.77992	-	-
JLOS	WJHS	0.02000	0.03170	239.77992	-	-
JLOS	WJHS	0.02518	0.03991	239.77992	-	-
JLOS	WJHS	0.03170	0.05024	239.77992	3.506	1.082
JLOS	WJHS	0.03991	0.06325	239.77992	3.356	2.928
JLOS	WJHS	0.05024	0.07962	239.77992	3.207	2.889
JLOS	WJHS	0.06325	0.10024	239.77992	3.199	4.535
JLOS	WJHS	0.07962	0.12619	239.77992	3.137	17.610
JLOS	WJHS	0.10024	0.15887	239.77992	3.140	8.965
JLOS	WJHS	0.12619	0.20000	239.77992	3.137	4.473
JLOS	WJHS	0.15887	0.25179	239.77992	2.127	2.759
JLOS	WJHS	0.20000	0.31698	239.77992	3.104	3.647
JLOS	WJHS	0.25179	0.39905	239.77992	3.038	3.032
JLOS	WJHS	0.31698	0.50238	239.77992	3.046	2.446
JLOS	WJHS	0.39905	0.63246	239.77992	3.002	2.511
JLOS	WJHS	0.50238	0.79621	239.77992	2.946	1.972
JLOS	WJHS	0.63246	1.00237	239.77992	3.566	1.367
JLOS	WJHS	0.79621	1.26191	239.77992	3.541	1.376
JLOS	WJHS	1.00237	1.58866	239.77992	3.447	1.526
JLOS	WJHS	1.26191	2.00000	239.77992	3.445	1.555
JLOS	WJHS	1.58866	2.51785	239.77992	4.313	1.481
JLOS	WJHS	2.00000	3.16979	239.77992	4.064	1.462
JLOS	WJHS	2.51785	3.99052	239.77992	4.070	1.591
JLOS	WJHS	3.16979	5.02377	239.77992	3.233	2.263
LNYS	WJHS	25.081	37.944	26.732	36.393	240.26912
sta1	sta2	lowpass	highpass	distance	km/sec	SNR
LNYS	WJHS	0.01589	0.02518	240.26912	-	-
LNYS	WJHS	0.02000	0.03170	240.26912	4.321	1.682
LNYS	WJHS	0.02518	0.03991	240.26912	-	-
LNYS	WJHS	0.03170	0.05024	240.26912	3.908	5.041
LNYS	WJHS	0.03991	0.06325	240.26912	3.055	3.911
LNYS	WJHS	0.05024	0.07962	240.26912	3.014	2.443
LNYS	WJHS	0.06325	0.10024	240.26912	3.173	4.209
LNYS	WJHS	0.07962	0.12619	240.26912	3.107	7.047
LNYS	WJHS	0.10024	0.15887	240.26912	-	-
LNYS	WJHS	0.12619	0.20000	240.26912	4.767	4.761
LNYS	WJHS	0.15887	0.25179	240.26912	3.226	3.868
LNYS	WJHS	0.20000	0.31698	240.26912	3.222	4.058
LNYS	WJHS	0.25179	0.39905	240.26912	3.109	3.039
LNYS	WJHS	0.31698	0.50238	240.26912	2.932	2.195
LNYS	WJHS	0.39905	0.63246	240.26912	2.947	1.987
LNYS	WJHS	0.50238	0.79621	240.26912	3.550	1.672

LNYS	WJHS	0.63246	1.00237	240.26912	3.561	1.394
LNYS	WJHS	0.79621	1.26191	240.26912	2.729	1.388
LNYS	WJHS	1.00237	1.58866	240.26912	3.785	1.283
LNYS	WJHS	1.26191	2.00000	240.26912	2.031	1.594
LNYS	WJHS	1.58866	2.51785	240.26912	4.479	1.591
LNYS	WJHS	2.00000	3.16979	240.26912	3.612	1.717
LNYS	WJHS	2.51785	3.99052	240.26912	3.678	3.097
LNYS	WJHS	3.16979	5.02377	240.26912	4.218	2.866
QLBS	WJHS	28.652	37.594	26.732	36.393	244.01152
sta1	sta2	lowpass	highpass	distance	km/sec	SNR
QLBS	WJHS	0.01589	0.02518	244.01152	-	-
QLBS	WJHS	0.02000	0.03170	244.01152	4.167	1.144
QLBS	WJHS	0.02518	0.03991	244.01152	3.005	1.388
QLBS	WJHS	0.03170	0.05024	244.01152	-	-
QLBS	WJHS	0.03991	0.06325	244.01152	2.912	4.213
QLBS	WJHS	0.05024	0.07962	244.01152	2.915	7.933
QLBS	WJHS	0.06325	0.10024	244.01152	2.943	3.414
QLBS	WJHS	0.07962	0.12619	244.01152	2.971	2.891
QLBS	WJHS	0.10024	0.15887	244.01152	2.894	6.831
QLBS	WJHS	0.12619	0.20000	244.01152	2.801	8.368
QLBS	WJHS	0.15887	0.25179	244.01152	2.815	5.329
QLBS	WJHS	0.20000	0.31698	244.01152	2.754	4.398
QLBS	WJHS	0.25179	0.39905	244.01152	2.576	3.262
QLBS	WJHS	0.31698	0.50238	244.01152	2.496	2.367
QLBS	WJHS	0.39905	0.63246	244.01152	3.898	1.558
QLBS	WJHS	0.50238	0.79621	244.01152	3.458	1.632
QLBS	WJHS	0.63246	1.00237	244.01152	3.498	2.003
QLBS	WJHS	0.79621	1.26191	244.01152	3.534	1.572
QLBS	WJHS	1.00237	1.58866	244.01152	2.082	1.352
QLBS	WJHS	1.26191	2.00000	244.01152	3.073	1.287
QLBS	WJHS	1.58866	2.51785	244.01152	4.150	1.349
QLBS	WJHS	2.00000	3.16979	244.01152	4.590	1.507
QLBS	WJHS	2.51785	3.99052	244.01152	2.993	1.579
QLBS	WJHS	3.16979	5.02377	244.01152	2.993	1.759
BDAS	QLBS	28.430	35.100	28.652	37.594	244.87831
sta1	sta2	lowpass	highpass	distance	km/sec	SNR
BDAS	QLBS	0.01589	0.02518	244.87831	-	-
BDAS	QLBS	0.02000	0.03170	244.87831	-	-
BDAS	QLBS	0.02518	0.03991	244.87831	-	-
BDAS	QLBS	0.03170	0.05024	244.87831	3.975	2.692
BDAS	QLBS	0.03991	0.06325	244.87831	2.842	1.797
BDAS	QLBS	0.05024	0.07962	244.87831	2.900	3.271
BDAS	QLBS	0.06325	0.10024	244.87831	2.917	2.577
BDAS	QLBS	0.07962	0.12619	244.87831	3.035	3.994
BDAS	QLBS	0.10024	0.15887	244.87831	2.931	7.203
BDAS	QLBS	0.12619	0.20000	244.87831	2.495	8.469
BDAS	QLBS	0.15887	0.25179	244.87831	2.680	6.477
BDAS	QLBS	0.20000	0.31698	244.87831	2.704	4.023
BDAS	QLBS	0.25179	0.39905	244.87831	2.611	3.807
BDAS	QLBS	0.31698	0.50238	244.87831	2.532	3.039
BDAS	QLBS	0.39905	0.63246	244.87831	2.374	2.312
BDAS	QLBS	0.50238	0.79621	244.87831	4.348	1.819
BDAS	QLBS	0.63246	1.00237	244.87831	3.812	1.402
BDAS	QLBS	0.79621	1.26191	244.87831	2.596	1.550
BDAS	QLBS	1.00237	1.58866	244.87831	4.631	2.100
BDAS	QLBS	1.26191	2.00000	244.87831	4.634	2.375
BDAS	QLBS	1.58866	2.51785	244.87831	3.498	1.726
BDAS	QLBS	2.00000	3.16979	244.87831	2.618	1.452
BDAS	QLBS	2.51785	3.99052	244.87831	4.749	1.644

BDAS	QLBS	3.16979	5.02377	244.87831	4.709	1.651
BLJS	FDAS	19.957	41.605	21.834	40.359	245.55402
sta1	sta2	lowpass	highpass	distance	km/sec	SNR
BLJS	FDAS	0.01589	0.02518	245.55402	3.898	2.693
BLJS	FDAS	0.02000	0.03170	245.55402	4.071	3.447
BLJS	FDAS	0.02518	0.03991	245.55402	-	-
BLJS	FDAS	0.03170	0.05024	245.55402	2.596	3.785
BLJS	FDAS	0.03991	0.06325	245.55402	2.683	2.636
BLJS	FDAS	0.05024	0.07962	245.55402	3.388	2.469
BLJS	FDAS	0.06325	0.10024	245.55402	3.418	2.985
BLJS	FDAS	0.07962	0.12619	245.55402	3.318	3.669
BLJS	FDAS	0.10024	0.15887	245.55402	3.219	3.604
BLJS	FDAS	0.12619	0.20000	245.55402	3.245	3.602
BLJS	FDAS	0.15887	0.25179	245.55402	3.216	4.429
BLJS	FDAS	0.20000	0.31698	245.55402	3.252	4.515
BLJS	FDAS	0.25179	0.39905	245.55402	3.252	3.681
BLJS	FDAS	0.31698	0.50238	245.55402	3.177	3.212
BLJS	FDAS	0.39905	0.63246	245.55402	3.184	2.757
BLJS	FDAS	0.50238	0.79621	245.55402	2.855	2.126
BLJS	FDAS	0.63246	1.00237	245.55402	3.118	1.878
BLJS	FDAS	0.79621	1.26191	245.55402	3.111	1.633
BLJS	FDAS	1.00237	1.58866	245.55402	3.349	1.509
BLJS	FDAS	1.26191	2.00000	245.55402	3.345	1.616
BLJS	FDAS	1.58866	2.51785	245.55402	4.299	1.665
BLJS	FDAS	2.00000	3.16979	245.55402	4.287	1.571
BLJS	FDAS	2.51785	3.99052	245.55402	3.250	1.822
BLJS	FDAS	3.16979	5.02377	245.55402	3.815	2.152
JAZS	NAMS	17.068	42.917	19.170	42.202	245.62926
sta1	sta2	lowpass	highpass	distance	km/sec	SNR
JAZS	NAMS	0.01589	0.02518	245.62926	3.744	2.079
JAZS	NAMS	0.02000	0.03170	245.62926	3.767	2.530
JAZS	NAMS	0.02518	0.03991	245.62926	3.305	2.565
JAZS	NAMS	0.03170	0.05024	245.62926	3.256	9.258
JAZS	NAMS	0.03991	0.06325	245.62926	3.127	16.271
JAZS	NAMS	0.05024	0.07962	245.62926	3.174	23.886
JAZS	NAMS	0.06325	0.10024	245.62926	3.222	11.680
JAZS	NAMS	0.07962	0.12619	245.62926	3.237	5.373
JAZS	NAMS	0.10024	0.15887	245.62926	3.425	2.712
JAZS	NAMS	0.12619	0.20000	245.62926	4.757	3.040
JAZS	NAMS	0.15887	0.25179	245.62926	3.222	4.109
JAZS	NAMS	0.20000	0.31698	245.62926	3.218	3.781
JAZS	NAMS	0.25179	0.39905	245.62926	3.265	3.866
JAZS	NAMS	0.31698	0.50238	245.62926	3.303	3.731
JAZS	NAMS	0.39905	0.63246	245.62926	3.554	2.944
JAZS	NAMS	0.50238	0.79621	245.62926	4.411	2.191
JAZS	NAMS	0.63246	1.00237	245.62926	-	-
JAZS	NAMS	0.79621	1.26191	245.62926	4.463	1.609
JAZS	NAMS	1.00237	1.58866	245.62926	3.385	1.513
JAZS	NAMS	1.26191	2.00000	245.62926	4.479	1.584
JAZS	NAMS	1.58866	2.51785	245.62926	4.472	1.632
JAZS	NAMS	2.00000	3.16979	245.62926	3.499	1.431
JAZS	NAMS	2.51785	3.99052	245.62926	3.491	1.608
JAZS	NAMS	3.16979	5.02377	245.62926	3.330	1.742
BLJS	DRBS	19.957	41.605	17.828	42.301	247.79448
sta1	sta2	lowpass	highpass	distance	km/sec	SNR
BLJS	DRBS	0.01589	0.02518	247.79448	-	-
BLJS	DRBS	0.02000	0.03170	247.79448	2.288	1.527
BLJS	DRBS	0.02518	0.03991	247.79448	2.258	1.222

BLJS	DRBS	0.03170	0.05024	247.79448	4.172	1.401
BLJS	DRBS	0.03991	0.06325	247.79448	3.130	2.461
BLJS	DRBS	0.05024	0.07962	247.79448	3.170	7.771
BLJS	DRBS	0.06325	0.10024	247.79448	3.372	15.087
BLJS	DRBS	0.07962	0.12619	247.79448	3.391	8.860
BLJS	DRBS	0.10024	0.15887	247.79448	3.465	3.138
BLJS	DRBS	0.12619	0.20000	247.79448	3.520	1.991
BLJS	DRBS	0.15887	0.25179	247.79448	3.484	2.280
BLJS	DRBS	0.20000	0.31698	247.79448	3.434	4.163
BLJS	DRBS	0.25179	0.39905	247.79448	3.267	3.361
BLJS	DRBS	0.31698	0.50238	247.79448	3.260	1.778
BLJS	DRBS	0.39905	0.63246	247.79448	2.355	1.430
BLJS	DRBS	0.50238	0.79621	247.79448	2.842	1.753
BLJS	DRBS	0.63246	1.00237	247.79448	2.893	2.221
BLJS	DRBS	0.79621	1.26191	247.79448	2.478	1.844
BLJS	DRBS	1.00237	1.58866	247.79448	2.472	1.580
BLJS	DRBS	1.26191	2.00000	247.79448	3.389	1.552
BLJS	DRBS	1.58866	2.51785	247.79448	3.389	1.570
BLJS	DRBS	2.00000	3.16979	247.79448	4.041	1.381
BLJS	DRBS	2.51785	3.99052	247.79448	3.625	1.428
BLJS	DRBS	3.16979	5.02377	247.79448	2.772	2.136
BDAS	BIDS	28.430	35.100	26.867	36.958	252.34773
sta1	sta2	lowpass	highpass	distance	km/sec	SNR
BDAS	BIDS	0.01589	0.02518	252.34773	3.657	6.492
BDAS	BIDS	0.02000	0.03170	252.34773	3.597	8.037
BDAS	BIDS	0.02518	0.03991	252.34773	3.689	26.139
BDAS	BIDS	0.03170	0.05024	252.34773	3.303	31.971
BDAS	BIDS	0.03991	0.06325	252.34773	3.143	22.284
BDAS	BIDS	0.05024	0.07962	252.34773	3.153	11.529
BDAS	BIDS	0.06325	0.10024	252.34773	3.094	10.311
BDAS	BIDS	0.07962	0.12619	252.34773	3.094	14.094
BDAS	BIDS	0.10024	0.15887	252.34773	3.196	8.847
BDAS	BIDS	0.12619	0.20000	252.34773	3.151	6.300
BDAS	BIDS	0.15887	0.25179	252.34773	3.291	6.939
BDAS	BIDS	0.20000	0.31698	252.34773	3.247	5.071
BDAS	BIDS	0.25179	0.39905	252.34773	3.094	3.962
BDAS	BIDS	0.31698	0.50238	252.34773	3.043	3.682
BDAS	BIDS	0.39905	0.63246	252.34773	3.033	2.461
BDAS	BIDS	0.50238	0.79621	252.34773	4.086	2.306
BDAS	BIDS	0.63246	1.00237	252.34773	3.655	1.609
BDAS	BIDS	0.79621	1.26191	252.34773	3.294	1.588
BDAS	BIDS	1.00237	1.58866	252.34773	3.548	1.750
BDAS	BIDS	1.26191	2.00000	252.34773	3.544	1.898
BDAS	BIDS	1.58866	2.51785	252.34773	2.499	1.750
BDAS	BIDS	2.00000	3.16979	252.34773	2.502	1.560
BDAS	BIDS	2.51785	3.99052	252.34773	3.431	1.638
BDAS	BIDS	3.16979	5.02377	252.34773	3.425	1.687
BIDS	JLOS	26.867	36.958	28.735	35.492	252.87619
sta1	sta2	lowpass	highpass	distance	km/sec	SNR
BIDS	JLOS	0.01589	0.02518	252.87619	-	-
BIDS	JLOS	0.02000	0.03170	252.87619	2.355	2.146
BIDS	JLOS	0.02518	0.03991	252.87619	3.650	2.563
BIDS	JLOS	0.03170	0.05024	252.87619	3.214	4.937
BIDS	JLOS	0.03991	0.06325	252.87619	2.909	4.953
BIDS	JLOS	0.05024	0.07962	252.87619	2.908	8.461
BIDS	JLOS	0.06325	0.10024	252.87619	2.770	7.565
BIDS	JLOS	0.07962	0.12619	252.87619	3.900	7.757
BIDS	JLOS	0.10024	0.15887	252.87619	3.458	5.884
BIDS	JLOS	0.12619	0.20000	252.87619	3.211	9.887

BIDS	JLOS	0.15887	0.25179	252.87619	3.008	8.182
BIDS	JLOS	0.20000	0.31698	252.87619	3.036	4.541
BIDS	JLOS	0.25179	0.39905	252.87619	2.958	3.286
BIDS	JLOS	0.31698	0.50238	252.87619	2.679	2.500
BIDS	JLOS	0.39905	0.63246	252.87619	3.754	2.741
BIDS	JLOS	0.50238	0.79621	252.87619	3.020	2.255
BIDS	JLOS	0.63246	1.00237	252.87619	4.053	1.785
BIDS	JLOS	0.79621	1.26191	252.87619	3.012	1.616
BIDS	JLOS	1.00237	1.58866	252.87619	3.003	1.558
BIDS	JLOS	1.26191	2.00000	252.87619	3.133	1.924
BIDS	JLOS	1.58866	2.51785	252.87619	4.424	1.854
BIDS	JLOS	2.00000	3.16979	252.87619	4.424	1.646
BIDS	JLOS	2.51785	3.99052	252.87619	3.939	2.209
BIDS	JLOS	3.16979	5.02377	252.87619	3.502	2.408
BLJS	SHMS	19.957	41.605	21.448	39.691	259.12320
sta1	sta2	lowpass	highpass	distance	km/sec	SNR
BLJS	SHMS	0.01589	0.02518	259.12320	-	-
BLJS	SHMS	0.02000	0.03170	259.12320	3.194	2.144
BLJS	SHMS	0.02518	0.03991	259.12320	3.137	8.125
BLJS	SHMS	0.03170	0.05024	259.12320	2.850	8.210
BLJS	SHMS	0.03991	0.06325	259.12320	3.160	3.107
BLJS	SHMS	0.05024	0.07962	259.12320	3.259	1.805
BLJS	SHMS	0.06325	0.10024	259.12320	3.174	3.401
BLJS	SHMS	0.07962	0.12619	259.12320	3.209	6.058
BLJS	SHMS	0.10024	0.15887	259.12320	3.228	9.573
BLJS	SHMS	0.12619	0.20000	259.12320	3.191	4.924
BLJS	SHMS	0.15887	0.25179	259.12320	3.194	3.956
BLJS	SHMS	0.20000	0.31698	259.12320	3.218	4.776
BLJS	SHMS	0.25179	0.39905	259.12320	3.142	4.720
BLJS	SHMS	0.31698	0.50238	259.12320	3.095	3.825
BLJS	SHMS	0.39905	0.63246	259.12320	3.097	2.597
BLJS	SHMS	0.50238	0.79621	259.12320	3.101	1.732
BLJS	SHMS	0.63246	1.00237	259.12320	2.642	1.414
BLJS	SHMS	0.79621	1.26191	259.12320	2.640	1.955
BLJS	SHMS	1.00237	1.58866	259.12320	3.613	2.088
BLJS	SHMS	1.26191	2.00000	259.12320	2.984	1.944
BLJS	SHMS	1.58866	2.51785	259.12320	2.521	1.584
BLJS	SHMS	2.00000	3.16979	259.12320	2.034	1.536
BLJS	SHMS	2.51785	3.99052	259.12320	3.891	1.921
BLJS	SHMS	3.16979	5.02377	259.12320	3.874	2.020
BIDS	KBRS	26.867	36.958	25.789	39.264	259.29306
sta1	sta2	lowpass	highpass	distance	km/sec	SNR
BIDS	KBRS	0.01589	0.02518	259.29306	-	-
BIDS	KBRS	0.02000	0.03170	259.29306	-	-
BIDS	KBRS	0.02518	0.03991	259.29306	-	-
BIDS	KBRS	0.03170	0.05024	259.29306	3.142	7.872
BIDS	KBRS	0.03991	0.06325	259.29306	3.123	9.011
BIDS	KBRS	0.05024	0.07962	259.29306	3.164	9.991
BIDS	KBRS	0.06325	0.10024	259.29306	3.065	16.968
BIDS	KBRS	0.07962	0.12619	259.29306	3.121	12.729
BIDS	KBRS	0.10024	0.15887	259.29306	3.231	4.029
BIDS	KBRS	0.12619	0.20000	259.29306	3.203	3.384
BIDS	KBRS	0.15887	0.25179	259.29306	2.937	2.599
BIDS	KBRS	0.20000	0.31698	259.29306	2.909	2.211
BIDS	KBRS	0.25179	0.39905	259.29306	2.968	2.534
BIDS	KBRS	0.31698	0.50238	259.29306	2.975	2.409
BIDS	KBRS	0.39905	0.63246	259.29306	2.978	2.510
BIDS	KBRS	0.50238	0.79621	259.29306	2.948	2.119
BIDS	KBRS	0.63246	1.00237	259.29306	3.502	1.960

BIDS	KBRS	0.79621	1.26191	259.29306	3.523	2.108
BIDS	KBRS	1.00237	1.58866	259.29306	2.908	1.778
BIDS	KBRS	1.26191	2.00000	259.29306	2.011	1.654
BIDS	KBRS	1.58866	2.51785	259.29306	2.740	1.439
BIDS	KBRS	2.00000	3.16979	259.29306	4.147	1.430
BIDS	KBRS	2.51785	3.99052	259.29306	3.619	1.648
BIDS	KBRS	3.16979	5.02377	259.29306	3.625	1.773
ENMS	FRSS	19.071	42.572	16.739	42.115	263.76678
sta1	sta2	lowpass	highpass	distance	km/sec	SNR
ENMS	FRSS	0.01589	0.02518	263.76678	-	-
ENMS	FRSS	0.02000	0.03170	263.76678	4.405	1.801
ENMS	FRSS	0.02518	0.03991	263.76678	3.054	1.862
ENMS	FRSS	0.03170	0.05024	263.76678	-	-
ENMS	FRSS	0.03991	0.06325	263.76678	3.061	1.285
ENMS	FRSS	0.05024	0.07962	263.76678	3.061	3.180
ENMS	FRSS	0.06325	0.10024	263.76678	3.032	4.699
ENMS	FRSS	0.07962	0.12619	263.76678	2.923	4.274
ENMS	FRSS	0.10024	0.15887	263.76678	3.172	3.547
ENMS	FRSS	0.12619	0.20000	263.76678	3.339	4.694
ENMS	FRSS	0.15887	0.25179	263.76678	3.212	3.794
ENMS	FRSS	0.20000	0.31698	263.76678	3.356	2.378
ENMS	FRSS	0.25179	0.39905	263.76678	2.001	2.072
ENMS	FRSS	0.31698	0.50238	263.76678	2.001	1.817
ENMS	FRSS	0.39905	0.63246	263.76678	2.105	1.486
ENMS	FRSS	0.50238	0.79621	263.76678	2.922	1.802
ENMS	FRSS	0.63246	1.00237	263.76678	2.494	1.466
ENMS	FRSS	0.79621	1.26191	263.76678	2.251	1.480
ENMS	FRSS	1.00237	1.58866	263.76678	2.257	1.433
ENMS	FRSS	1.26191	2.00000	263.76678	2.158	1.339
ENMS	FRSS	1.58866	2.51785	263.76678	2.781	1.562
ENMS	FRSS	2.00000	3.16979	263.76678	2.333	1.572
ENMS	FRSS	2.51785	3.99052	263.76678	2.445	1.467
ENMS	FRSS	3.16979	5.02377	263.76678	2.445	1.388
HAQS	QLBS	29.050	34.920	28.652	37.594	264.18167
sta1	sta2	lowpass	highpass	distance	km/sec	SNR
HAQS	QLBS	0.01589	0.02518	264.18167	-	-
HAQS	QLBS	0.02000	0.03170	264.18167	2.575	0.957
HAQS	QLBS	0.02518	0.03991	264.18167	4.294	3.333
HAQS	QLBS	0.03170	0.05024	264.18167	3.060	5.495
HAQS	QLBS	0.03991	0.06325	264.18167	3.042	2.368
HAQS	QLBS	0.05024	0.07962	264.18167	2.952	2.905
HAQS	QLBS	0.06325	0.10024	264.18167	2.966	5.802
HAQS	QLBS	0.07962	0.12619	264.18167	2.938	6.448
HAQS	QLBS	0.10024	0.15887	264.18167	2.873	9.574
HAQS	QLBS	0.12619	0.20000	264.18167	2.808	12.134
HAQS	QLBS	0.15887	0.25179	264.18167	2.839	8.098
HAQS	QLBS	0.20000	0.31698	264.18167	2.906	3.866
HAQS	QLBS	0.25179	0.39905	264.18167	2.552	2.752
HAQS	QLBS	0.31698	0.50238	264.18167	2.452	2.409
HAQS	QLBS	0.39905	0.63246	264.18167	2.185	2.531
HAQS	QLBS	0.50238	0.79621	264.18167	2.195	2.255
HAQS	QLBS	0.63246	1.00237	264.18167	2.763	1.602
HAQS	QLBS	0.79621	1.26191	264.18167	4.017	1.658
HAQS	QLBS	1.00237	1.58866	264.18167	3.326	1.841
HAQS	QLBS	1.26191	2.00000	264.18167	3.307	1.925
HAQS	QLBS	1.58866	2.51785	264.18167	3.297	1.603
HAQS	QLBS	2.00000	3.16979	264.18167	2.788	1.431
HAQS	QLBS	2.51785	3.99052	264.18167	3.706	1.651
HAQS	QLBS	3.16979	5.02377	264.18167	4.377	1.971

